2003

Active Vibration Suppression of Smart Structures Using Piezoelectric Shear Actuators

Brian P. Baillargeon

ACTIVE VIBRATION SUPPRESSION OF SMART STRUCTURES USING PIEZOELECTRIC SHEAR ACTUATORS

by

Brian P. Baillargeon

B.S. University of Maine, 2002

A THESIS

Submitted in Partial Fulfillment of the

Requirements for the Degree of

Master of Science

(in Mechanical Engineering)

The Graduate School

The University of Maine

December, 2003

Advisory Committee:

Senthil S. Vel, Assistant Professor of Mechanical Engineering, Advisor

Donald A. Grant, R.C. Hill Professor and Chairman of Mechanical Engineering

Vincent Caccese, Associate Professor of Mechanical Engineering

Michael T. Boyle, Associate Professor of Mechanical Engineering

ACTIVE VIBRATION SUPPRESSION OF SMART STRUCTURES USING PIEZOELECTRIC SHEAR ACTUATORS

By Brian P. Baillargeon

Thesis Advisor: Dr. Senthil S. Vel

An Abstract of the Thesis Presented
in Partial Fulfillment of the Requirements for the
Degree of Master of Science
(in Mechanical Engineering)
December, 2003

Active vibration damping using piezoelectric materials integrated with structural systems has found widespread use in engineering applications. Current vibration suppression systems usually consist of piezoelectric extension actuators bonded to the surface or embedded within the structure. The use of piezoelectric shear actuators/sensors has been proposed as an alternative, where the electric field is applied perpendicular to the direction of polarization to cause shear deformation of the material.

We present an exact analysis and active vibration suppression of laminated composite plates and cylindrical shells with embedded piezoelectric shear actuators and sensors. Suitable displacement and electric potential functions are utilized to identically satisfy the boundary conditions at the simply supported edges. A solution to the resulting set of coupled ordinary differential equations is obtained by using either a power series or

Frobenius series. The natural frequencies, mode shapes and through-thickness profiles of displacements, potential and stresses are presented for several lamination schemes. Active vibration suppression is implemented with positive position feedback (PPF) and velocity feedback. Frequency response curves with various controller frequencies, controller damping ratios and scalar gains demonstrate that an embedded shear actuator can be utilized to actively damp the fundamental mode of vibration. In addition, it is shown that suppression of the thickness modes is feasible using a piezoelectric shear actuator.

An experimental and finite element investigation of the active vibration suppression of a sandwich cantilever beam using piezoelectric shear actuators is also performed. The beam is constructed with aluminum facings, foam core and two piezoelectric shear actuators. The finite element analyses are performed using the commercial finite element package ABAQUS/Standard 6.3-1. It is shown experimentally for the first time that piezoelectric shear actuators can be utilized for active vibration suppression. There are significant reductions in beam tip acceleration amplitudes and settling time as a result of the positive position feedback and strain-rate feedback. The finite element shows good comparison with the experimental results.

DEDICATION

For my wife Stephanie…

ACKNOWLEDGEMENTS

There are a number of people who sincerely deserve my thanks for their effort in the support of my master's thesis. First, I would like to thank the work of my Advisory Committee throughout the process, including the reading of this thesis and making many important suggestions. Special thanks goes to Dr. Senthil S. Vel who gave me the perfect balance between technical direction and freedom in the pursuit my research interests. I would also like to thank Mary Girard for her help in completing some of the experimental work. I would like to thank Paul Melrose for providing me with the foam core material I needed for the cantilever beam experimental setup.

I gratefully acknowledge the support of Maine Space Grant Consortium under collaborative seed grant No. EP-02-11.

Finally, I would like to thank my family for all their love and support throughout my educational career. This is especially true for my wife Stephanie who occasionally even performed some of the experimental testing for me.

TABLE OF CONTENTS

LIST OF TABLES

LIST OF FIGURES

Chapter 1

INTRODUCTION

This chapter presents an introduction to active vibration suppression of structural systems using piezoelectric sensors and actuators. The motivation of the research is given in the first section, followed by a detailed literature review of piezoelectric shear actuators and active vibration damping through feedback control. The last section contains an overview of this thesis, including its research approach and contributions.

1.1. Motivation

Piezoelectricity (literally "pressure electricity"), in the simplest of terms, is a coupling between a material's mechanical and electrical fields. In the direct piezoelectric effect, an electric charge collects on the surface of a piezoelectric material when it is strained. In the converse piezoelectric effect, the material deforms mechanically when it is subjected to an electric field. The direct and converse effects enable a piezoelectric material to work as both a sensor for detecting strains and as an actuator to induce mechanical strains. The Curie brothers first discovered this phenomenon in 1880. The first serious application of the piezoelectric effect was the development of an ultrasonic submarine detector by Langevin and French co-workers after World War I. Since then, piezoelectric materials have been developed into many different technologies. This includes sonar, small tone audio devices, sensitive microphones, and many other devices.

The use of piezoelectric materials in smart/adaptive structures has been studied intensely for more than a decade. Engineering applications using this technology have

been proposed and conceived experimentally, such as for active vibration suppression (Fuller *et al.*, 1996; Bailey and Hubbard, 1985; Garcia *et al.*, 1992), noise cancellation (Clark and Fuller, 1992; Hsu *et al.*, 1998), and shape control (Agrawal and Treanor, 1999; Koconis *et al.*, 1994).

Adaptive structures using piezoelectric materials usually employ lead zirconium titanate (PZT) ceramic sensors and actuators to detect and mechanically deform a structure. Piezopolymer films (e.g. polyvinylidene fluoride (PVDF)) are not usually preferred because they lack the stiffness requirements to achieve high actuation authority. The addition of the PZT material allows the structure to sense and react to its environment. Conventional adaptive structures require a network of these actuators and sensors to be bonded to the surfaces or embedded within the structure (Crawley and de Luis, 1987). The actuators and sensors are coupled together to form a closed-loop network. This enables the sensors to detect a change in structural deformation, and then feed the actuators with a signal to produce the desired response to the external stimulus.

Most raw piezoceramic materials do not exhibit the piezoelectric effect because all the dipoles of the crystal structure are not oriented in the same direction. There are regions of the material that are groups of aligned dipoles called domains (Clephas, 1999). Raw artificially created piezoelectric materials have randomly oriented domains throughout the material. To align these domains, a very strong DC electric field is passed through the material at a slightly elevated temperature (~100°C for PZT-5A). This process is referred to as poling of a material. After it has been poled, the material will have a net polarization and exhibit the piezoelectric phenomenon provided that the

applied electric field is not large enough to cause the material to de-pole (degradation of the polarization).

Traditionally, an adaptive structure employs a thin rectangular piezoelectric wafer that is poled in the thickness direction, with electrodes applied to the faces that are perpendicular to the poling direction. These piezoceramic elements are referred to as *extension* actuators (see Figure 1.1(a)). Application of the electric field in the thickness direction causes the piezoelectric extension actuator's lateral dimensions to increase or decrease. An electric field E_3 applied in the thickness direction will cause a longitudinal strain $\varepsilon_1 = d_{13} E_3$, where d_{13} is the piezoelectric strain constant that relates the axial strain to the transverse electric field (Nye, 1957). In addition, the electric field will induce a transverse normal strain $\varepsilon_3 = d_{33} E_3$, where d_{33} is the piezoelectric strain constant that relates the transverse normal strain to the transverse electric field. Typically, extension actuators are bonded to the surface of a host structure to cause deformation. As an alternative to the conventional poling technique, one can pole the piezoelectric element in a different direction in order to utilize other modes of actuation. For example, Bent (1997) utilized the d_{33} piezoelectric coefficient to produce extension actuators by poling piezoelectric fibers in the axial direction and applying an electric field parallel to the fiber axis using interdigitated electrodes.

A distinctly different piezoelectric transduction mode is achieved when the electric field is perpendicular to the poling direction. In this case, a piezoelectric rectangular element that is poled in the longitudinal direction and subjected to an electric field E_3 in the thickness direction will undergo shear deformation of magnitude

$\gamma_{13} = d_{35} E_3$ as shown in Figure 1.1(b). This is referred to as the piezoelectric *shear* actuation mechanism.

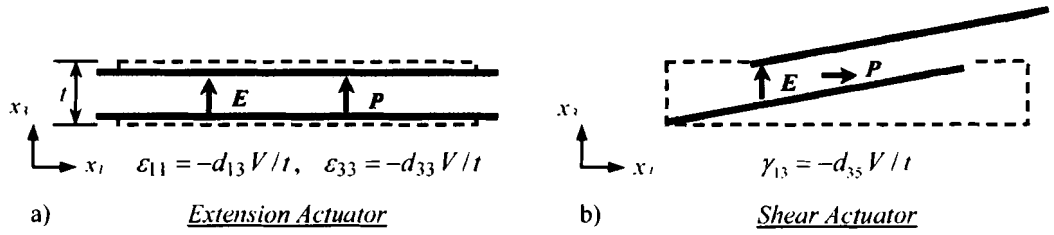

Figure 1.1. The piezoelectric extension vs. shear mechanisms

The reason for the overzealous use of the piezoelectric extensional mechanism may be due to initial experiments on the converse piezoelectric phenomena using a piezopolymer, polyvinylidene fluoride (PVDF), as stated by Benjeddou and Deü (2001a). In this instance, the material is well suited for use as an extension actuator because the extensional coefficient is greater than its shear counterpart. This way of thinking has transferred to other piezoelectric materials, mainly PZT, but that reasoning is no longer logical.

For most of the materials that exhibit piezoelectric behavior, the piezoelectric shear coefficients d_{35}, has the largest value of all the coefficients (Glazounov and Zhang, 1998). For example, typical values of the PZT-5A coefficients, d_{35}, d_{13} and d_{33} are 584×10^{-12} m/V, -171×10^{-12} m/V and 374×10^{-12} m/V, respectively (Berlincourt and Krueger, n.d.). As can be seen, the piezoelectric shear coefficient d_{35} is far superior to those of the extensional coefficients d_{13} and d_{33}. This data suggests that a shear-mode piezoelectric element might be better suited than an extensional actuator in terms of sensing and actuating.

In most smart structural applications, thickness-poled piezoelectric elements are usually placed at the extreme thickness positions of the structure to achieve the most effective actuation authority, as depicted in Figure 1.2(a). This subjects the actuator to high longitudinal stress that is unfavorable to the brittle piezoceramic. Also, if the actuator is placed on the surface of the structure, then the active element is likely to be damaged by contact with foreign objects. To alleviate these problems Zhang and Sun (1995) proposed the use of an axial-poled piezoelectric core sandwiched between two elastic face sheets as shown in Figure 1.2(b).

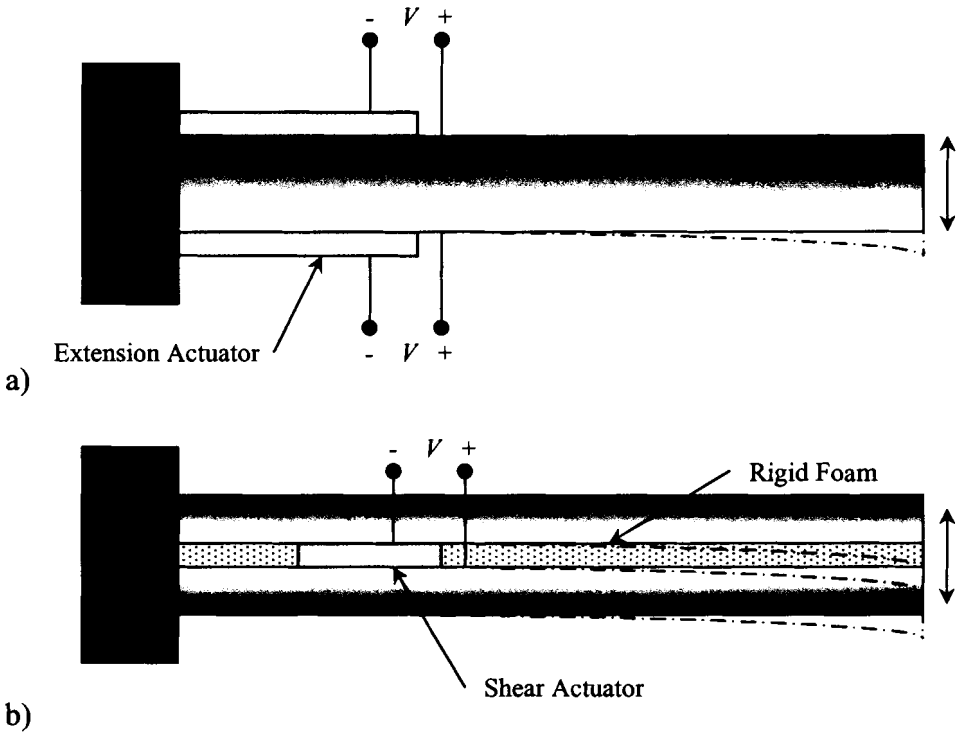

Figure 1.2. The transverse tip deflection of a cantilever beam using extension and shear actuators

More than a decade of intense research into the use of piezoelectric materials in smart structures has primarily focused on the use of thickness-poled active elements. Only a relatively limited number of studies have dealt with the use of piezoelectric shear

actuators. It should be noted that analytical and numerical solutions for thickness-poled piezoelectric materials are not applicable to axial-poled piezoelectric materials since the assumed form of the piezoelectric matrix that couples the electric field to the mechanical deformation is different. To the author's knowledge, there have been no published experimental investigations on the use of a piezoelectric shear actuator for smart structural applications to date. In this thesis, analytical, numerical and experimental research is performed to quantify the effectiveness of shear actuators for active vibration suppression of smart structures.

1.2. Literature Review

1.2.1. Piezoelectric Extension Actuators

In order to successfully incorporate piezoelectric materials into adaptive structures, the mechanical interaction between active element and the host structure must be fully understood. Numerous mechanical models have been developed for the analysis of hybrid beams and shells with thickness-poled piezoelectric elements (Crawley and Anderson, 1990; Lee, 1990; Huang and Wu, 1996; Mitchell and Reddy, 1995; Batra and Liang, 1997). Exact three-dimensional solutions for the static generalized plane strain deformation of simply supported piezoelectric plates have been given by Ray *et al.* (1993) and Heyliger and Brooks (1996). Heyliger (1994; 1997), Bisegna and Maceri (1996) and Lee and Jiang (1996) have obtained exact solutions for simply supported rectangular piezoelectric laminates. Analysis of the vibrations of a simply supported plate with piezoceramic actuators either bonded to its upper and lower surfaces or embedded within the laminate was done by Yang *et al.* (1994) and Batra *et al.* (1996).

Three-dimensional analytical solutions for thick piezoelectric plates subjected to arbitrary boundary conditions have been developed by Vel and Batra (2000a; 2000b; 2001a). Exact solutions for the free vibration of hybrid plates with thickness-poled piezoelectric layers have been obtained by Heyliger and Brooks (1995) and Heyliger and Saravanos (1995).

1.2.2. Piezoelectric Shear Actuators

Utilization of the piezoelectric shear coefficient d_{35} is not a new concept. In fact, it has been used in accelerometers since the 1960's (Bradley and Bergman, 1963). It also has been used in piezoelectric torsional elements as a means of generating angular displacement (Glazounov and Zhang, 1998). It has only been recently suggested, however, that the thickness-shear mode of piezoelectric actuation be used in smart structures (Sun and Zhang, 1995). Since then, there have been numerous finite element and analytical studies concerning the use of shear piezoelectric elements in smart structure applications. There has also been little experimental research into the actual shear actuation mechanism. The following section contains an overview of the current state of knowledge of the piezoelectric shear sensor/actuator mechanism.

Sun and Zhang (1995) were the first to study the effects of using a shear-mode type actuator in a cantilever beam configuration using a commercial finite element package. They concluded that a beam using an embedded thickness-shear mode type of actuator is much better at providing tip deflection, so long as there is a large actuator thickness ratio (thickness-to-length ratio). If the thickness ratio is small, then the surface mounted extensional actuators are superior to the embedded shear actuators. They also found other advantages of the shear actuator such as reduced stress levels in the actuator,

and lower stresses at the interface between the actuator and the host structure. It is advantageous to have smaller stresses since PZT is a brittle material with an ultimate tensile strength of 76 MPa.

Zhang and Sun (1995) derived governing equations for an adaptive sandwich beam using the variational principle. These equations allow for the analysis of stress distributions for a cantilever beam with either an extensional- or shear-mode piezoelectric actuators. It was found that the shear-mode configuration provides much lower stresses in the actuator because it is located closer to the neutral axis of the beam. This analytical solution, however, is valid only for a cantilever beam with a piezoelectric shear actuator extending over the entire length of the beam. As the authors point out, this is not practical in real engineering situations due to the high mass density of the piezoceramic.

Benjeddou *et al.* (1999) furthered the state of knowledge by deriving a shear actuated beam finite element with the facings modeled as Euler-Bernoulli beams and the core modeled as a shear deformable Timoshenko beam. These elements are capable of dealing with both extensional and shear piezoelectric material. It was found that the extensional actuators, located on the surface, produce moments and forces concentrated at the extremities of the actuator. The shear actuators, however, produce distributed moments throughout the length of the device. Thus, the piezoelectric shear mechanism alleviates de-bonding associated with high stresses at the extremities of actuator. It was also found that the shear-mode of actuation performs better on stiffer structures than its extensional counterpart. In agreement with Zhang and Sun (1995) and Sun and Zhang (1995), it was also found that thicker shear actuators perform best, whereas thin extensional actuators performed well.

Zhang and Sun (1999) derived an analytical solution for dealing with a plate with a piezoelectric core using the Raleigh-Ritz method based on the principal of stationary potential energy. In this model, the piezoelectric core is poled in the axial direction to induce the needed shear motion. This solution is compared to a finite element model of the same situation, and it is found that the analytical solution is in good agreement with the FE solution.

Trindade *et al.* (2000) performed a parametric study on the active control of a sandwich beam with both shear and extension actuators. The finite element analysis modeled the facings as Euler-Bernoulli layers and the core as a Timoshenko layer. The control law utilized was a linear quadratic regulator based on optimal control with state feedback. The results of the study indicate that using a shear actuator is better suited for the control of bending vibrations in a sandwich beam than an extension actuator.

Benjeddou *et al.* (2001a) developed an analytical solution of an adaptive sandwich composite with shear-actuated shells of revolution. Subsequently, they presented a finite element implementation of the analytical formulation (Benjeddou *et al.*, 2001b). The finite element solution was validated using an analytical solution to the vibration of a PZT-4 spherical shell. This analysis gives a viable method for the vibrational analysis of axisymmetric shells with embedded piezoelectric shear actuators.

Benjeddou and Deü (2001a; 2001b) derived an exact three-dimensional solution of transverse shear actuation and sensing of simply supported piezoelectric plates. In their derivation they use a three-dimensional mixed state-space formulation. In the second portion of the study, the solution is applied to an adaptive sandwich composite plate. Parametric studies are reported for different plate thickness ratio, piezoelectric

2. The actuator/sensor is best suited for placement on the mid-surface of the host specimen.
3. The actuator is suitable for small amplitude displacements.
4. The shear-mode produces distributed moments throughout the actuator, rather than point forces and moments at the element extremities, as with an extension actuator.
5. Shear-mode of movement performs better on stiffer structures, as compared to its extensional counterpart.

There are, however, disadvantages related to using the shear-mode of the piezoelectric device. A thicker shear actuator is needed to actively control the structure. This is a disadvantage because of the high mass density of the piezoceramic. Utilization of these actuators could increase the mass of the structure considerably.

A limitation of the current state of knowledge is that none of the analytical or numerical studies have been compared with experiments. The efficacy of piezoelectric shear-mode for actively controlling smart structures has not been experimentally verified. A goal of this thesis is to experimentally prove the viability of using shear-mode piezoelectric material in smart/adaptive structure applications.

1.2.3. Vibration Suppression Using Adaptive Structures

Vibration damping in structures can be achieved by a passive, active or hybrid active-passive control system. Passive damping systems can employ a constrained viscoelastic layer that dissipates energy by deformation of the material (Kerwin, Jr., 1959, Benjeddou, 2000). The advantages of passive damping systems are that they are inherently stable and have a low-cost relative to active damping systems. However, the

effectiveness of passive vibration control depends on the frequency, temperature and geometry. Another type of passive damping system utilizes shunted piezoelectric materials (Hagood and von Flotow, 1991). The mechanical energy is dissipated as heat in the resistor. This type of passive damping is dependent on frequency, but is less dependent on temperature than that of a viscoelastic material. Since active control systems usually employ smart materials, depending on the control algorithm, an extremely focused region on the frequency spectrum can be targeted for suppression. In addition, active damping systems possess the adaptability of altering control parameters in real-time that passive systems do not (Benjeddou, 2000). A disadvantage of many control algorithms is the phenomena of spillover, where the stability of the structure can be compromised by inadvertently exciting an uncontrolled mode of vibration (Goh and Caughey, 1985). Researchers have also combined passive and active systems by using a smart material as the constraining layer creating the so-called active constrained layer damping (Benjeddou, 2000; Trindade *et al.*, 2001a; 2001b).

Vibration suppression is a concept that is very well suited for an intelligent structure because of its ability to sense and respond to external stimulus. The active vibration suppression uses sensors and actuators to control the response of the system. This requires a control scheme as seen in Figure 1.3 (Culshaw, 1996).

The system shown in Figure 1.3 is a closed-loop feedback control system since the signal sent to the actuator is a direct result of the incoming sensor signal. The process of active vibration control happens as follows: a sensory signal from the excited structure is detected by the control system, the signal is processed by a control algorithm and an appropriate signal is sent to the actuator. An important part of the control scheme is the

control algorithm because this determines how the structure responds to external excitation sources.

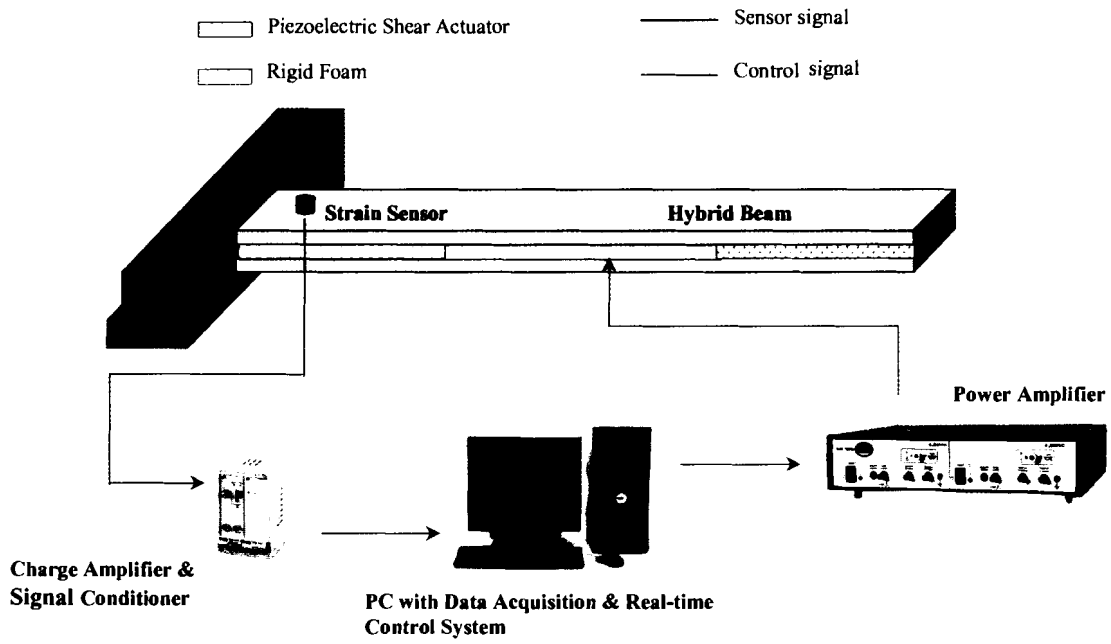

Figure 1.3. Feedback vibration suppression control scheme using piezoelectric elements

A control algorithm that actively dampens vibrations very well is a method called positive position feedback (PPF), which was first introduced by Goh and Caughey (1985). This control method has been successfully used in numerous experiments since that time (Ruggiero, 2002; Song *et al.*, 2001; Hegewald, 2000; DeGuilio, 2000, Meyer *et al.*, 1998). The PPF control uses second order differential equations to model the interaction between the system and compensator(s). The advantage of this system is that individual modes can be targeted for active vibration suppression.

The structure/compensator interaction is as follows (Friswell and Inman, 1999):

$$\text{The Structure:} \qquad \ddot{\xi} + 2\zeta\omega_n \dot{\xi} + \omega_n{}^2 \xi = g\omega_c{}^2 \eta \tag{1.1}$$

$$\text{The Compensator:} \qquad \ddot{\eta} + 2\zeta_c\omega_c \dot{\eta} + \omega_c{}^2 \eta = \omega_c{}^2 \xi \tag{1.2}$$

where ξ is the modal coordinate, η is the compensator coordinate, ζ is the damping ratio of the structure, ω_n is the natural frequency of the structure, ζ_c is the compensator damping ratio, ω_c is the compensator frequency and g is a scalar gain.

As can be seen from (1.1) and (1.2), there are really three quantities that must be appropriately chosen to implement this feedback control. These quantities are the scalar gain g, the compensator natural frequency ω_c and the compensator damping ratio ζ_c. The rest of the quantities are a direct result of the physical system. The scalar gain must lie within the range of $0<g<1$ for stability (Fanson and Caughey, 1990). Hegewald (2000) states that the compensator damping ratio is usually selected between the range of 0.05 to 0.5 and kept constant throughout the experiment. A suggestion of $1.45\omega_n$ for the value of the compensator frequency ω_c is given by Fagan (1993), while a value of $1.3\omega_n$ is suggested by Dosch *et al.* (1992).

The second feedback control law used in this thesis is strain-rate feedback (SRF) (Song *et al.*, 2001; Newman, 1992). In this thesis, this feedback control law will also be referred to as velocity feedback due to the fact that the structural velocity at a point will be applied to the compensator in Chapter 2. This feedback control algorithm is different than what is usually referred to as a simple negative or constant velocity feedback control algorithm that is usually seen in the literature (Lee *et al.*, 2001; Lim *et al.*, 1999; Lim *et al.*, 1997; Han and Lee, 1997; Lam *et al.*, 1997). In a simple negative or constant velocity feedback control law, the structural velocity is fed back directly to the actuator element. The proposed velocity feedback control law in this thesis models the structure and compensator in the following manner:

The Structure: $$\ddot{\xi} + 2\zeta\omega_n \dot{\xi} + \omega_n{}^2 \xi = -G\omega_c{}^2 \eta \quad (1.3)$$

The Compensator: $$\ddot{\eta} + 2\zeta_c\omega_c \dot{\eta} + \omega_c{}^2 \eta = \omega_c{}^2 \dot{\xi} \quad (1.4)$$

where ξ is the modal coordinate, η is the compensator coordinate, ζ is the damping ratio of the structure, ω_n is the natural frequency of the structure, ζ_c is the compensator damping ratio, ω_c is the compensator frequency and G is a scalar gain.

1.3. Overview of Thesis

1.3.1. Contributions

The contributions of this thesis include the development of analytical exact solutions for the vibration and active damping of composite plates and cylindrical shells with embedded piezoelectric shear actuators, and the experimental verification of the vibration suppression of a cantilever beam using shear actuators. The specific contributions of this thesis are as follows:

1. Several beam theories have been developed for the analysis of composite beams with embedded shear actuators (Zhang and Sun, 1996; Benjeddou *et al.* 1999; Raja *et al.*, 2002). However, since the beam theories are based on kinematic assumptions, they need to be validated using accurate three-dimensional analyses. In this thesis, we have developed three-dimensional benchmark solutions for the free vibration of simply supported laminated composite plates with embedded piezoelectric shear actuators. Natural frequencies, mode shapes, displacements, electric potential and stresses are presented for three-layer hybrid laminates consisting of a piezoelectric shear actuator sandwiched between fiber-reinforced composite layers. Results are also obtained

using the finite element method. It is found that the analytical and finite element results are in excellent agreement.

2. Analysis of the static deformation and free vibration of composite shells with radially-poled piezoelectric actuators have been presented by Chen *et al.* (1996), Dumir *et al.* (1997) and Chen and Shen (1998). In this thesis, three-dimensional exact solutions have been obtained for the first time for the static deformation, free vibration and forced vibration of composite cylindrical shells with embedded circumferentially-poled shear actuators.
3. Several researchers have presented exact solutions for the static deformation, free and forced vibration of piezoelectric plates and shells (Heyliger, 1994; Heyliger, 1997; Bisegna and Maceri, 1996; Chen and Shen, 1998; Vel and Batra, 2001b). However, none of these exact solutions included the effect of feedback control for structural damping. In this thesis, we have derived exact solutions for the active damping of composite plates and cylindrical shells with piezoelectric actuators, and the effect of controller parameters on system damping is studied. In addition, due to the fact that an exact solution is used in the analysis, this thesis also demonstrates that it is feasible to suppress thickness mode vibrations. It should be noted that traditional plate- or shell-type theories cannot be used to analyze thickness modes of vibration due to the kinematic assumption of inextensibility in the thickness direction.
4. In this thesis, a sandwich cantilever beam consisting of aluminum facings with a foam core and embedded shear actuators was fabricated and experimentally tested. The effectiveness of the shear actuators for active damping of vibration was experimentally verified. In addition, a feedback control algorithm was implemented

using a commercial finite element program. The finite element model of the system compared well with the experimental response.

1.3.2. Approach

The investigation of an exact solution to the vibration and active damping of composite plates with piezoelectric shear actuators is based upon the assumptions that the composite plate is simply supported and it is of infinite extent in one direction. This causes the plate to be in a state of generalized plane strain. Suitable displacement and electric potential functions that identically satisfy the boundary conditions at the simply supported edges are used to reduce the equations governing the steady-state vibrations of the hybrid laminate to a set of coupled ordinary differential equations, which are solved by employing the power series method. The solution satisfies the governing equations of motion, the charge equation of electrostatics, the interface conditions between laminae and the boundary conditions at the top and bottom surfaces. Using the derived solution, natural frequencies, mode shapes, displacements, stresses and potential are found for composite plates with embedded shear actuators. In addition, results from a steady-state forced vibration solution with integrated PPF and velocity feedback controllers are presented.

The next investigation involves the static deformation, vibration and active damping of cylindrical composite shells with embedded circumferentially-poled piezoelectric actuators. For this configuration, the assumed form of the electric potential and displacements yields a coupled set of ordinary differential equations of the radial coordinate with non-constant coefficients. A Frobenius series solution is used to solve the system of ordinary differential equations. The static deflection, natural frequencies,

mode shapes, displacements and stresses for a four layer composite shell that includes a shear sensor and actuator are presented. It is shown that active damping of a shell is feasible using circumferentially-poled piezoelectric actuators.

The last study of this thesis involves the experimental and numerical investigation of the active damping of a cantilever beam with embedded piezoelectric actuators. The cantilever beam consists of aluminum facings and a foam core. Two piezoelectric shear actuators are embedded within the foam core for feedback control of the structure. The experimental model is analyzed numerically using a commercial finite element program. The PPF feedback control is implemented in the numerical model by including a second order system to model the compensator. The experimental and numerical models are then compared to show that the observed experimental behavior of the piezoelectric shear actuator can be reproduced numerically.

1.3.3. Outline

The exact analysis of the vibration and active damping of composite plates with embedded piezoelectric shear actuators is presented in Chapter 2. Chapter 3 is an analysis of static deformation, vibration and active damping of cylindrical composite shells with piezoelectric shear actuators. An experimental and numerical investigation of a cantilever beam with embedded piezoelectric shear actuators is in Chapter 4. Chapter 5 presents the conclusions and recommendations for future research.

Chapter 2

EXACT ANALYSIS AND VIBRATION SUPPRESSION OF LAMINATED COMPOSITE PLATES USING EMBEDDED PIEZOELECTRIC SHEAR ACTUATORS

2.1. Introduction

This chapter provides an exact analysis and vibration suppression of laminated composite plates with embedded piezoelectric shear actuators. First, the solution provides system identification, which includes the natural frequencies, mode shapes and through-the-thickness plots of displacements, potential and stresses. Next, a forced vibration analysis is undertaken for the purpose of utilizing a vibration suppression algorithm. The two control laws used are positive position feedback (PPF) and velocity feedback. A thorough investigation into the influence of parameters for both control schemes is performed.

2.2. Problem Formulation

A rectangular Cartesian coordinate system is used, which can be found in Figure 2.1, to describe the infinitesimal deformations of the N-layer piezoelectric/composite plate. The plate is of extent L in the x_1-direction, H in the x_3-direction and infinity in the x_2-direction. The bottom and top surfaces, as well as the interfaces between lamina, are

given by $H^{(1)} = -H/2$, $H^{(2)},\ldots,H^{(n)},\ldots,H^{(N)}$, $H^{(N+1)} = H/2$. Also, each lamina is assumed to be homogenous.

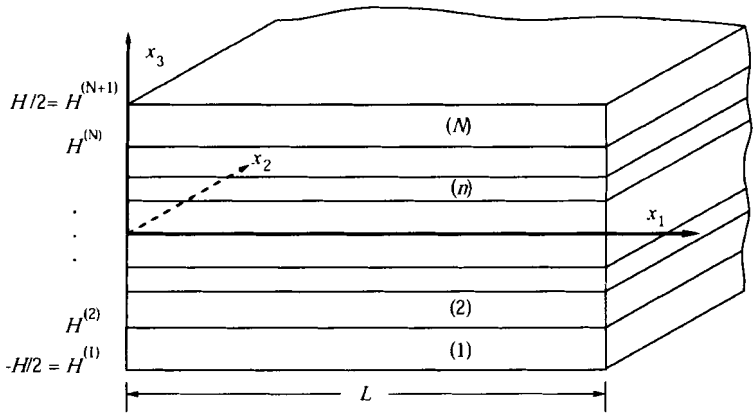

Figure 2.1. The geometrical configuration of an N-layer hybrid laminated plate

We first begin with the equations of motion and the charge equation of electrostatics in the absence of body forces and free charges:

$$\sigma_{ij,j}^{(n)} = \rho^{(n)} \ddot{u}_i^{(n)}, \qquad D_{i,i}^{(n)} = 0 \qquad (i,j = 1,2,3). \tag{2.1}$$

Where σ_{ij} are components of the Cauchy stress tensor, u_i are the displacements, D_i are the electric displacements and ρ is the density. A comma followed by an index j indicates partial differentiation with respect to the position x_j and a superimposed dot indicates partial derivative with respect to time t. A repeated index represents a summation over the range of the index. The superscript (n) refers to quantities of the n^{th}-layer of the piezoelectric/composite plate.

The edges of the plate are assumed to be simply supported and free of electric charge resulting in the following boundary conditions at $x_1 = 0, L$:

$$\sigma_{11}^{(n)} = \sigma_{12}^{(n)} = 0, \qquad u_3^{(n)} = 0, \qquad D_1^{(n)} = 0. \tag{2.2}$$

It should be noted that these boundary conditions are identical to those used by Vel and Batra (2001b). The mechanical boundary conditions are those for a simply supported plate. This is seen from the vanishing transverse displacement and moment at $x_1 = 0, L$. The assumption that the electric charge, and hence the electric displacement, D_1 vanish at the edges, allows an exact solution to be found. This boundary condition is different from that used by Heyliger and Brooks (1995) and Heyliger and Saravanos (1995) to obtain an exact solution for composite plates with embedded extension actuators. They assumed that the edges were electrically grounded and set the electric potential to zero at the edges. It should be noted that setting the charge equal to zero is a more realistic boundary condition because this is the condition most likely seen in practice.

The mechanical interface conditions between laminae are specified as follows:

$$u_i^{(n)} = u_i^{(n+1)}, \sigma_{3i}^{(n)} = \sigma_{3i}^{(n+1)} \text{ at } x_3 = H^{(n+1)} \text{ for } n = 1,\ldots,N\text{-}1. \tag{2.3}$$

The displacements are continuous between laminae since the layers are assumed to be perfectly bonded together. The stresses σ_{33}, σ_{13} and σ_{23} are continuous since the equilibrium of an infinitesimally small element that extends into both materials at the interface between adjoining laminae dictates that that the traction vector be continuous.

The interfaces between layers can be either electroded or not electroded. If the interface is not electroded, then the following conditions are used:

$$\phi^{(n)} = \phi^{(n+1)} \quad \text{and} \quad D_3^{(n)} = D_3^{(n+1)} \quad \text{at } x_3 = H^{(n+1)}. \tag{2.4}$$

If the interface is electroded, then the electrical interface condition becomes:

$$\phi^{(n)} = \phi^{(n+1)} = f(x_1, t) \text{ at } x_3 = H^{(n+1)}. \tag{2.5}$$

Here, ϕ denotes the electric potential. If the interface is not electroded, then the potential and the normal component of the electric displacement are continuous at the interface between laminae. If the interface is electroded, then the potential is prescribed by some known function $f(x_1,t)$. Again, the potential in this case must be continuous across the interface, although the normal component of the electric displacement need not be continuous.

The boundary conditions for the top and bottom surfaces of the plate are given as follows:

$$\sigma_{33} = q(x_1,t), \qquad \sigma_{13} = \sigma_{23} = 0 \qquad \text{at } x_3 = -H/2, H/2. \tag{2.6}$$

and

$$\phi = g(x_1,t) \quad \text{or} \quad D_3 = s(x_1,t) \qquad \text{at } x_3 = -H/2, H/2. \tag{2.7}$$

The shear stresses σ_{13} and σ_{23} are set equal to zero at $x_3 = H/2, -H/2$ because it is assumed that there are no applied shear stresses on either the top or bottom faces of the plate. The transverse normal stress is not set equal to zero because in the later part this chapter a sinusoidal load is applied to the top surface of the plate to find the steady-state response of the plate at a particular forcing frequency. The applied $q(x_1,t)$ is set equal to zero when the natural frequencies and mode shapes are found. The boundary condition (2.7) implies that the plate could have either a prescribed potential or charge on the top and bottom surfaces of the laminate.

The material model for each layer is considered linear elastic and orthotropic. Also, it is assumed that the poling direction of the piezoelectric material is in the x_1-x_2 plane. The constitutive relations for each of the n-layers are as follows in contracted form:

$$\begin{Bmatrix}\sigma_{11}\\ \sigma_{22}\\ \sigma_{33}\\ \sigma_{23}\\ \sigma_{31}\\ \sigma_{12}\end{Bmatrix}^{(n)} = \begin{bmatrix} C_{11} & C_{12} & C_{13} & 0 & 0 & C_{16} \\ C_{12} & C_{22} & C_{23} & 0 & 0 & C_{26} \\ C_{13} & C_{23} & C_{33} & 0 & 0 & C_{36} \\ 0 & 0 & 0 & C_{44} & C_{45} & 0 \\ 0 & 0 & 0 & C_{45} & C_{55} & 0 \\ C_{16} & C_{26} & C_{36} & 0 & 0 & C_{66} \end{bmatrix}^{(n)} \begin{Bmatrix}\varepsilon_{11}\\ \varepsilon_{22}\\ \varepsilon_{33}\\ 2\varepsilon_{23}\\ 2\varepsilon_{31}\\ 2\varepsilon_{12}\end{Bmatrix}^{(n)} - \begin{bmatrix} e_{11} & e_{21} & 0 \\ e_{12} & e_{22} & 0 \\ e_{13} & e_{23} & 0 \\ 0 & 0 & e_{34} \\ 0 & 0 & e_{35} \\ e_{16} & e_{26} & 0 \end{bmatrix}^{(n)} \begin{Bmatrix}E_1\\ E_2\\ E_3\end{Bmatrix}^{(n)},$$

$$\begin{Bmatrix}D_1\\ D_2\\ D_3\end{Bmatrix}^{(n)} = \begin{bmatrix} e_{11} & e_{12} & e_{13} & 0 & 0 & e_{16} \\ e_{21} & e_{22} & e_{23} & 0 & 0 & e_{26} \\ 0 & 0 & 0 & e_{34} & e_{35} & 0 \end{bmatrix}^{(n)} \begin{Bmatrix}\varepsilon_{11}\\ \varepsilon_{22}\\ \varepsilon_{33}\\ 2\varepsilon_{23}\\ 2\varepsilon_{31}\\ 2\varepsilon_{12}\end{Bmatrix}^{(n)} + \begin{bmatrix} \in_{11} & \in_{12} & 0 \\ \in_{12} & \in_{22} & 0 \\ 0 & 0 & \in_{33} \end{bmatrix}^{(n)} \begin{Bmatrix}E_1\\ E_2\\ E_3\end{Bmatrix}^{(n)}, \tag{2.8}$$

where ε_{ij} are components of the infinitesimal strain tensor, E_i are the electric field components, C_{ij} are the elastic constants in contracted notation, e_{ij} are the piezoelectric stress coefficients and $\in_{ij}$ are the electrical permittivity. The infinitesimal strain tensor and the electric field components are related to the displacements and electric potential in the following manner:

$$\varepsilon_{ij}^{(n)} = \frac{1}{2}\left(u_{i,j}^{(n)} + u_{j,i}^{(n)}\right), \; E_i^{(n)} = -\phi_{,i}^{(n)}. \tag{2.9}$$

2.3. Exact Solution

The goal of this study is to derive a general exact solution to the cylindrical bending vibration of a layered piezoelectric plate. We first begin by constructing a local coordinate system for each layer, originating at the center of the layer as shown in Figure 2.1. In this local coordinate system, the n^{th}-layer occupies the region of 0 to L in the x_1-direction, infinity in the x_2-direction and $h^{(n)}$ in the x_3-direction, where $h^{(n)} = H^{(n+1)} - H^{(n)}$.

The displacements, stresses, electric potential and electric displacements are assumed to be functions of only x_1 and x_3. This is a valid assumption because the

material properties and loads (mechanical and electrical) do not depend on x_2, and the plate is assumed to be infinite in the x_2-direction.

We seek a semi-inverse solution by assuming the following forms of the displacements and electric potential:

$$\begin{aligned} u_1(x_1,x_3,t) &= U_1(x_3)e^{i\omega t}\cos(px_1), \\ u_2(x_1,x_3,t) &= U_2(x_3)e^{i\omega t}\cos(px_1), \\ u_3(x_1,x_3,t) &= U_3(x_3)e^{i\omega t}\sin(px_1), \\ \phi(x_1,x_3,t) &= \Phi(x_3)e^{i\omega t}\cos(px_1), \end{aligned} \tag{2.10}$$

where $p = \dfrac{k\pi}{L}$ and k is an integer that defines the axial mode shape.

As can be seen from (2.10), the assumed transverse displacement u_3 is zero at $x_1 = 0, L$, which satisfies the displacement boundary conditions in (2.2). Substitution of (2.10) into (2.9) yields the following expressions for the infinitesimal strain tensor and electric field components:

$$\varepsilon_{11} = u_{1,1} = -U_1 p e^{i\omega t}\sin(p x_1), \quad \varepsilon_{22} = u_{2,2} = 0, \quad \varepsilon_{33} = u_{3,3} = U_3' e^{i\omega t}\sin(p x_1),$$

$$2\varepsilon_{23} = u_{2,3} + u_{3,2} = U_2' e^{i\omega t}\cos(p x_1), \quad 2\varepsilon_{12} = u_{1,2} + u_{2,1} = -U_2 p e^{i\omega t}\sin(p x_1), \tag{2.11}$$

$$2\varepsilon_{31} = u_{1,3} + u_{3,1} = (U_1' + U_3 p)e^{i\omega t}\cos(p x_1).$$

and

$$E_1 = -\phi_{,1} = \Phi p e^{i\omega t}\sin(p x_1), \quad E_2 = -\phi_{,2} = 0, \quad E_3 = -\phi_{,3} = -\Phi' e^{i\omega t}\cos(p x_1). \tag{2.12}$$

The prime denotes derivatives with respect to x_3.

The stresses and electric displacements are inferred in terms of the displacements using the constitutive relations in (2.8) along with (2.11) and (2.12). This results in the following Cauchy stress and electric displacement components:

$$\sigma_{11} = (-C_{11} U_1 p + C_{13} U_3' - C_{16} U_2 p - e_{11} \Phi p) e^{i\omega t} \sin(p x_1),$$

$$\sigma_{22} = (-C_{12} U_1 p + C_{23} U_3' - C_{26} U_2 p - e_{12} \Phi p) e^{i\omega t} \sin(p x_1),$$

$$\sigma_{33} = (-C_{13} U_1 p + C_{33} U_3' - C_{36} U_2 p - e_{13} \Phi p) e^{i\omega t} \sin(p x_1), \tag{2.13}$$

$$\sigma_{23} = (C_{44} U_2' p + C_{45} U_1' + C_{45} U_3 p + e_{34} \Phi') e^{i\omega t} \cos(p x_1),$$

$$\sigma_{31} = (C_{45} U_2' p + C_{55} U_1' + C_{55} U_3 p + e_{35} \Phi') e^{i\omega t} \cos(p x_1),$$

$$\sigma_{12} = (-C_{16} U_1 p + C_{36} U_3' - C_{66} U_2 p - e_{16} \Phi p) e^{i\omega t} \sin(p x_1).$$

and

$$D_1 = (-e_{11} U_1 p + e_{13} U_3' - e_{16} U_2 p + \in_{11} \Phi p) e^{i\omega t} \sin(p x_1),$$

$$D_2 = (-e_{21} U_1 p + e_{23} U_3' - e_{26} U_2 p + \in_{12} \Phi p) e^{i\omega t} \sin(p x_1), \tag{2.14}$$

$$D_3 = (e_{34} U_2' + e_{35} U_1' + e_{35} U_3 p - \in_{33} \Phi') e^{i\omega t} \cos(p x_1).$$

As can be seen from the expressions for σ_{11} and σ_{12} in (2.13) and D_1 in (2.14), the relevant boundary conditions of (2.2) are identically satisfied. Therefore, all the boundary conditions at the simply supported edges are identically satisfied by the assumed form of the displacements and electric potential in Equation (2.10).

The stress components and electric displacements from (2.13) and (2.14), respectively, are substituted into the equations of motion and charge equation of (2.1) yielding the following equations:

$$\sigma_{1j,j} = \rho \ddot{u}_1 : \quad \begin{aligned} &-C_{11} U_1 p^2 + (C_{13} + C_{55}) U_3' p - C_{16} U_2 p^2 - e_{11} \Phi p^2 + C_{45} U_2'' \\ &+ C_{55} U_1'' + e_{35} \Phi'' = -\rho \omega^2 U_1, \end{aligned} \tag{2.15}$$

$$\sigma_{2j,j} = \rho \ddot{u}_2 : \quad \begin{aligned} &-C_{16} U_1 p^2 + (C_{36} + C_{45}) U_3' p - C_{66} U_2 p^2 - e_{16} \Phi p^2 \\ &+ C_{44} U_2'' + C_{45} U_1'' + e_{34} \Phi'' = -\rho \omega^2 U_2, \end{aligned} \tag{2.16}$$

$$\sigma_{3j,j} = \rho \ddot{u}_3 : \quad \begin{aligned} &-(C_{13}+C_{55})U_1' p-(C_{36}+C_{45})U_2' p - C_{55}U_3 p^2 \\ &-(e_{13}+e_{35})\Phi' p + C_{33}U_3'' = -\rho\omega^2 U_3 \,, \end{aligned} \tag{2.17}$$

$$D_{i,i} = 0 : \quad \begin{aligned} &-e_{11}U_1 p^2 + (e_{13}+e_{35})U_3' p - e_{16}U_2 p^2 + \in_{11} \Phi p^2 \\ &+ e_{34}U_2'' + e_{35}U_1'' - \in_{33} \Phi'' = 0 \,. \end{aligned} \tag{2.18}$$

Note that the non-zero common factor $e^{i\omega t}$ cancels out in equations (2.15)-(2.18). Furthermore, since the governing equations have to hold at every location x_1, the common factors of either $\cos(p\,x_1)$ or $\sin(p\,x_1)$ in equations (2.15)-(2.18) are cancelled. Equations (2.15)-(2.18) form a set of four coupled second order ordinary differential equations that need to be solved. One method for solving this system of differential equations is by a power series solution for $U_i(x_3)$ and $\Phi(x_3)$ in the following manner:

$$U_i(x_3) = \sum_{\beta=0}^{\infty} \tilde{U}_i^{(\beta)} x_3^{\beta} \,, \; \Phi(x_3) = \sum_{\beta=0}^{\infty} \tilde{\Phi}^{(\beta)} x_3^{\beta} \,, \tag{2.19}$$

where $\tilde{U}_i^{(\beta)}$ and $\tilde{\Phi}^{(\beta)}$ are coefficients in the series solution.

The equations in (2.19) are substituted first into (2.15) yielding the following equation:

$$\begin{aligned} &-\sum_{\beta=0}^{\infty} C_{11}\, p^2\, \tilde{U}_1^{(\beta)} x_3^{\beta} + \sum_{\beta=1}^{\infty} (C_{13}+C_{55})\, p\, \beta\, \tilde{U}_3^{(\beta)} x_3^{\beta-1} - \sum_{\beta=0}^{\infty} C_{16}\, p^2 \tilde{U}_2^{(\beta)} x_3^{\beta} \\ &-\sum_{\beta=0}^{\infty} e_{11}\, p^2\, \tilde{\Phi}^{(\beta)} x_3^{\beta} + \sum_{\beta=2}^{\infty} C_{45}\, \beta(\beta-1) \tilde{U}_2^{(\beta)} x_3^{\beta-2} + \sum_{\beta=2}^{\infty} C_{55}\, \beta(\beta-1) \tilde{U}_1^{(\beta)} x_3^{\beta-2} \\ &+\sum_{\beta=2}^{\infty} e_{35}\, \beta(\beta-1) \tilde{\Phi}^{(\beta)} x_3^{\beta-2} = -\sum_{\beta=0}^{\infty} \rho\omega^2\, \tilde{U}_1^{(\beta)} x_3^{\beta} \,. \end{aligned} \tag{2.20}$$

Upon shifting the summation index β to range over 0 to infinity in (2.20) and equating like powers of x_3, we obtain:

$$\begin{aligned} &C_{55}(\beta+2)(\beta+1)\tilde{U}_1^{(\beta+2)} + C_{45}(\beta+2)(\beta+1)\tilde{U}_2^{(\beta+2)} + e_{35}(\beta+2)(\beta+1)\tilde{\Phi}^{(\beta+2)} \\ &= (C_{11}\, p^2 - \rho\omega^2)\tilde{U}_1^{(\beta)} + C_{16}\, p^2\, \tilde{U}_2^{(\beta)} + e_{11}\, p^2 \tilde{\Phi}^{(\beta)} - (C_{13}+C_{55})\, p(\beta+1)\tilde{U}_3^{(\beta+1)} \,. \end{aligned} \tag{2.21}$$

Similarly, by substituting (2.19) into (2.16)-(2.18), shifting the summation index β to range over 0 to infinity and equating like powers of x_3 we obtain

$$\begin{aligned} &C_{45}(\beta+2)(\beta+1)\tilde{U}_1^{(\beta+2)} + C_{44}(\beta+2)(\beta+1)\tilde{U}_2^{(\beta+2)} + e_{34}(\beta+2)(\beta+1)\tilde{\Phi}^{(\beta+2)} \\ &= C_{16}p^2\tilde{U}_1^{(\beta)} + (C_{66}p^2 - \rho\omega^2)\tilde{U}_2^{(\beta)} + e_{16}p^2\tilde{\Phi}^{(\beta)} - (C_{36}+C_{45})p(\beta+1)\tilde{U}_3^{(\beta+1)}, \end{aligned} \tag{2.22}$$

$$\begin{aligned} &C_{33}(\beta+2)(\beta+1)\tilde{U}_3^{(\beta+2)} = (C_{55}p^2 - \rho\omega^2)\tilde{U}_3^{(\beta)} + (C_{13}+C_{55})p(\beta+1)\tilde{U}_1^{(\beta+1)} \\ &+ (C_{36}+C_{45})p(\beta+1)\tilde{U}_2^{(\beta+2)} + (e_{13}+e_{35})p(\beta+1)\tilde{\Phi}^{(\beta+1)}, \end{aligned} \tag{2.23}$$

$$\begin{aligned} &e_{35}(\beta+2)(\beta+1)\tilde{U}_1^{(\beta+2)} + e_{34}(\beta+2)(\beta+1)\tilde{U}_2^{(\beta+2)} - \in_{33}(\beta+2)(\beta+1)\tilde{\Phi}^{(\beta+2)} \\ &= e_{11}p^2 U_1^{(\beta)} + e_{16}p^2 U_2^{(\beta)} - \in_{11}p^2\tilde{\Phi}^{(\beta)} - (e_{13}+e_{35})p(\beta+1)\tilde{U}_3^{(\beta+1)}. \end{aligned} \tag{2.24}$$

The next step in the solution process is to cast (2.21), (2.22), (2.23) and (2.24) into matrix form. This results in the following recurrence relation:

$$\begin{Bmatrix} \tilde{U}_1^{(\beta+2)} \\ \tilde{U}_2^{(\beta+2)} \\ \tilde{U}_3^{(\beta+2)} \\ \tilde{\Phi}^{(\beta+2)} \end{Bmatrix} = \frac{1}{(\beta+2)(\beta+1)}[K]^{-1}[A]\begin{Bmatrix} \tilde{U}_1^{(\beta)} \\ \tilde{U}_2^{(\beta)} \\ \tilde{U}_3^{(\beta)} \\ \tilde{\Phi}^{(\beta)} \end{Bmatrix} + \frac{1}{(\beta+2)}[K]^{-1}[B]\begin{Bmatrix} \tilde{U}_1^{(\beta+1)} \\ \tilde{U}_2^{(\beta+1)} \\ \tilde{U}_3^{(\beta+1)} \\ \tilde{\Phi}^{(\beta+1)} \end{Bmatrix}, \tag{2.25}$$

where

$$[K] = \begin{bmatrix} C_{55} & C_{45} & 0 & e_{35} \\ C_{45} & C_{44} & 0 & e_{34} \\ 0 & 0 & C_{33} & 0 \\ e_{35} & e_{34} & 0 & -\in_{33} \end{bmatrix},$$

$$[A] = \begin{bmatrix} C_{11}p^2 - \rho\omega^2 & C_{16}p^2 & 0 & e_{11}p^2 \\ C_{16}p^2 & C_{66}p^2 - \rho\omega^2 & 0 & e_{16}p^2 \\ 0 & 0 & C_{55}p^2 - \rho\omega^2 & 0 \\ e_{11}p^2 & e_{16}p^2 & 0 & -\in_{11}p^2 \end{bmatrix}, \tag{2.26}$$

$$[B] = \begin{bmatrix} 0 & 0 & -(C_{13}+C_{55})p & 0 \\ 0 & 0 & -(C_{36}+C_{45})p & 0 \\ (C_{13}+C_{55})p & (C_{36}+C_{45})p & 0 & (e_{13}+e_{35})p \\ 0 & 0 & -(e_{13}+e_{35})p & 0 \end{bmatrix}.$$

Equation (2.25) is the recurrence relationship for the series coefficients. This relationship allows for any number of terms to be retained and have only eight unknown coefficients that need to be determined. For example, when β = 0 in (2.25), $\tilde{U}_1^{(2)}, \tilde{U}_2^{(2)}, \tilde{U}_3^{(2)}$ and $\tilde{\Phi}^{(2)}$ can be expressed in terms of $\tilde{U}_1^{(0)}, \tilde{U}_2^{(0)}, \tilde{U}_3^{(0)}, \tilde{\Phi}^{(0)}, \tilde{U}_1^{(1)}, \tilde{U}_2^{(1)}, \tilde{U}_3^{(1)}$ and $\tilde{\Phi}^{(1)}$. Similarly, if β = 1, using $\tilde{U}_1^{(2)}, \tilde{U}_2^{(2)}, \tilde{U}_3^{(2)}$ and $\tilde{\Phi}^{(2)}$, we can express $\tilde{U}_1^{(3)}, \tilde{U}_2^{(3)}, \tilde{U}_3^{(3)}$ and $\tilde{\Phi}^{(3)}$ also in terms of $\tilde{U}_1^{(0)}, \tilde{U}_2^{(0)}, \tilde{U}_3^{(0)}, \tilde{\Phi}^{(0)}, \tilde{U}_1^{(1)}, \tilde{U}_2^{(1)}, \tilde{U}_3^{(1)}$ and $\tilde{\Phi}^{(1)}$. Finding the coefficients when β = 2, 3,... proceeds in the same manner.

The recurrence relation results in eight unknowns for each lamina, namely $\tilde{U}_1^{(0)}, \tilde{U}_2^{(0)}, \tilde{U}_3^{(0)}, \tilde{\Phi}^{(0)}, \tilde{U}_1^{(1)}, \tilde{U}_2^{(1)}, \tilde{U}_3^{(1)}$ and $\tilde{\Phi}^{(1)}$. This implies that for an N-layer laminate, there are $8N$ unknowns to be found. There are four boundary conditions at $x_3 = -H/2$ and $x_3 = H/2$ to be satisfied, namely those specified in equations (2.6) and (2.7). There are also eight conditions at the N-1 interfaces that need to be satisfied (refer to (2.3), (2.4) and (2.5)). This means that there are $8N$ equations that can be used to solve for the $8N$ unknown coefficients.

2.3.1. Determination of Natural Frequencies and Mode Shapes

The natural frequencies and mode shapes of the system are the solution to the free vibration of the simply supported laminated plate with embedded shear actuators. As implied with the term free vibration, there are no loads (mechanical or electrical) applied to the plate. In this case the frequency ω in (2.21), (2.22), (2.23) and (2.24) is unknown.

As is stated in the previous section, there are $8N$ unknowns for an N-layer laminate. Application of all the interface and boundary conditions from (2.3), (2.4), (2.5), (2.6) and (2.7) result in $8N$ algebraic equations. Casting these equations into matrix form results in the following:

$$[M(\omega)]\{V\} = \{0\}, \tag{2.27}$$

where $[M(\omega)]$ is an $8N$ x $8N$ matrix whose elements are polynomials in ω and $\{V\}$ is a column vector of the $8N$ unknowns. As can be seen from (2.27), the determinant of $[M(\omega)]$ must be equal to zero for a non-trivial solution. This results in a polynomial equation in ω whose roots are the eigenvalues of the system that are arranged in ascending order $\{\omega_k^{(1)}, \omega_k^{(2)}, \omega_k^{(3)}, \ldots\}$, which are the natural frequencies corresponding to the longitudinal mode shape defined by the integer k. Corresponding to each eigenvalue, an eigenvector can be found that can be used to compute displacements, stresses, electric potentials and electric displacements that represent the mode shape.

2.3.2. Forced Vibration Analysis

The forced vibration analysis will focus on the steady-state response of the laminated plate due to a harmonic load applied transversely on the top surface. The harmonic load is of the following form:

$$\sigma_{33}(x_1, H/2, t) = q_0 e^{i\omega t} \sin(p x_1), \tag{2.28}$$

where q_0 is a constant that determines the magnitude of the applied load, $e^{i\omega t}$ is the harmonic component and $\sin(p x_1)$ is the variation of the applied load in the x_1-direction. Any loading profile can be written as a Fourier series; therefore, it can be assumed that (2.28) represents a single term in the Fourier series.

The loading profile in (2.28) is a boundary condition for σ_{33} in (2.6). Note that by this form of the loading profile, the terms $e^{i\omega t}$ and $\sin(p x_1)$ are common to the terms in σ_{33} of (2.13). This means that these terms can be dropped from both sides without losing generality. When this boundary condition is used for the forced vibration case, the right-hand side will not be equal to zero

$$[M(\omega)]\{V\} = \{R\}. \tag{2.29}$$

Since the forcing frequency ω is known, the $8N$ unknowns $\{V\}$ are determined by solving the matrix equation (2.29).

2.3.3. Implementation of Positive Position and Velocity Feedback

The second portion of this study will utilize a feedback control algorithm for the purpose of vibration suppression. The exact solution derived in the previous sections does not contain material damping. It is proposed that active vibration damping be introduced into the model using either PPF or velocity feedback.

Implementation of the PPF control is made possible by the assumption that the excitation is harmonic, as well as the fact the only the steady-state solution is of interest. This can be seen if we examine the equations that govern the PPF control law (refer to (1.1) and (1.2)). If we assume that the system coordinate is the displacement $u_3(L/2, H/2)$ the dynamic equation for the compensator becomes:

$$\ddot{\eta} + 2\zeta_c \omega_c \dot{\eta} + \omega_c{}^2 \eta = \omega_c{}^2 u_3(L/2, H/2, t), \tag{2.30}$$

where η the compensator is coordinate, ω_c is the frequency of the compensator and ζ_c is the damping parameter of the compensator.

For steady-state vibration $\eta = \eta_0 e^{i\omega t}$ and $u_3 = u_3{}^0 e^{i\omega t}$. Therefore, (2.30) becomes:

$$-\omega^2 \eta_0 + 2i\omega_c \omega \eta_0 + \omega_c{}^2 \eta_0 = \omega_c{}^2 u_3{}^0 (L/2, H/2). \tag{2.31}$$

Solving for η_0:

$$\eta_0 = \left[\frac{\omega_c{}^2}{\left(\omega_c{}^2 - \omega^2\right) + 2i\zeta_c \omega_c \omega} \right] u_3{}^0 (L/2, H/2). \tag{2.32}$$

The applied feedback potential to the piezoelectric shear actuator is as follows:

$$\phi_0 = g\, \omega_c{}^2 \eta_0, \tag{2.33}$$

where g is the feedback gain. The following potential distribution is applied to the actuator to suppress the vibration:

$$\phi(x_1, t) = \phi_0 e^{i\omega t} \cos(p\, x_1). \tag{2.34}$$

The implementation of the PPF control is very similar to that of the forcing excitation. The feedback potential in (2.34) is applied as a boundary condition in (2.5). Upon applying this condition, the form of the resulting system of equations for the $8N$ unknown coefficients $\{V\}$ is the same as equation (2.29). Since the potential applied to the actuator is a function of the transverse displacement $u_3(L/2, H/2, t)$, the feedback law appears in the left-hand side matrix $[M(\omega)]$ of (2.29). The right-hand side vector $\{R\}$ depends only on the amplitude of the applied harmonic load q_0. The unknown coefficients are determined by solving the linear system of equations (2.29). Once the coefficients are determined, the displacements, electric potential, stresses and electric displacement can be determined.

The velocity feedback algorithm is implemented in a manner very similar to that of PPF. The only difference is that the transverse velocity is used instead of the transverse displacement as in the PPF control law. The dynamic equation for the compensator becomes:

$$\ddot{\eta} + 2\zeta_c \omega_c \dot{\eta} + \omega_c^2 \eta = \omega_c^2 \dot{u}_3(L/2, H/2, t). \tag{2.35}$$

Upon assuming $\eta = \eta_0 e^{i\omega t}$ and $u_3 = u_3^0 e^{i\omega t}$ for the steady-state response, we obtain the following expression for η_0:

$$\eta_0 = \left[\frac{i\omega\omega_c^2}{(\omega_c^2 - \omega^2) + 2i\zeta_c \omega_c \omega} \right] u_3^0(L/2, H/2). \tag{2.36}$$

In order to effectively utilize velocity feedback control, the gain must be negative. This results in the following expression:

$$\phi_0 = -G\omega_c^2 \eta_0. \tag{2.37}$$

The rest of the feedback control implementation is exactly the same as that for PPF control.

2.4. Finite Element Solution

The natural frequencies of the hybrid plates are also computed by the finite element method using the commercial finite element package ABAQUS/Standard 6.3-1 (Hibbitt, Karlsson & Sorensen, Inc., 2002) to ensure that no algebraic errors were made during the implementation of the exact solution. A plane strain analysis is performed, assuming that $u_2 = 0$ and u_1, u_3 and ϕ are functions of x_1, x_3 and t. ABAQUS does have an elastic generalized plane strain element, but lacks a generalized plane strain

piezoelectric element. Therefore, the out-of-plane mode shapes with non-zero displacement component u_2 cannot be computed using ABAQUS.

The natural frequencies of the plates with various length-to-thickness ratios are extracted using the Lanczos method. The other method offered by ABAQUS is a subspace iteration eigenvalue extraction. The Lanczos method is preferred in this instance because it is typically faster when the system contains a large number of degrees-of-freedom.

The elements used in the analysis are CPE8R and CPE8RE for the linear elastic and piezoelectric materials, respectively. The CPE8R is a general 2D 8-node biquadratic plane strain element with reduced integration. The CPE8RE is a 2D piezoelectric 8-node biquadratic plane strain element with reduced integration. A convergence study using a single mesh refinement showed that the fundamental frequency did not change in any of the significant figures. A detailed convergence study was not performed since the finite element results are used only as an algebraic check. The number of elements and nodes for all the finite element studies were kept constant at 15,700 elements and 47,877 nodes.

2.5. Results and Discussion

In the first portion of this study we analyze the free vibration of several piezoelectric and composite plates. The natural frequencies and mode shapes are the result of a free vibration analysis. System identification is very important to any vibration suppression control scheme. Once the natural frequencies and mode shapes are known, vibration suppression using both PPF and velocity feedback is undertaken to determine the influence of the control parameters on the system damping. (Note that the analytical implementation of the exact solution can be found in Appendix A.)

Table 2.1. Non-vanishing material properties of the Gr-Ep and PZT-5A

Property	0° Gr-Ep	± 45° Gr-Ep	0° PZT-5A	45° PZT-5A
C_{11} (GPa)	183.443	58.128	86.856	93.003
C_{22} (GPa)	11.662	58.182	99.201	93.003
C_{33} (GPa)	11.662	11.622	99.201	99.201
C_{12} (GPa)	4.363	43.788	50.788	50.803
C_{13} (GPa)	4.363	4.140	50.788	52.397
C_{23} (GPa)	3.918	4.140	54.016	52.397
C_{44} (GPa)	2.870	5.020	22.593	21.847
C_{55} (GPa)	7.170	5.020	21.100	21.847
C_{66} (GPa)	7.170	46.595	21.000	21.126
C_{16} (GPa)	0	± 42.945	0	-3.086
C_{26} (GPa)	0	± 42.945	0	-3.086
C_{36} (GPa)	0	± 0.222	0	-1.619
C_{45} (GPa)	0	± 2.150	0	-0.7465
e_{11} (C m^{-2})	0	0	15.118	11.510
e_{12} (C m^{-2})	0	0	-7.209	-5.917
e_{13} (C m^{-2})	0	0	-7.209	-5.098
e_{16} (C m^{-2})	0	0	0	7.894
e_{21} (C m^{-2})	0	0	0	-5.917
e_{22} (C m^{-2})	0	0	0	11.510
e_{23} (C m^{-2})	0	0	0	-5.098
e_{26} (C m^{-2})	0	0	12.322	7.894
e_{34} (C m^{-2})	0	0	0	8.713
e_{35} (C m^{-2})	0	0	12.322	8.713
ϵ_{11} (10^{-10} F m^{-1})	153.0	153.0	150.0	151.5
ϵ_{22} (10^{-10} F m^{-1})	153.0	153.0	153.0	151.5
ϵ_{33} (10^{-10} F m^{-1})	153.0	153.0	153.0	153.0
ϵ_{12} (10^{-10} F m^{-1})	0	0	0	-1.50
ρ (kg/m^3)	1590	1590	7750	7750

The laminae of the plates are assumed to be either graphite-epoxy (Gr-Ep) or PZT-5A. The properties for these materials can be found in Table 2.1. This data is the same as that used by Vel and Batra (2001a). The principal axes for both materials are assumed to vary within the x_1-x_2 plane. The principal axis is denoted by $\theta°$ preceding the material designation. The material properties listed are that for 0° Gr-Ep, ● 45° Gr-Ep, 0° PZT-5A and 45° PZT-5A.

2.5.1. Results for a [0° Gr-Ep/0° PZT-5A/0° Gr-Ep] Plate

A three-layer laminated composite comprised of 0° PZT-5A sandwiched in between two layers of 0° Gr-Ep is considered. The exact configuration of the system is shown in Figure 2.2.

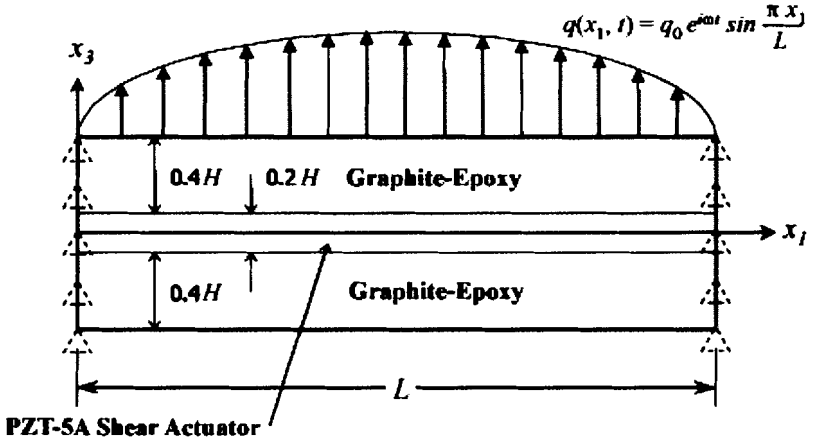

Figure 2.2. The geometrical configuration of the three-layer hybrid laminate

As can be seen from Figure 2.2, 80% of the laminate in the thickness direction is comprised of Gr-Ep, and the remaining material is the piezoelectric shear actuator. Figure 2.2 displays a forcing function applied to the top surface of the plate, but this will not be used to ascertain the natural frequencies and mode shapes. It will be used later for vibration suppression using feedback control.

The natural frequencies and mode shapes for a [0° Gr-Ep/0° PZT-5A/0° Gr-Ep] plate that is 0.25 m in length are computed for three different length-to-thickness ratios of 4, 10 and 100. There are also two different electrical boundary conditions considered at $x_3 = 0.1\ H$, $-0.1\ H$. The boundary is either considered electrically closed ($\phi = 0$) or open (D_3=0). Finite element results obtained for this case are listed in parenthesis below the exact values. Again, a plane strain analysis is performed and any modes that have movement in the x_2-direction cannot be computed using ABAQUS. The first twelve natural frequencies for a [0° Gr-Ep/0° PZT-5A/0° Gr-Ep] plate are listed in Table 2.2 for three different length-to-thickness ratios.

Table 2.2. The first twelve natural frequencies of a [0° Gr-Ep/0° PZT-5A/0° Gr-Ep] plate

L/H = 4				*L/H* = 10				*L/H* = 100			
Mode	Closed, Hz	Mode	Open, Hz	Mode	Closed, Hz	Mode	Open, Hz	Mode	Closed, Hz	Mode	Open, Hz
$\omega_1^{(1)}$	2449.9 (2449.9)	$\omega_1^{(1)}$	2483.73 (2483.7)	$\omega_1^{(1)}$	1328.91 (1328.9)	$\omega_1^{(1)}$	1334.23 (1334.2)	$\omega_1^{(1)}$	145.057 (145.06)	$\omega_1^{(1)}$	145.064 (145.06)
$\omega_1^{(2)}$	3752.27 (--)	$\omega_1^{(2)}$	3752.27 (--)	$\omega_1^{(2)}$	3755.9 (--)	$\omega_1^{(2)}$	3755.9 (--)	$\omega_2^{(1)}$	578.545 (578.55)	$\omega_2^{(1)}$	578.655 (578.66)
$\omega_2^{(1)}$	6085.51 (6085.5)	$\omega_2^{(1)}$	6219.85 (6219.9)	$\omega_2^{(1)}$	4367.51 (4367.5)	$\omega_2^{(1)}$	4415.16 (4415.2)	$\omega_3^{(1)}$	1295.49 (1295.5)	$\omega_3^{(1)}$	1296.04 (1296.0)
$\omega_2^{(2)}$	7479.11 (--)	$\omega_2^{(2)}$	7479.11 (--)	$\omega_2^{(2)}$	7507.64 (--)	$\omega_2^{(2)}$	7507.64 (--)	$\omega_4^{(1)}$	2287.84 (2287.8)	$\omega_4^{(1)}$	2289.53 (2289.5)
$\omega_3^{(1)}$	9678.38 (9678.4)	$\omega_3^{(1)}$	9931.1 (9931.1)	$\omega_3^{(1)}$	7931.9 (7931.9)	$\omega_3^{(1)}$	8060.28 (8060.3)	$\omega_5^{(1)}$	3544.82 (3544.8)	$\omega_5^{(1)}$	3548.85 (3548.8)
$\omega_3^{(2)}$	11158.1 (--)	$\omega_3^{(2)}$	11158.1 (--)	$\omega_3^{(2)}$	11251.1 (--)	$\omega_3^{(2)}$	11251.1 (--)	$\omega_1^{(2)}$	3756.58 (--)	$\omega_1^{(2)}$	3756.58 (--)
$\omega_4^{(1)}$	13238.5 (13239)	$\omega_4^{(1)}$	13625.6 (13626)	$\omega_4^{(1)}$	11580.3 (11580)	$\omega_4^{(1)}$	11808.1 (11808)	$\omega_6^{(1)}$	5053.35 (5053.3)	$\omega_6^{(1)}$	5061.46 (5061.5)
$\omega_1^{(3)}$	13368.6 (13369)	$\omega_1^{(4)}$	13684.7 (--)	$\omega_1^{(3)}$	14674.1 (14674)	$\omega_1^{(3)}$	14907.4 (14907)	$\omega_7^{(1)}$	6798.55 (6798.6)	$\omega_7^{(1)}$	6813.07 (6813.1)
$\omega_1^{(4)}$	13684.7 (--)	$\omega_1^{(3)}$	13689.7 (13689)	$\omega_4^{(2)}$	14982.4 (--)	$\omega_4^{(2)}$	14982.4 (--)	$\omega_2^{(2)}$	7513.13 (--)	$\omega_2^{(2)}$	7513.13 (--)
$\omega_4^{(2)}$	14773.4 (--)	$\omega_4^{(2)}$	14773.4 (--)	$\omega_5^{(1)}$	15213.8 (15214)	$\omega_5^{(1)}$	15549.6 (15550)	$\omega_8^{(1)}$	8764.26 (8764.3)	$\omega_8^{(1)}$	8788.09 (8788.1)
$\omega_5^{(1)}$	16777.4 (16777)	$\omega_1^{(5)}$	17156 (--)	$\omega_5^{(2)}$	18697.8 (--)	$\omega_5^{(2)}$	18697.8 (--)	$\omega_9^{(1)}$	10933.5 (10934)	$\omega_9^{(1)}$	10970.1 (10970)
$\omega_1^{(5)}$	17156 (--)	$\omega_5^{(1)}$	17315.3 (17315)	$\omega_6^{(1)}$	18821.2 (18821)	$\omega_6^{(1)}$	19271 (19271)	$\omega_3^{(2)}$	11269.6 (--)	$\omega_3^{(2)}$	11269.6 (--)

From Table 2.2, it is evident that the finite element solution agrees very well with the exact solution. This also verifies that no algebraic mistakes were made while

computing the exact solution. There are six modes that have displacement in the x_2-direction for $L/H = 4$, which cannot be found using a plane strain finite element analysis.

The electrical boundary condition for the piezoelectric material plays an important role, as can be seen in Table 2.2. In fact, the order of the modes changes as a result of the boundary condition when the length-to-thickness ratio is 4. The modes $\omega_5^{(1)}$ and $\omega_1^{(5)}$ change from modes 11 and 12, when the electric boundaries are closed, to modes number 12 and 11, respectively, when the electric boundaries are open. This stresses the importance of prescribing the correct electrical boundary conditions for the piezoelectric layers.

2.5.2. Results for a [45° Gr-Ep/0° PZT-5A/-45° Gr-Ep] Plate

We now consider an unsymmetric [45° Gr-Ep/0° PZT-5A/-45° Gr-Ep] composite that is 0.25 m in length. The off-axis orientations of the top and bottom fiber-reinforced Gr-Ep layers will introduce strong coupling of the deformation in the x_1-x_3 plane to that in the x_2-direction. The first twelve natural frequencies of the [45° Gr-Ep/0° PZT-5A/-45° Gr-Ep] plate are given in Table 2.3 for a thick plate with length-to-thickness ratio of 4. As for the previous case, two different electrical boundary conditions are considered for the piezoelectric material. The interfaces at 0.1 H and -0.1 H are either electrically closed ($\phi = 0$) or open (D_3=0). An ABAQUS finite element solution is not given due to the anisotropic nature of the problem.

Table 2.3. The first twelve natural frequencies of a [45° Gr-Ep/0° PZT-5A/-45° Gr-Ep] plate

$L/H = 4$			
Mode	Closed, Hz	Mode	Open, Hz
$\omega_1^{(1)}$	1210.29	$\omega_1^{(1)}$	1212.93
$\omega_2^{(1)}$	3786.37	$\omega_2^{(1)}$	3805.64
$\omega_3^{(1)}$	6721.76	$\omega_3^{(1)}$	6770.05
$\omega_1^{(2)}$	6936.61	$\omega_1^{(2)}$	6971.56
$\omega_1^{(3)}$	8186.22	$\omega_1^{(3)}$	8559.04
$\omega_4^{(1)}$	9733.10	$\omega_4^{(1)}$	9818.43
$\omega_2^{(2)}$	11881.4	$\omega_2^{(2)}$	12003.6
$\omega_5^{(1)}$	12758.8	$\omega_5^{(1)}$	12886.8
$\omega_2^{(3)}$	13631.9	$\omega_2^{(3)}$	14171.2
$\omega_1^{(4)}$	15583.7	$\omega_1^{(4)}$	15661.4
$\omega_6^{(1)}$	15788.9	$\omega_6^{(1)}$	15963.9
$\omega_1^{(5)}$	15893.9	$\omega_1^{(5)}$	15955.2

As can be seen from Table 2.3, the electrical boundary condition has a profound effect on the natural frequency corresponding to certain modes. For example, $\omega_1^{(3)}$ changes from 8186.22 Hz to 8559.04 Hz by altering the electrical boundary condition from closed to open.

The mode shapes corresponding to the first twelve closed natural frequencies in Table 2.3 are depicted in Figure 2.3. Again, the plate extends to infinity in the x_2-direction, but the plate has been truncated in the illustrations.

The effect of the unsymmetric laminate is very evident in Figure 2.3. For example, Figure 2.3(i) is a thickness mode in which the thickness vibration induces a shearing motion in the x_2-x_3 plane due to the elastic coupling introduced by the off-axis Gr-Ep layers. The rest of the mode shapes in Figure 2.3 also exhibit coupling, although it may be hard to discern from the plots.

The nonlinearity of the u_1-displacement in the mode of Figure 2.3(k) is very apparent from the plot. This further shows that a classical plate theory is not adequate enough to predict behavior such as this. Therefore, a higher-order theory is needed for any of the higher modes.

The results presented in Figure 2.4 are the displacements and electric potential profiles through the thickness of the first nine closed natural frequencies found in Table 2.3. The displacements and electric potential are normalized by their maximum value for the plots. The displacements and stresses were computed using 35 terms in the series solution to obtain accurate values for the plots.

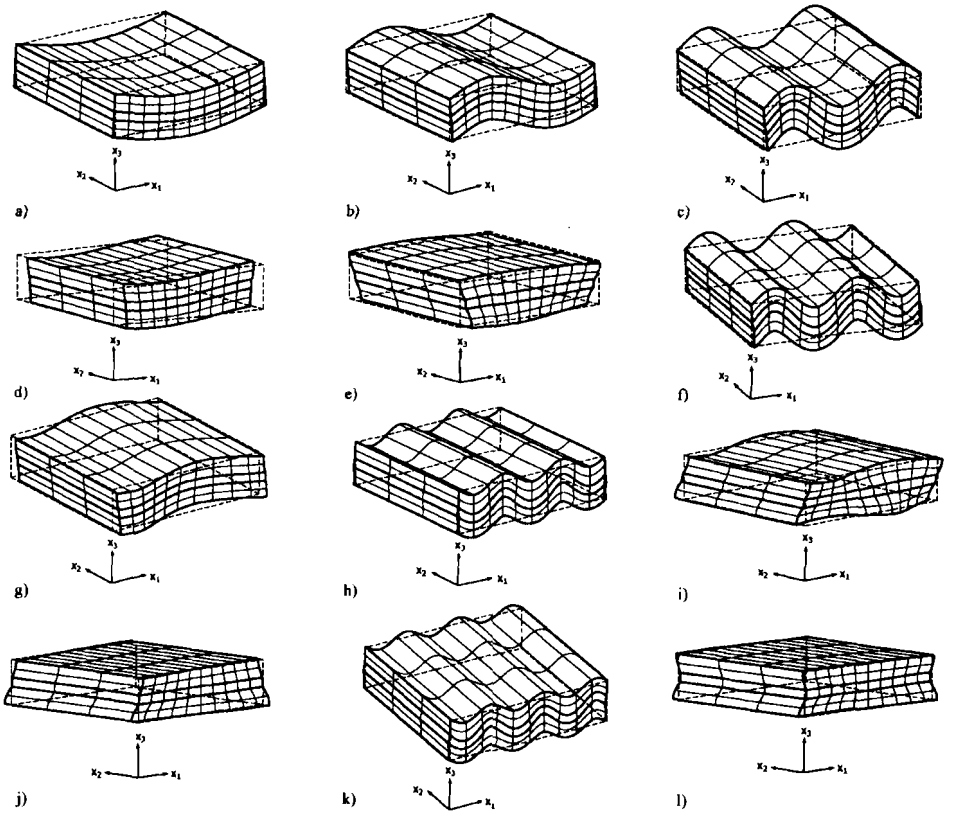

Figure 2.3. The first twelve natural frequencies of an electrically closed [45° Gr-Ep/0° PZT-5A/-45° Gr-Ep] plate

As can be seen in Figure 2.4(h) for $\omega_4^{(1)}$, the u_1-displacement is highly nonlinear for the three-layer laminated composite with an embedded piezoelectric shear actuator. A linear approximation would result in gross errors in the solution. In fact, the solution starts to deviate from a fairly linear profile in Figure 2.4(b). In addition, the transverse displacement u_3 has a non-constant profile through the thickness for the higher modes, such as that in Figure 2.4(h). The u_2-displacement also exhibit nonlinearities for the higher modes.

The through-the-thickness plots for the stresses σ_{11}, σ_{12}, σ_{33} and σ_{13} are given in Figure 2.5 for the first nine electrically closed modes listed to Table 2.3. The longitudinal normal stress σ_{11} is highly nonlinear in the Gr-Ep face sheets in Figures 2.5(d), 2.5(e), 2.5(f), 2.5(g), 2.5(h) and 2.5(i). This implies that a classical plate type theory would not give accurate results for most of the modes listed in Figure 2.5. The longitudinal stress is fairly linear through the piezoelectric layer, however.

The plate exhibits the expected profile for the transverse shear stress σ_{13} that one would expect in Figures 2.5(a), 2.5(b), 2.5(c), 2.5(f) and 2.5(h), which is nearly a parabolic shape within each layer. The plate exhibits a zigzag pattern for the transverse shear stress in Figures 2.5(e) and 2.5(i). The stress component σ_{13} appears to be constant though the piezoelectric material in Figures 2.5(d) and 2.5(g), and the stress component has a linear trend through the Gr-Ep face sheets.

It is also interesting to note that the transverse normal stress σ_{33} is nearly linear in the piezoelectric layer in Figures 2.5(a)-2.5(d) and 2.5(f)-2.5(h). This trend is different from the case of a monolithic PZT-5A plate, where the through-the-thickness variation of the transverse normal stress is cubic.

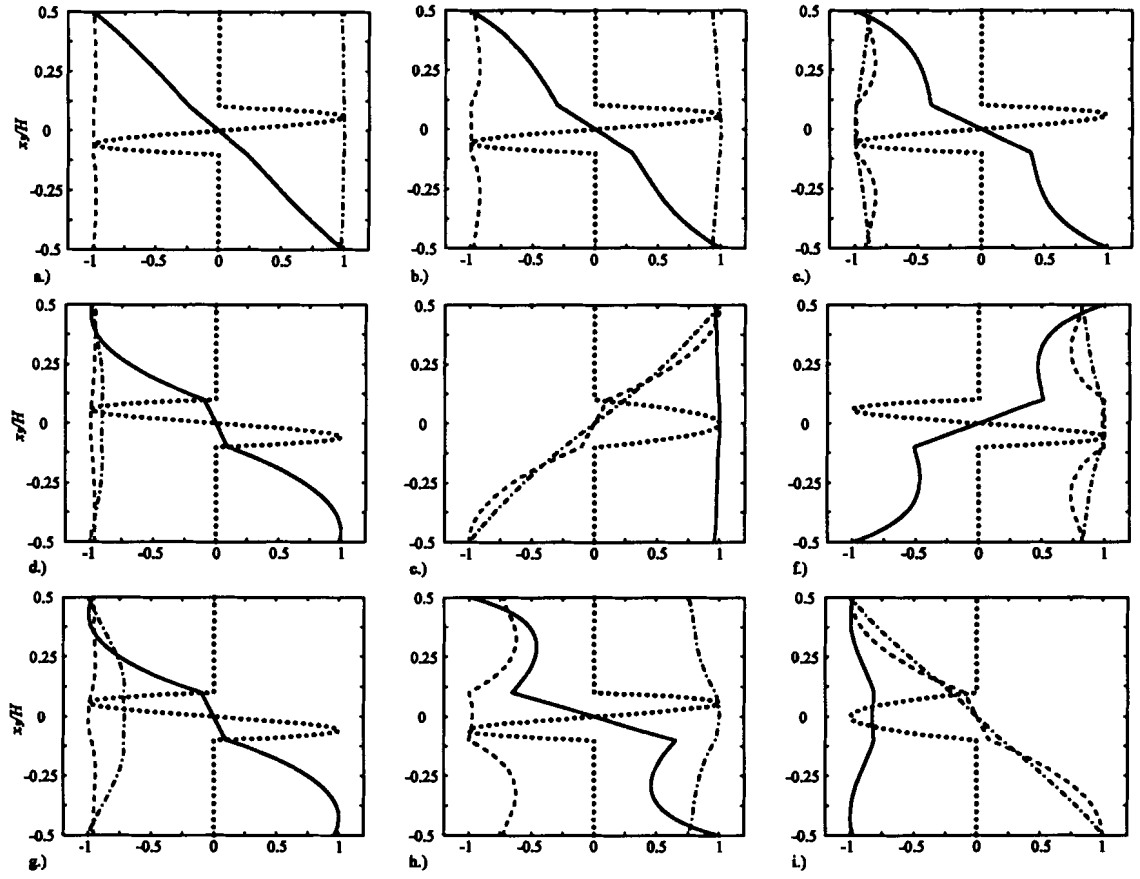

Figure 2.4. Displacements and potential profiles of the first nine modes of an electrically closed [45° Gr-Ep/0° PZT-5A/-45° Gr-Ep] hybrid laminate: ____ $\frac{u_1(0,x_3)}{Max|u_1(0,x_3)|}$; - - - $\frac{u_2(0,x_3)}{Max|u_2(0,x_3)|}$; -.-.- $\frac{u_3(L/2,x_3)}{Max|u_3(L/2,x_3)|}$; ..... $\frac{\phi(0,x_3)}{Max|\phi(0,x_3)|}$

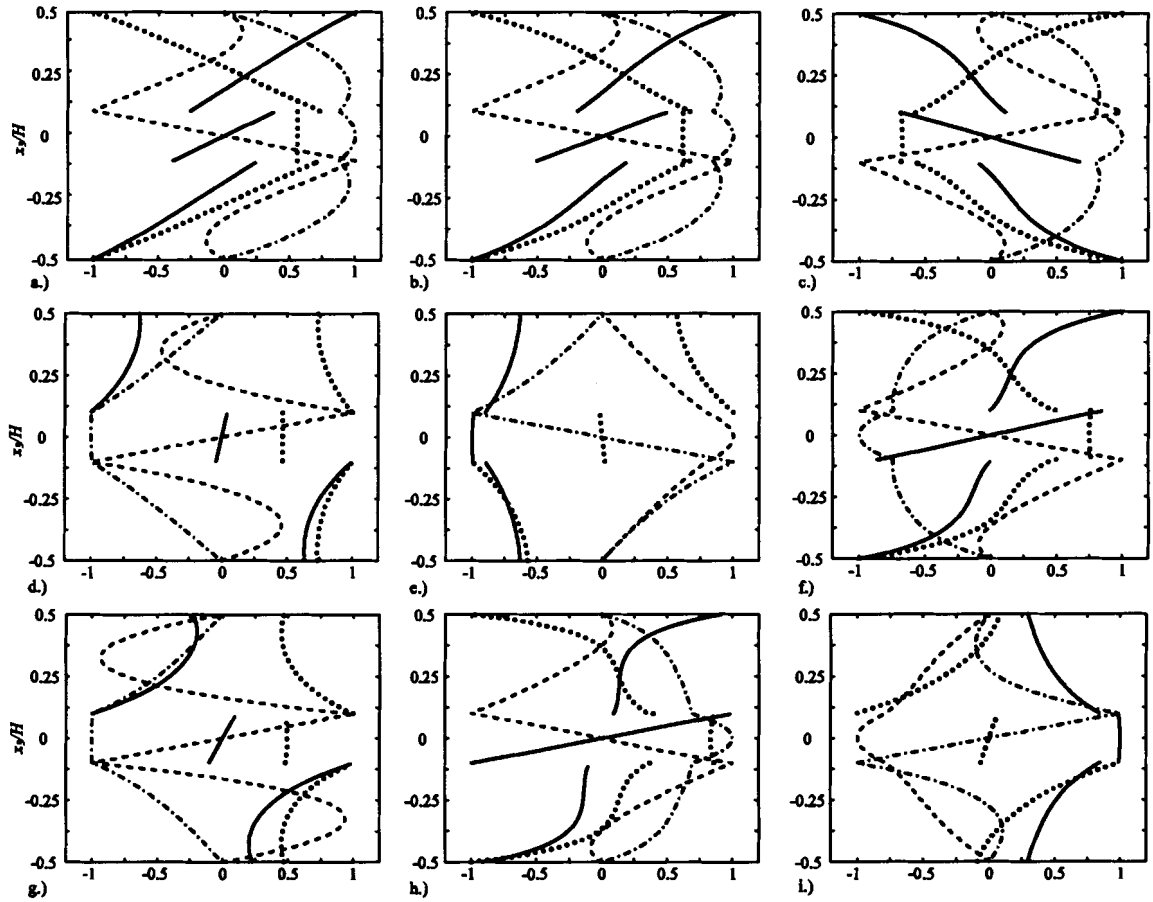

Figure 2.5. Stress profiles of the first nine modes of an electrically closed [45° Gr-Ep/0° PZT-5A/-45° Gr-Ep] hybrid laminate: ____ $\frac{\sigma_{11}(L/2,x_3)}{Max|\sigma_{11}(L/2,x_3)|}$; - - - $\frac{\sigma_{33}(L/2,x_3)}{Max|\sigma_{33}(L/2,x_3)|}$; -·-·- $\frac{\sigma_{12}(L/2,x_3)}{Max|\sigma_{12}(L/2,x_3)|}$; ····· $\frac{\sigma_{13}(0,x_3)}{Max|\sigma_{13}(0,x_3)|}$

2.5.3. Results of the Vibration Suppression of a [0° Gr-Ep/0° PZT-5A/0° Gr-Ep] Plate Using PPF Control

In this section, we present exact results for vibration damping of composite plates using the embedded piezoelectric actuators and PPF control. The first step in the procedure is to determine the steady-state response of the system due to a harmonic distributed load on the top surface of the plate. Section 2.3.3 contains details of implementation, and Figure 2.2 depicts the geometry of the system. Once this is accomplished, the vibration control algorithm is implemented by imposing a potential electrical boundary condition to the piezoelectric actuator in the form of (2.34).

We consider the vibration suppression of the [0° Gr-Ep/0° PZT-5A/0° Gr-Ep] plate analyzed earlier. The length-to-thickness ratio is chosen to be 10. The control voltage is applied to the top surface of the piezoelectric layer at $x_3 = 0.1H$, and the bottom surface at $x_3 = -0.1H$ is assumed to be electrically grounded. The goal of the analysis is to (a) investigate whether shear actuation mechanism is effective for vibration suppression and (b) determine the effect of the PPF control parameters on the applied system damping of a continuous system. The analysis will consist of determining the amplitude of the transverse displacement of the plate as a function of the forcing frequency. The result is presented in the form of a frequency response curve near the fundamental frequency.

The PPF control parameter comparison is accomplished by choosing a compensator baseline from which each parameter is individually changed. The baseline system consists of choosing a compensator frequency ω_c equal to the system frequency, the compensator damping paramter ζ_c to be 0.05 and the scalar gain g to be equal to

0.1 V s^2 / m. From Table 2.2, the fundamental frequency of the [0° Gr-Ep/0° PZT-5A/0° Gr-Ep] plate with an electrically closed boundary condition is 1328.91 Hz. Next, the compensator frequency is altered to be equal to $1.1\omega_n$, $1.35\omega_n$ and $1.4\omega_n$, while maintaining the same values for the other compensator variables. Note that ω_n is referring to the mode being targeted for vibration suppression. Next, the compensator damping ratio is changed from 0.05 to 0.15, then to 0.35 and finally to 0.5. This encompasses the entire range usually recommended (refer to Section 1.2.3). Lastly, the compensator gain is changed from 0.1 V s^2 / m to 0.45 V s^2 / m, 0.65 V s^2 / m and 0.9 V s^2 / m.

The influence of the PPF compensator parameters on the frequency response function can be found in Figure 2.6. Shown on the left are the comparison plots of the magnitude of the u_3-displacement at $x_1 = L/2$ and $x_3 = H/2$. The magnitude is normalized by q_0, L and C_0, which have values of 1 Pa, 0.25 m and 21.1 GPa, respectively. Immediately to the right of these plots are phase curves of u_3 relative to the applied load.

As can be seen from Figure 2.6(a), maximum system damping is achieved when the compensator frequency is set equal to the fundamental frequency of the system. This value is not recommended by other experimenters, however, who choose either $1.3\omega_n$ or $1.45\omega_n$ (refer to Section 1.2.3). This could be attributed to the fact that in the present analysis the system does not contain any damping of its own. This causes the system to be in perfect phase with the forcing frequency when the compensator is not active. Therefore, to counter all of the motion of the forcing function, the voltage applied to the piezoelectric actuator must respond exactly as the system.

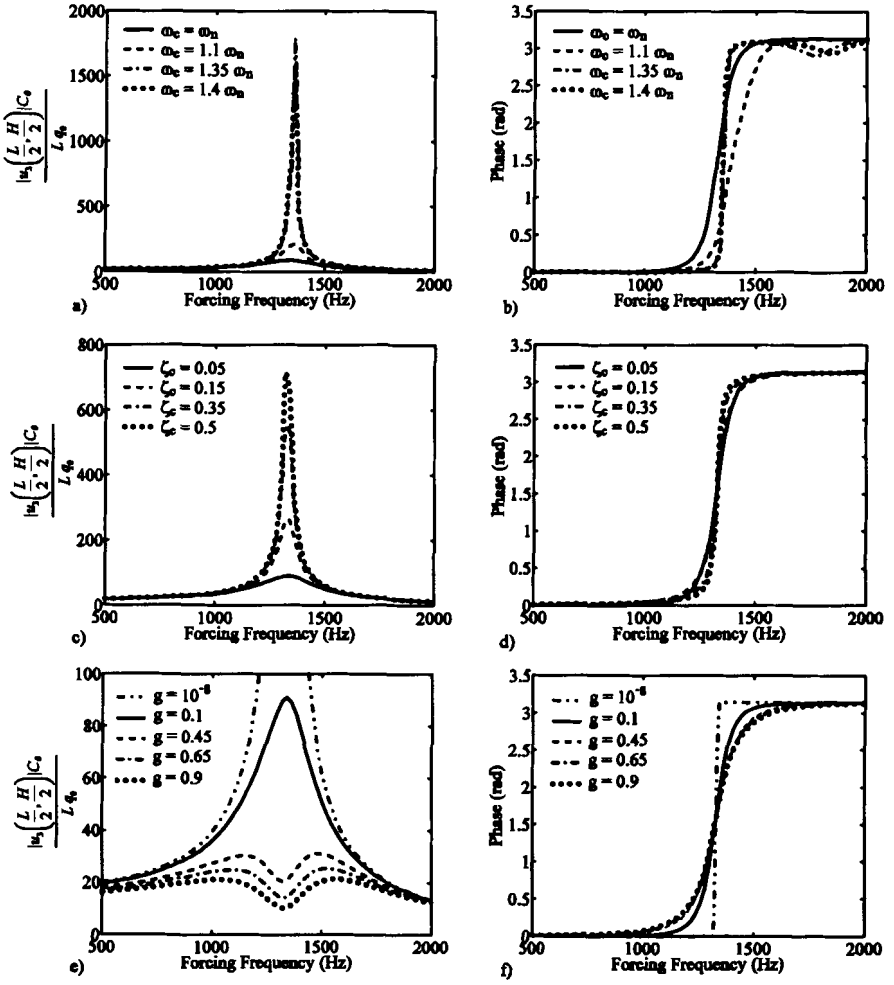

Figure 2.6. PPF compensator variable comparison plots of magnitude and phase for the first flexural mode

The compensator damping ratio has some interesting effects to the response of the system, as can be seen in Figure 2.6(b). The larger the compensator damping parameter, the less damping the system achieves. This fact is also discussed by Song *et al.* (2002). This phenomenon is explained by the fact that as the compensator damping is reduced, the damping of the system will increase, but as a tradeoff the bandwidth of the PPF control is reduced. Therefore, the system response needs to be fully understood. In most cases, however, the response will change with time, due to such things as damage, temperature, etc. The most effective system must be found by allowing for an adequate control range while maximizing damping.

The response of the system due to changes in the gain g is fairly evident from Figure 2.6(c). As the gain is increased, more potential is applied to the actuator, which increases the system damping. An interesting phenomenon occurs once the gain reaches 0.45 V s^2 / m. The transverse displacement at the hybrid plate's fundamental frequency (1328.91 Hz) is less than the response of the system at frequencies equal to 1000 Hz or 1500 Hz. This is a result of extremely targeted vibration suppression. This parameter is more a function of the highest amount of potential that can be applied to the PZT actuator. This can be caused by limitations of the power amplifier, dielectric breakdown concerns, etc.

Next, vibration suppression of the first thickness mode is analytically performed. The vibration control of this mode with the piezoelectric shear actuator utilizes a non-zero electric field component E_1 and the piezoelectric coefficient e_{13} to influence the transverse strain ε_{33}. The study is performed in exactly the same manner as described

above. A base PPF compensator is identified, and then each control parameter is changed individually to see the effect each has on the feedback performance.

As before, the base compensator consists of a filter damping ratio of 0.05, filter frequency equal to the target natural frequency (first thickness mode, 14674.1 Hz), and a scalar gain of 0.1 V s^2 / m. The filter damping ratio is altered from being equal to 0.05 to 0.15, 0.35 and finally 0.5. The target frequency is altered from being equal to the first thickness mode frequency to 110%, 135% and 140% of that value. Finally, the gain g is changed from 0.1 V s^2 / m to 0.45 V s^2 / m, 0.65 V s^2 / m and 0.9 V s^2 / m. Using the exact same comparison values for the suppression of the thickness mode as that of the first flexural mode will allow a separate comparison between the performances in both cases. However, they can be compared only in a relative sense due to the amplitude difference between each mode.

Comparison plots of the compensator performance for the first thickness mode can be found in Figure 2.7. As can be seen in Figure 2.7, the forcing frequency is from 14200 Hz to 15000 Hz. The magnitude of the u_3-displacement at $x_1 = L/2$ and $x_3 = H/2$ is normalized by the values C_0, q_0 and L, which have values of 21.1 GPa, 1 Pa and 0.25 m, respectively. Plots of the non-dimensional displacement $|u_3(L/2,H/2)\ C_0 / L\ q_0|$ versus forcing frequency can be found in Figures 2.7(a), 2.7(c) and 2.7(e). The phase difference between the system response and forcing frequency can be found immediately to the right of the frequency response curves. Note that g in Figures 2.7(e) and 2.7(f) has units of V s^2 / m.

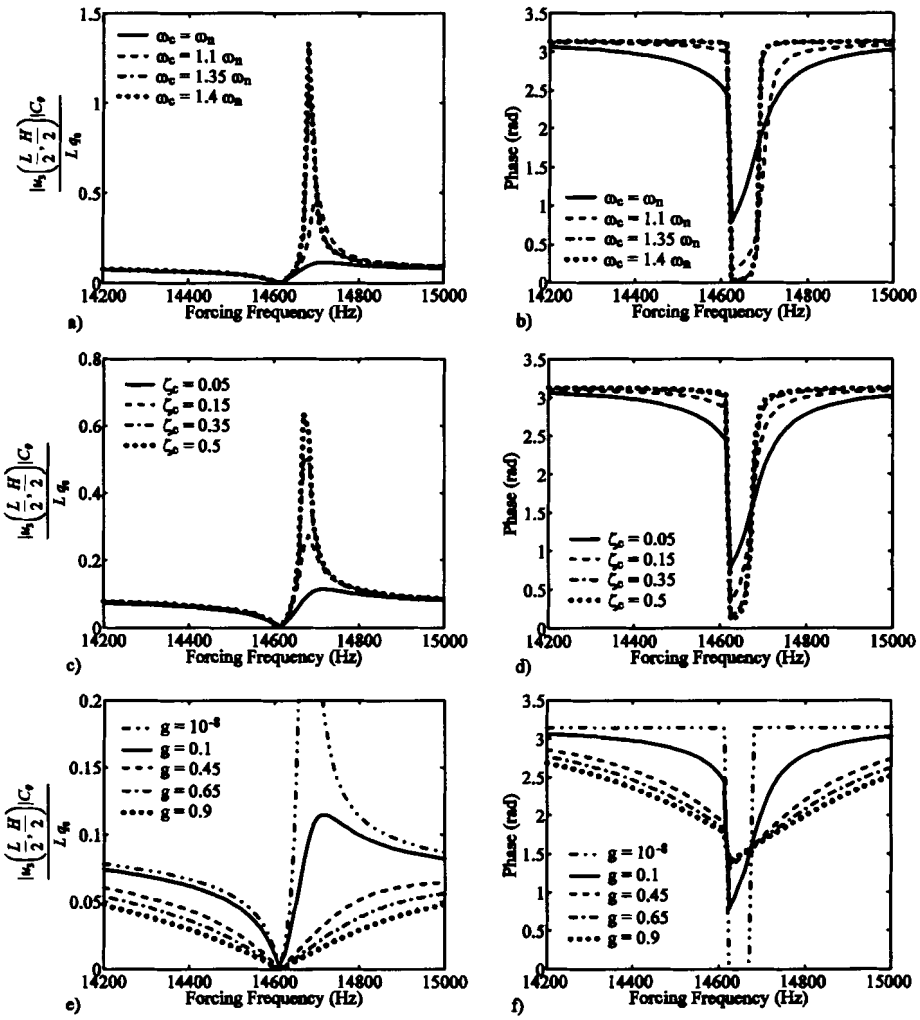

Figure 2.7. PPF compensator variable comparison plots of magnitude and phase for the suppression of the first thickness mode

As can be seen from Figure 2.7, vibration suppression of a thickness mode using a PPF control algorithm is feasible. The trends, as far as the compensator variables are concerned, are very similar to that of the control of the first bending mode. For example, as the compensator damping is increased, the damping of the system decreases. This, however, is a result of the compensator itself; therefore, it would make sense for this factor to be independent of the mode being controlled. Also, as the compensator frequency ω_c is increased the system response gets larger.

The effect of the increased gain on the PPF controller performance for suppressing the first thickness mode is as expected. As the gain is increased, larger amounts of potential are applied to the PZT-5A actuator, which results in superior vibration suppression. It is interesting to note that the system peak response at the natural frequency seems to disappear as g attains a value of 0.45 V s^2 / m.

The hybrid plate exhibits an interesting response when the forcing frequency is 14613.7 Hz as shown in Figure 2.7. The transverse deflection $|u_3(L/2,H/2)\ C_0 / L\ q_0|$ attains a value of 5.944×10^{-3} at this point with no active feedback control. Also, there is a discrete phase shift at this frequency. This phenomenon where there is a local minimum of system response is known as anti-resonance.

2.5.4. Results of the Vibration Suppression of a [0° Gr-Ep/0° PZT-5A/0° Gr-Ep] Plate Using Velocity Feedback Control

We now consider the vibration suppression of the [0° Gr-Ep/0° PZT-5A/0° Gr-Ep] plate using a velocity feedback control algorithm. The steady-state solution is the only dynamic component studied. The implementation of this routine follows the

derivation outlined in Section 2.3.3. Similar to the PPF implementation, the feedback control utilizes the velocity at $x_1=L/2$ and $h=H/2$, and impose an electric potential interface condition at $h = 0.1\,H$ in the form of (2.37).

The variables of the velocity feedback control are very similar to that of the PPF compensator. The base variables used are 0.05 for the control damping ratio ζ_c, filter frequency ω_c equal to the fundamental frequency of the system, and a gain parameter G of 1×10^{-5} V s^3 / m. All the variables, except the parameter G, are altered in exactly the same way as that for the PPF variable comparison (refer to Section 2.5.3). In this comparison, the gain parameter G is changed from the base value to 0.8×10^{-5} V s^3 / m, 1.5×10^{-5} V s^3 / m and 2×10^{-5} V s^3 / m.

The variable comparison for the velocity feedback control algorithm can be found in Figure 2.8. Normalized plots of the u_3-displacement are shown in Figures 2.8(a), 2.8(c) and 2.8(e), with corresponding plots of the phase differences immediately to the right. The magnitude is normalized by q_0, L and C_0, which all have values of 1 Pa, 0.25 m and 21.1 GPa, respectively. Note that G in Figures 2.8(e) and 2.8(f) has units of V s^3 / m.

As can be seen from Figure 2.8, the velocity feedback control behaves similar to that of the PPF control algorithm. For example, in Figure 2.8(a) the system response gets larger with increasing compensator frequency ω_c. There is one noticeable difference, however. As the compensator frequency is increased, the peak system response does not increase as dramatically as is seen with PPF control. This means that the velocity feedback controller has a larger bandwidth than the PPF compensator.

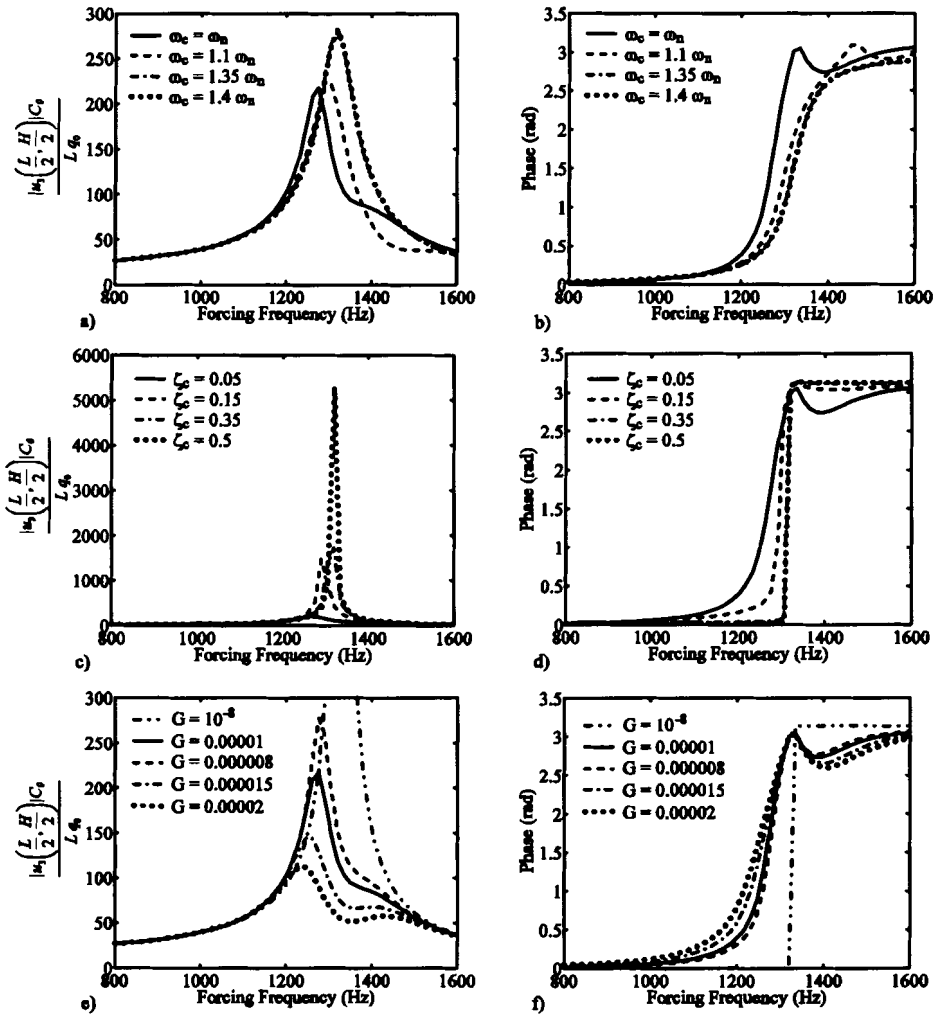

Figure 2.8. Velocity feedback variable comparison plots of magnitude and phase

The velocity feedback controller damping parameter has a large influence on the system dynamics. As the damping parameter ζ_c increases, the system response also increases. This phenomenon was also seen in the PPF control analysis, but not to the extent seen in Figure 2.8(b).

As can be seen in Figure 2.8(c), the velocity feedback control algorithm behaves similarly to that of the PPF control when the gain is increased. As the gain becomes larger, the amplitude at the target frequency gets smaller. There is one notable difference, however. The frequency response curves in Figure 2.8(c) are not symmetric, with respect to the resonance point, like those found in Figure 2.6(c).

Chapter 3

ANALYSIS OF STATIC DEFLECTION, VIBRATION AND ACTIVE DAMPING OF CYLINDRICAL COMPOSITE SHELLS WITH EMBEDDED PIEZOELECTRIC SHEAR ACTUATORS

3.1. Introduction

This chapter provides an exact analysis and active vibration suppression of laminated composite cylindrical shells with embedded circumferentially-poled piezoelectric shear actuators. Results for the static deflection of a four-layer composite are presented first. The solution provides a method of system identification, which includes determination of natural frequencies, mode shapes and through-the-thickness plots of displacements, potential and stresses. Next, a forced vibration analysis is undertaken for the purpose of utilizing a vibration suppression algorithm. The control law utilized is positive position feedback (PPF). A thorough investigation into the influence of the parameters for the control scheme is performed.

3.2. Problem Formulation

An orthogonal cylindrical coordinate system is used to describe the infinitesimal deformations of an N-layer piezoelectric/composite shell as pictured in Figure 3.1. The shell is of extent Θ in the θ-direction, H in the r-direction and infinity in the x-direction. As can be seen in Figure 3.1, the variable R quantifies the location of the mid-surface of

the shell. The top and bottom surfaces, as well as the interfaces between lamina are given by $r^{(1)} = R - H/2$, $r^{(2)},\ldots, r^{(n)},\ldots,r^{(N)}$, $r^{(N+1)} = R + H/2$. Also, it is assumed that each lamina is homogeneous. It should be noted that for each n-layer of the composite, there is a local cylindrical coordinate system that originates at the mid-surface of the lamina.

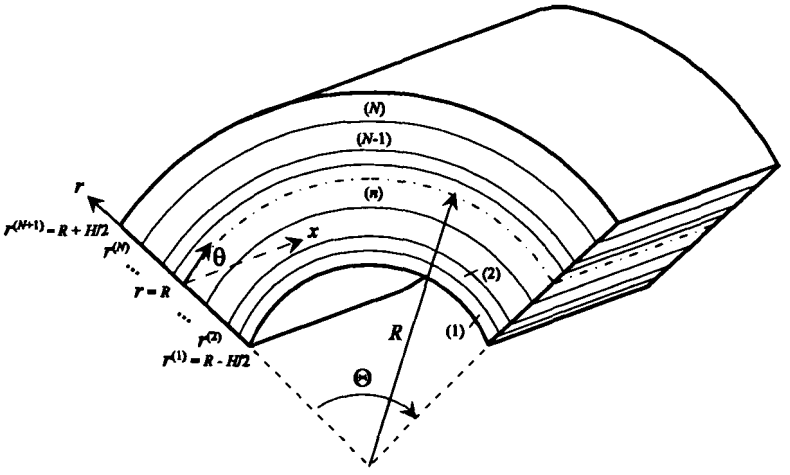

Figure 3.1. The geometrical configuration of the composite piezoelectric shell

We first begin with the equations of motion and the charge equation in the absence of body forces and free charges:

$$
\begin{aligned}
&\sigma_{rr,r}^{(n)} + \frac{1}{r}\sigma_{r\theta,\theta}^{(n)} + \sigma_{xr,x}^{(n)} + \frac{1}{r}\left(\sigma_{rr}^{(n)} - \sigma_{\theta\theta}^{(n)}\right) = \rho^{(n)}\ddot{u}_r^{(n)},\\
&\sigma_{r\theta,r}^{(n)} + \frac{1}{r}\sigma_{\theta\theta,\theta}^{(n)} + \sigma_{x\theta,x}^{(n)} + \frac{2}{r}\sigma_{r\theta}^{(n)} = \rho^{(n)}\ddot{u}_\theta^{(n)},\\
&\sigma_{rx,r}^{(n)} + \frac{1}{r}\sigma_{\theta x,\theta}^{(n)} + \sigma_{xx,x}^{(n)} + \frac{1}{r}\sigma_{rx}^{(n)} = \rho^{(n)}\ddot{u}_x^{(n)},\\
&D_{r,r}^{(n)} + \frac{1}{r}(D_{\theta,\theta}^{(n)} + D_r^{(n)}) + D_{x,x}^{(n)} = 0,
\end{aligned}
\tag{3.1}
$$

where the variables σ are the components of the Cauchy stress tensor in cylindrical coordinates, r is the radial location away from the origin of the shell, ρ is the mass density, u are the cylindrical components of the displacements and the variables D are the components of the electric displacement. A comma followed by the index r indicates

partial differentiation with respect to the position in the r-direction, and a superimposed dot indicates differentiation with respect to time t. The superscript (n) refers to quantities for the n^{th}-layer of the piezoelectric/composite shell.

The fiber-reinforced elastic layers are orthotropic with principal material direction oriented at an angle to the θ-axis in the θ-x surface. It is assumed that the poling direction of the piezoelectric material also lies in the θ-x plane. The constitutive equations, in contracted notation, for lamina n are

$$\begin{Bmatrix} \sigma_{\theta\theta} \\ \sigma_{xx} \\ \sigma_{rr} \\ \sigma_{xr} \\ \sigma_{r\theta} \\ \sigma_{\theta x} \end{Bmatrix}^{(n)} = \begin{bmatrix} C_{11} & C_{12} & C_{13} & 0 & 0 & C_{16} \\ C_{12} & C_{22} & C_{23} & 0 & 0 & C_{26} \\ C_{13} & C_{23} & C_{33} & 0 & 0 & C_{36} \\ 0 & 0 & 0 & C_{44} & C_{45} & 0 \\ 0 & 0 & 0 & C_{45} & C_{55} & 0 \\ C_{16} & C_{26} & C_{36} & 0 & 0 & C_{66} \end{bmatrix}^{(n)} \begin{Bmatrix} \varepsilon_{\theta\theta} \\ \varepsilon_{xx} \\ \varepsilon_{rr} \\ 2\varepsilon_{xr} \\ 2\varepsilon_{r\theta} \\ 2\varepsilon_{\theta x} \end{Bmatrix}^{(n)} - \begin{bmatrix} e_{11} & e_{21} & 0 \\ e_{12} & e_{22} & 0 \\ e_{13} & e_{23} & 0 \\ 0 & 0 & e_{34} \\ 0 & 0 & e_{35} \\ e_{16} & e_{26} & 0 \end{bmatrix}^{(n)} \begin{Bmatrix} E_\theta \\ E_x \\ E_r \end{Bmatrix}^{(n)},$$

$$\begin{Bmatrix} D_\theta \\ D_x \\ D_r \end{Bmatrix}^{(n)} = \begin{bmatrix} e_{11} & e_{12} & e_{13} & 0 & 0 & e_{16} \\ e_{21} & e_{22} & e_{23} & 0 & 0 & e_{26} \\ 0 & 0 & 0 & e_{34} & e_{35} & 0 \end{bmatrix}^{(n)} \begin{Bmatrix} \varepsilon_{\theta\theta} \\ \varepsilon_{xx} \\ \varepsilon_{rr} \\ 2\varepsilon_{xr} \\ 2\varepsilon_{r\theta} \\ 2\varepsilon_{\theta x} \end{Bmatrix}^{(n)} + \begin{bmatrix} \in_{11} & \in_{12} & 0 \\ \in_{12} & \in_{22} & 0 \\ 0 & 0 & \in_{33} \end{bmatrix}^{(n)} \begin{Bmatrix} E_\theta \\ E_x \\ E_r \end{Bmatrix}^{(n)}, \quad (3.2)$$

where the variable ε denotes the infinitesimal strain tensor, E is the electric field vector, C_{ij} are the elasticity constants, e_{ij} are the piezoelectric coefficients and $\in_{ij}$ are the electric permittivities.

The infinitesimal strain tensor and electric field components in cylindrical coordinates are related to displacements u and electric potential ϕ in the follow manner:

$$\varepsilon_{\theta\theta}{}^{(n)} = \frac{1}{r}\left(u_{\theta,\theta}{}^{(n)} + u_r{}^{(n)}\right), \quad \varepsilon_{xx}{}^{(n)} = u_{x,x}{}^{(n)} = 0, \quad \varepsilon_{rr}{}^{(n)} = u_{r,r}{}^{(n)},$$
$$\varepsilon_{r\theta}{}^{(n)} = \frac{1}{2}\left(\frac{1}{r}u_{r,\theta}{}^{(n)} + u_{\theta,r}{}^{(n)} - \frac{u_\theta{}^{(n)}}{r}\right), \quad \varepsilon_{\theta x}{}^{(n)} = \frac{1}{2}\left(u_{\theta,x}{}^{(n)} + \frac{1}{r}u_{x,\theta}{}^{(n)}\right), \tag{3.3}$$
$$\varepsilon_{rx}{}^{(n)} = \frac{1}{2}\left(u_{r,x}{}^{(n)} + u_{x,r}{}^{(n)}\right).$$

$$E_\theta{}^{(n)} = -\frac{1}{r}\phi_{,\theta}{}^{(n)}, \quad E_r{}^{(n)} = -\phi_{,r}{}^{(n)}, \quad E_x{}^{(n)} = -\phi_{,x}{}^{(n)}. \tag{3.4}$$

The shell is assumed to be simply supported and free of electric charge at its edges, resulting in the following boundary conditions:

$$\sigma_{\theta\theta}{}^{(n)} = \sigma_{\theta x}{}^{(n)} = 0, \quad u_r{}^{(n)} = 0, \quad D_\theta{}^{(n)} = 0 \text{ at } \theta = 0, \Theta. \tag{3.5}$$

It should be noted that the above mechanical boundary conditions are for the case when the shell is viewed as a three-dimensional body. They simulate a simply supported plate characterized by the vanishing of transverse displacement and bending moment at the edges.

The mechanical interface conditions for each of the cylindrical laminae are given as follows:

$$\begin{aligned} &u_r{}^{(n)} = u_r{}^{(n+1)}, \quad u_\theta{}^{(n)} = u_\theta{}^{(n+1)}, \quad u_x{}^{(n)} = u_x{}^{(n+1)}, \\ &\sigma_{r\theta}{}^{(n)} = \sigma_{r\theta}{}^{(n+1)}, \quad \sigma_{rx}{}^{(n)} = \sigma_{rx}{}^{(n+1)}, \quad \sigma_{rr}{}^{(n)} = \sigma_{rr}{}^{(n+1)} \end{aligned} \text{ at } r^{(n)} = r^{(n+1)}. \tag{3.6}$$

The three components of the displacements in (3.6) are continuous from one layer to the next due to the assumption that all the laminae are perfectly bonded together. The components of stress listed in (3.6) are continuous between layers since a small element that overlaps the interface must be in equilibrium. This dictates that the traction vector between the layers must be continuous.

The interface between the lamina can either be electroded or not electroded. If the interface is not electroded, then the electric interface condition becomes the following:

$$\phi^{(n)} = \phi^{(n+1)} \quad \text{and} \quad D_r^{(n)} = D_r^{(n+1)} \quad \text{at } r = r^{(n+1)}. \tag{3.7}$$

If the interface is electroded, then the electrical interface condition must be as follows:

$$\phi^{(n)} = \phi^{(n+1)} = f(\theta, t) \text{ at } r = r^{(n+1)}. \tag{3.8}$$

Where the function $f(\theta,t)$ describes the potential distribution as a function of both position θ and time t.

The boundary conditions on the top and bottom surfaces are specified in the following manner:

$$\sigma_{r\theta} = \sigma_{rx} = 0\,,\ \sigma_{rr} = p(\theta,t) \text{ at } r = r^{(1)} \text{ and } r^{(N+1)},$$

$$\text{and} \tag{3.9}$$

$$D_r = q(\theta,t) \text{ or } \phi = \phi_0(\theta,t) \text{ at } r = r^{(1)} \text{ and } r^{(N+1)}.$$

The stress components $\sigma_{r\theta}$ and σ_{rx} in (3.9) are set equal to zero because it is assumed that the there are no applied shear stresses to the shell. The transverse normal stress σ_{rr} is assumed to have a functional variation on the top and bottom surfaces to accommodate a forced vibration analysis. The electrical boundary conditions in (3.9) are also assumed to have functional variations, and in this case either the radial electric displacement or potential is specified.

3.3. Exact Solution

We seek an exact solution to the cylindrical bending vibration of a composite piezoelectric shell. The displacements, stresses, electric displacements and electric potentials are assumed to be functions of θ and r only. This assumption is valid because the loads (mechanical and electrical), as well as the material properties are not a function of the x-coordinate. Also, the geometry of the shell is of infinite extent in the x-direction.

We assume the following semi-inverse solution for the displacements and electric potential:

$$\begin{aligned} u_\theta^{(n)}(\theta,r,t) &= U_\theta^{(n)}(r)e^{i\omega t}\cos(p\theta), \\ u_x^{(n)}(\theta,r,t) &= U_x^{(n)}(r)e^{i\omega t}\cos(p\theta), \\ u_r^{(n)}(\theta,r,t) &= U_r^{(n)}(r)e^{i\omega t}\sin(p\theta), \\ \phi^{(n)}(\theta,r,t) &= \Phi^{(n)}(r)e^{i\omega t}\cos(p\theta), \end{aligned} \tag{3.10}$$

where $p = \dfrac{k\pi}{\Theta}$ and k is an integer that defines the circumferential mode shape.

As can be seen from (3.10), the assumed form of the radial displacement u_r is equal to 0 at $\theta = 0, \Theta$, which is required by the boundary conditions in (3.5). The assumed forms of displacement and electric potential in (3.10) are substituted into (3.3) and (3.4) to obtain the components of the infinitesimal strain tensor and electric field vector:

$$\varepsilon_{\theta\theta}^{(n)} = \frac{1}{r}\left[-pU_\theta^{(n)} + U_r^{(n)}\right]e^{i\omega t}\sin(p\theta), \quad \varepsilon_{xx}^{(n)} = 0,$$

$$\varepsilon_{rr}^{(n)} = U_r^{(n)'} e^{i\omega t}\sin(p\theta), \quad \varepsilon_{r\theta}^{(n)} = \frac{1}{2}\left[\frac{U_r^{(n)} p - U_\theta^{(n)}}{r} + U_\theta^{(n)'}\right]e^{i\omega t}\cos(p\theta), \tag{3.11}$$

$$\varepsilon_{\theta x}^{(n)} = -\frac{1}{2r} pU_x^{(n)} e^{i\omega t}\sin(p\theta), \quad \varepsilon_{rx}^{(n)} = \frac{1}{2}U_x^{(n)'} e^{iwt}\cos(p\theta),$$

$$E_\theta^{(n)} = \frac{1}{r}\Phi^{(n)} p e^{i\omega t}\sin(p\theta), \quad E_r^{(n)} = -\Phi^{(n)} e^{i\omega t}\cos(p\theta), \quad E_x^{(n)} = 0, \tag{3.12}$$

where the prime denotes differentiation with respect to r.

The stresses and electric displacements are found using the derived expressions in (3.11) and (3.12) along with the constitutive relations found in (3.2). This results in the following Cauchy stress and electric displacement components:

$$\sigma_{\theta\theta}^{(n)} = \left(C_{11}^{(n)}\frac{U_r^{(n)} - pU_\theta^{(n)}}{r} + C_{13}^{(n)} U_r^{(n)'} - C_{16}^{(n)}\frac{pU_x^{(n)}}{r} - e_{11}^{(n)}\frac{\Phi^{(n)} p}{r}\right)e^{i\omega t}\sin(p\theta),$$

$$\sigma_{xx}^{(n)} = \left(C_{12}^{(n)}\frac{U_r^{(n)} - pU_\theta^{(n)}}{r} + C_{23}^{(n)} U_r^{(n)'} - C_{26}^{(n)}\frac{pU_x^{(n)}}{r} - e_{12}^{(n)}\frac{\Phi^{(n)} p}{r}\right)e^{i\omega t}\sin(p\theta),$$

$$\sigma_{rr}^{(n)} = \left(C_{13}^{(n)}\frac{U_r^{(n)} - pU_\theta^{(n)}}{r} + C_{33}^{(n)} U_r^{(n)'} - C_{36}^{(n)}\frac{pU_x^{(n)}}{r} - e_{13}^{(n)}\frac{\Phi^{(n)} p}{r}\right)e^{i\omega t}\sin(p\theta), \tag{3.13}$$

$$\sigma_{xr}^{(n)} = \left(C_{44}^{(n)} U_x^{(n)'} + C_{45}^{(n)}\frac{U_r^{(n)} p - U_\theta^{(n)}}{r} + C_{45}^{(n)} U_\theta^{(n)'} + e_{34}^{(n)}\Phi^{(n)'}\right)e^{i\omega t}\cos(p\theta),$$

$$\sigma_{r\theta}^{(n)} = \left(C_{45}^{(n)} U_x^{(n)'} + C_{55}^{(n)}\frac{U_r^{(n)} p - U_\theta^{(n)}}{r} + C_{55}^{(n)} U_\theta^{(n)'} + e_{35}^{(n)}\Phi^{(n)'}\right)e^{i\omega t}\cos(p\theta),$$

$$\sigma_{\theta x}^{(n)} = \left(C_{16}^{(n)}\frac{U_r^{(n)} - pU_\theta^{(n)}}{r} + C_{36}^{(n)} U_r^{(n)'} - C_{66}^{(n)}\frac{pU_x^{(n)}}{r} - e_{16}^{(n)}\frac{\Phi^{(n)} p}{r}\right)e^{i\omega t}\sin(p\theta).$$

$$D_\theta^{(n)} = \left(e_{11}^{(n)}\frac{U_r^{(n)} - pU_\theta^{(n)}}{r} + e_{13}^{(n)} U_r^{(n)'} - e_{16}^{(n)}\frac{pU_x^{(n)}}{r} + \epsilon_{11}^{(n)}\frac{\Phi^{(n)} p}{r}\right)e^{i\omega t}\sin(p\theta),$$

$$D_x^{(n)} = \left(e_{21}^{(n)}\frac{U_r^{(n)} - pU_\theta^{(n)}}{r} + e_{23}^{(n)} U_r^{(n)'} - e_{26}^{(n)}\frac{pU_x^{(n)}}{r} + \epsilon_{21}^{(n)}\frac{\Phi^{(n)} p}{r}\right)e^{i\omega t}\sin(p\theta), \tag{3.14}$$

$$D_r^{(n)} = \left(e_{34}^{(n)} U_x^{(n)'} + e_{35}^{(n)}\frac{U_r^{(n)} p - U_\theta^{(n)}}{r} + e_{35}^{(n)} U_\theta^{(n)'} - \epsilon_{33}^{(n)}\Phi^{(n)'}\right)e^{i\omega t}\cos(p\theta).$$

Upon examination of $\sigma_{\theta\theta}{}^{(n)}$ and $\sigma_{\theta x}{}^{(n)}$ in (3.13) and $D_\theta{}^{(n)}$ in (3.14), it is seen that these expressions satisfy exactly the relevant boundary conditions from (3.5). This implies that all of the boundary conditions at the simply supported edges are identically satisfied by the assumed form of displacements and potential in (3.10).

The equations of motion and charge equation of electrostatics can be expressed in terms of the assumed displacements and electric potential using (3.13) and (3.14):

$$\begin{aligned} &C_{13}{}^{(n)} r U_r{}^{(n)\prime} - (C_{13}{}^{(n)} + C_{55}{}^{(n)}) p r U_\theta{}^{(n)\prime} + C_{33}{}^{(n)} r^2 U_r{}^{(n)\prime\prime} - (C_{36}{}^{(n)} + C_{45}{}^{(n)}) p r U_x{}^{(n)\prime} \\ &- (e_{13}{}^{(n)} + e_{35}{}^{(n)}) p r \Phi^{(n)\prime} - C_{55}{}^{(n)} p (p U_r{}^{(n)} - U_\theta{}^{(n)}) + (C_{33}{}^{(n)} - C_{13}{}^{(n)}) r U_r{}^{(n)\prime} \\ &- C_{11}{}^{(n)} (U_r{}^{(n)} - p U_\theta{}^{(n)}) + C_{16}{}^{(n)} p U_x{}^{(n)} + e_{11}{}^{(n)} p \Phi^{(n)} + \rho^{(n)} \omega^2 r^2 U_r{}^{(n)} = 0, \end{aligned} \tag{3.15}$$

$$\begin{aligned} &C_{45}{}^{(n)} r^2 U_x{}^{(n)\prime\prime} + (C_{13}{}^{(n)} + C_{55}{}^{(n)}) p r U_r{}^{(n)\prime} + C_{55}{}^{(n)} r^2 U_\theta{}^{(n)\prime\prime} + e_{35}{}^{(n)} r^2 \Phi^{(n)\prime\prime} \\ &+ C_{11}{}^{(n)} p (U_r{}^{(n)} - p U_\theta{}^{(n)}) - C_{16}{}^{(n)} p^2 U_x{}^{(n)} - e_{11}{}^{(n)} p^2 \Phi^{(n)} + 2 C_{45}{}^{(n)} r U_x{}^{(n)\prime} \\ &+ C_{55}{}^{(n)} (p U_r{}^{(n)} - U_\theta{}^{(n)}) + C_{55}{}^{(n)} r U_\theta{}^{(n)\prime} + 2 e_{35}{}^{(n)} r \Phi^{(n)\prime} + r^2 \rho^{(n)} \omega^2 U_\theta{}^{(n)} = 0, \end{aligned} \tag{3.16}$$

$$\begin{aligned} &C_{44}{}^{(n)} r^2 U_x{}^{(n)\prime\prime} + (C_{45}{}^{(n)} + C_{36}{}^{(n)}) p r U_r{}^{(n)\prime} + C_{45}{}^{(n)} r^2 U_\theta{}^{(n)\prime\prime} + e_{34}{}^{(n)} r^2 \Phi^{(n)\prime\prime} \\ &+ C_{16}{}^{(n)} p (U_r{}^{(n)} - p U_\theta{}^{(n)}) - C_{66}{}^{(n)} p^2 U_x{}^{(n)} - e_{16}{}^{(n)} p^2 \Phi^{(n)} + C_{44}{}^{(n)} r U_x{}^{(n)\prime} \\ &+ e_{35}{}^{(n)} r \Phi^{(n)\prime} + \rho^{(n)} \omega^2 r^2 U_x{}^{(n)} = 0, \end{aligned} \tag{3.17}$$

$$\begin{aligned} &e_{34}{}^{(n)} r^2 U_x{}^{(n)\prime\prime} + (e_{13}{}^{(n)} + e_{35}{}^{(n)}) p r U_r{}^{(n)\prime} + e_{35}{}^{(n)} r^2 U_\theta{}^{(n)\prime\prime} - \in_{33}{}^{(n)} r^2 \Phi^{(n)\prime\prime} \\ &+ e_{11}{}^{(n)} p (U_r{}^{(n)} - p U_\vartheta{}^{(n)}) - e_{16}{}^{(n)} p^2 U_x{}^{(n)} + \in_{11}{}^{(n)} p^2 \Phi^{(n)} \\ &+ e_{34}{}^{(n)} r U_x{}^{(n)\prime} - \in_{33}{}^{(n)} r \Phi^{(n)\prime} = 0. \end{aligned} \tag{3.18}$$

Note that the non-zero common factor of $e^{i\omega t}$ present in (3.15)-(3.18) cancels from each equation.

Equations (3.15)-(3.18) are a system of coupled ordinary second order differential equations with non-constant coefficients. A method for solving a system such as this is

to use a Frobenius method for ${U_\theta}^{(n)}$, ${U_x}^{(n)}$, ${U_r}^{(n)}$, and $\Phi^{(n)}$in the following manner (Kreyszig, 1999):

$$
\begin{aligned}
{U_\theta}^{(n)}(r) &= r^{\lambda^{(n)}} \sum_{\beta=0}^{\infty} {A_\theta}^{(n,\beta)} r^{\beta}, \quad {U_x}^{(n)}(r) = r^{\lambda^{(n)}} \sum_{\beta=0}^{\infty} {A_x}^{(n,\beta)} r^{\beta}, \\
{U_r}^{(n)}(r) &= r^{\lambda^{(n)}} \sum_{\beta=0}^{\infty} {A_r}^{(n,\beta)} r^{\beta}, \quad \Phi(r)^{(n)} = r^{\lambda^{(n)}} \sum_{\beta=0}^{\infty} {A_\phi}^{(n,\beta)} r^{\beta},
\end{aligned}
\tag{3.19}
$$

where ${A_\theta}^{(n,\beta)}$, ${A_x}^{(n,\beta)}$, ${A_r}^{(n,\beta)}$ and ${A_\phi}^{(n,\beta)}$ are coefficients in the series solutions, and $\lambda^{(n)}$ are constants that need to be determined. The values of $\lambda^{(n)}$ can be either real or complex and it is chosen such that either ${A_\theta}^{(n,0)}$, ${A_x}^{(n,0)}$, ${A_r}^{(n,0)}$ or ${A_\phi}^{(n,\beta)}$ is non-zero. Note that the preceding condition is no restriction on generality since it simply means that we factor out the highest possible power of r.

The equations in (3.19) are first substituted into (3.5) yielding the following equation:

$$
\begin{aligned}
&{C_{13}}^{(n)} \sum_{\beta=0}^{\infty} {A_r}^{(n,\beta)} \left(\beta + \lambda^{(n)}\right) r^{\beta+\lambda^{(n)}} - \left({C_{13}}^{(n)} + {C_{55}}^{(n)}\right) p \sum_{\beta=0}^{\infty} {A_\theta}^{(n,\beta)} \left(\beta + \lambda^{(n)}\right) r^{\beta+\lambda^{(n)}} \\
&+ {C_{33}}^{(n)} \sum_{\beta=0}^{\infty} {A_r}^{(n,\beta)} \left(\beta + \lambda^{(n)}\right)\left(\beta + \lambda^{(n)} - 1\right) r^{\beta+\lambda^{(n)}} - \left({C_{36}}^{(n)} + {C_{45}}^{(n)}\right) p \sum_{\beta=0}^{\infty} {A_x}^{(n,\beta)} \left(\beta + \lambda^{(n)}\right) r^{\beta+\lambda^{(n)}} \\
&- \left({e_{13}}^{(n)} + {e_{35}}^{(n)}\right) p \sum_{\beta=0}^{\infty} {A_\phi}^{(n,\beta)} \left(\beta + \lambda^{(n)}\right) r^{\beta+\lambda^{(n)}} - {C_{55}}^{(n)} p^2 \sum_{\beta=0}^{\infty} {A_r}^{(n,\beta)} r^{\beta+\lambda^{(n)}} \\
&+ {C_{55}}^{(n)} p \sum_{\beta=0}^{\infty} {A_\theta}^{(n,\beta)} r^{\beta+\lambda^{(n)}} + \left({C_{33}}^{(n)} - {C_{13}}^{(n)}\right) \sum_{\beta=0}^{\infty} {A_r}^{(n,\beta)} \left(\beta + \lambda^{(n)}\right) r^{\beta+\lambda^{(n)}} \\
&- {C_{11}}^{(n)} \sum_{\beta=0}^{\infty} {A_r}^{(n,\beta)} r^{\beta+\lambda^{(n)}} + {C_{11}}^{(n)} p \sum_{\beta=0}^{\infty} {A_\theta}^{(n,\beta)} r^{\beta+\lambda^{(n)}} + {C_{16}}^{(n)} p \sum_{\beta=0}^{\infty} {A_x}^{(n,\beta)} r^{\beta+\lambda^{(n)}} \\
&+ {e_{11}}^{(n)} p \sum_{\beta=0}^{\infty} {A_\phi}^{(n,\beta)} r^{\beta+\lambda^{(n)}} + \rho^{(n)} \omega^2 \sum_{\beta=2}^{\infty} {A_r}^{(n,\beta-2)} r^{\beta+\lambda^{(n)}} = 0.
\end{aligned}
\tag{3.20}
$$

Next, (3.19) is substituted into (3.16) yielding the following equation:

$$
\begin{aligned}
&C_{45}^{(n)}\sum_{\beta=0}^{\infty}A_x^{(n,\beta)}\left(\beta+\lambda^{(n)}\right)\left(\beta+\lambda^{(n)}-1\right)r^{\beta+\lambda^{(n)}}+\left(C_{13}^{(n)}+C_{55}^{(n)}\right)p\sum_{\beta=0}^{\infty}A_r^{(n,\beta)}\left(\beta+\lambda^{(n)}\right)r^{\beta+\lambda^{(n)}}\\
&+C_{55}^{(n)}\sum_{\beta=0}^{\infty}A_\theta^{(n,\beta)}\left(\beta+\lambda^{(n)}\right)\left(\beta+\lambda^{(n)}-1\right)r^{\beta+\lambda^{(n)}}+e_{35}^{(n)}\sum_{\beta=0}^{\infty}A_\phi^{(n,\beta)}\left(\beta+\lambda^{(n)}\right)\left(\beta+\lambda^{(n)}-1\right)r^{\beta+\lambda^{(n)}}\\
&+C_{11}^{(n)}p\sum_{\beta=0}^{\infty}\left(A_r^{(n,\beta)}-pA_\theta^{(n,\beta)}\right)r^{\beta+\lambda^{(n)}}-C_{16}^{(n)}p^2\sum_{\beta=0}^{\infty}A_x^{(n,\beta)}r^{\beta+\lambda^{(n)}}-e_{11}^{(n)}p^2\sum_{\beta=0}^{\infty}A_\phi^{(n,\beta)}r^{\beta+\lambda^{(n)}}\\
&+2C_{45}^{(n)}\sum_{\beta=0}^{\infty}A_x^{(n,\beta)}\left(\beta+\lambda^{(n)}\right)r^{\beta+\lambda^{(n)}}+C_{55}^{(n)}\sum_{\beta=0}^{\infty}\left(pA_r^{(n,\beta)}-A_\theta^{(n,\beta)}\right)r^{\beta+\lambda^{(n)}}\\
&+C_{55}^{(n)}\sum_{\beta=0}^{\infty}A_\theta^{(n,\beta)}\left(\beta+\lambda^{(n)}\right)r^{\beta+\lambda^{(n)}}+2e_{35}^{(n)}\sum_{\beta=0}^{\infty}A_\phi^{(n,\beta)}\left(\beta+\lambda^{(n)}\right)r^{\beta+\lambda^{(n)}}\\
&+\rho^{(n)}\omega^2\sum_{\beta=2}^{\infty}A_\theta^{(n,\beta-2)}r^{\beta+\lambda^{(n)}}=0.
\end{aligned}
\tag{3.21}
$$

Substitution of (3.19) into (3.17) yields the following equation:

$$
\begin{aligned}
&C_{44}^{(n)}\sum_{\beta=0}^{\infty}A_x^{(n,\beta)}\left(\beta+\lambda^{(n)}\right)\left(\beta+\lambda^{(n)}-1\right)r^{\beta+\lambda^{(n)}}+\left(C_{45}^{(n)}+C_{36}^{(n)}\right)p\sum_{\beta=0}^{\infty}A_r^{(n,\beta)}\left(\beta+\lambda^{(n)}\right)r^{\beta+\lambda^{(n)}}\\
&+C_{45}^{(n)}\sum_{\beta=0}^{\infty}A_\theta^{(n,\beta)}\left(\beta+\lambda^{(n)}\right)\left(\beta+\lambda^{(n)}-1\right)r^{\beta+\lambda^{(n)}}+e_{34}^{(n)}\sum_{\beta=0}^{\infty}A_\phi^{(n,\beta)}\left(\beta+\lambda^{(n)}\right)\left(\beta+\lambda^{(n)}-1\right)r^{\beta+\lambda^{(n)}}\\
&+C_{16}^{(n)}p\sum_{\beta=0}^{\infty}\left(A_r^{(n,\beta)}-pA_\theta^{(n,\beta)}\right)r^{\beta+\lambda^{(n)}}-C_{66}^{(n)}p^2\sum_{\beta=0}^{\infty}A_x^{(n,\beta)}r^{\beta+\lambda^{(n)}}\\
&-e_{16}^{(n)}p^2\sum_{\beta=0}^{\infty}A_\phi^{(n,\beta)}r^{\beta+\lambda^{(n)}}+C_{44}^{(n)}\sum_{\beta=0}^{\infty}A_x^{(n,\beta)}\left(\beta+\lambda^{(n)}\right)r^{\beta+\lambda^{(n)}}+e_{35}^{(n)}\sum_{\beta=0}^{\infty}A_\phi^{(n,\beta)}\left(\beta+\lambda^{(n)}\right)r^{\beta+\lambda^{(n)}}\\
&+\rho^{(n)}\omega^2\sum_{\beta=2}^{\infty}A_x^{(n,\beta-2)}r^{\beta+\lambda^{(n)}}=0.
\end{aligned}
\tag{3.22}
$$

Finally, (3.19) is substituted into (3.18) yielding the following equation:

$$
\begin{aligned}
&e_{34}^{(n)}\sum_{\beta=0}^{\infty}A_x^{(n,\beta)}\left(\beta+\lambda^{(n)}\right)\left(\beta+\lambda^{(n)}-1\right)r^{\beta+\lambda^{(n)}}+\left(e_{13}^{(n)}+e_{35}^{(n)}\right)p\sum_{\beta=0}^{\infty}A_r^{(n,\beta)}\left(\beta+\lambda^{(n)}\right)r^{\beta+\lambda^{(n)}}\\
&+e_{35}^{(n)}\sum_{\beta=0}^{\infty}A_\theta^{(n,\beta)}\left(\beta+\lambda^{(n)}\right)\left(\beta+\lambda^{(n)}-1\right)r^{\beta+\lambda^{(n)}}+e_{11}^{(n)}p\sum_{\beta=0}^{\infty}\left(A_r^{(n,\beta)}-pA_\theta^{(n,\beta)}\right)r^{\beta+\lambda^{(n)}}\\
&-e_{16}^{(n)}p^2\sum_{\beta=0}^{\infty}A_x^{(n,\beta)}r^{\beta+\lambda^{(n)}}+\in_{11}^{(n)}p^2\sum_{\beta=0}^{\infty}A_\phi^{(n,\beta)}r^{\beta+\lambda^{(n)}}+e_{34}^{(n)}\sum_{\beta=0}^{\infty}A_x^{(n,\beta)}\left(\beta+\lambda^{(n)}\right)r^{\beta+\lambda^{(n)}}\\
&-\in_{33}^{(n)}\sum_{\beta=0}^{\infty}A_\phi^{(n,\beta)}\left(\beta+\lambda^{(n)}\right)r^{\beta+\lambda^{(n)}}=0.
\end{aligned}
\tag{3.23}
$$

Equating the $r^{\lambda^{(n)}}$ terms on both sides of Equations (3.20), (3.21), (3.22) and (3.23) results in the following system of equations:

$$\left[M^{(n)}(0)\right]\begin{Bmatrix} A_r^{(n,0)} \\ A_\theta^{(n,0)} \\ A_x^{(n,0)} \\ A_\phi^{(n,0)} \end{Bmatrix} = \begin{Bmatrix} 0 \\ 0 \\ 0 \\ 0 \end{Bmatrix}, \tag{3.24}$$

where the coefficient matrix $\left[M^{(n)}(\beta)\right]$ has the following form:

$$\left[M^{(n)}(\beta)\right]=\begin{bmatrix} -C_{11}^{(n)} - C_{55}^{(n)} p^2 + C_{33}^{(n)}\left(\beta+\lambda^{(n)}\right)^2 & C_{11}^{(n)} p + C_{55}^{(n)} p - \left(C_{13}^{(n)} + C_{55}^{(n)}\right) p\left(\beta+\lambda^{(n)}\right) \\ C_{11}^{(n)} p + C_{13}^{(n)} p\left(\beta+\lambda^{(n)}\right) + C_{55}^{(n)} p\left(\beta+\lambda^{(n)}+1\right) & -C_{11}^{(n)} p^2 + C_{55}^{(n)}\left(\beta+\lambda^{(n)}+1\right)\left(\beta+\lambda^{(n)}-1\right) \\ C_{16}^{(n)} p + \left(C_{36}^{(n)} + C_{45}^{(n)}\right) p\left(\beta+\lambda^{(n)}\right) & -C_{16}^{(n)} p^2 + C_{45}^{(n)}\left(\beta+\lambda^{(n)}\right)\left(\beta+\lambda^{(n)}-1\right) \\ e_{11}^{(n)} p + \left(e_{13}^{(n)} + e_{35}^{(n)}\right) p\left(\beta+\lambda^{(n)}\right) & -e_{11}^{(n)} p^2 + e_{35}^{(n)}\left(\beta+\lambda^{(n)}\right)\left(\beta+\lambda^{(n)}-1\right) \end{bmatrix} \cdots$$

$$\begin{bmatrix} C_{16}^{(n)} p - \left(C_{36}^{(n)} + C_{45}^{(n)}\right) p\left(\beta+\lambda^{(n)}\right) & e_{11}^{(n)} p - \left(e_{13}^{(n)} + e_{35}^{(n)}\right) p\left(\beta+\lambda^{(n)}\right) \\ -C_{16}^{(n)} p^2 + C_{45}^{(n)}\left(\beta+\lambda^{(n)}+1\right)\left(\beta+\lambda^{(n)}\right) & -e_{11}^{(n)} p^2 + e_{35}^{(n)}\left(\beta+\lambda^{(n)}+1\right)\left(\beta+\lambda^{(n)}\right) \\ -C_{66}^{(n)} p^2 + C_{44}^{(n)}\left(\beta+\lambda^{(n)}\right)^2 & -e_{16}^{(n)} p^2 + e_{35}^{(n)}\left(\beta+\lambda^{(n)}\right) + e_{34}^{(n)}\left(\beta+\lambda^{(n)}\right)\left(\beta+\lambda^{(n)}-1\right) \\ -e_{16}^{(n)} p^2 + e_{34}^{(n)}\left(\beta+\lambda^{(n)}\right)^2 & \epsilon_{11}^{(n)} p^2 - \epsilon_{33}^{(n)}\left(\beta+\lambda^{(n)}\right)^2 \end{bmatrix}. \tag{3.25}$$

A non-trivial solution for $\left\{A_r^{(n,0)}, A_\theta^{(n,0)}, A_x^{(n,0)}, A_\phi^{(n,0)}\right\}$ in (3.24) is obtained by setting the determinant of the coefficient matrix equal to zero

$$\left|M^{(n)}(0)\right| = 0. \tag{3.26}$$

Equation (3.26) is the *indicial equation* for the differential equations in (3.15)-(3.18). The determinant of (3.26) is an eighth order polynomial in $\lambda^{(n)}$. The eight roots of this polynomial correspond to eight separate solutions. The linear nature of the problem allows for the sum of these solutions to form a single solution. Corresponding to each $\lambda_m^{(n)}$ (m = 1,...,8) an eigenvector can be found to determine the relative magnitudes of $A_r^{(n,0)}$, $A_\theta^{(n,0)}$, $A_x^{(n,0)}$ and $A_\phi^{(n,0)}$. This means that for each $\lambda_m^{(n)}$, there is a single unknown that must be determined. Since there are eight values of $\lambda_m^{(n)}$, there are eight unknowns per layer that must be determined. It is assumed that the values $\lambda_m^{(n)}$ are distinct and do not differ by an integer value. In the event of a mathematically

degenerate case of repeated values of $\lambda_m^{(n)}$, or values of $\lambda_m^{(n)}$ that differ by an integer, the solution in (3.19) must be modified appropriately (Kreyszig, 1999).

Next, the $r^{\lambda^{(n)}+1}$ terms from (3.20), (3.21), (3.22) and (3.23) are equated resulting in the following matrix equation for the series coefficients $A_r^{(n,1)}$, $A_\theta^{(n,1)}$, $A_x^{(n,1)}$ and $A_\phi^{(n,1)}$:

$$\begin{Bmatrix} A_r^{(n,1)} \\ A_\theta^{(n,1)} \\ A_x^{(n,1)} \\ A_\phi^{(n,1)} \end{Bmatrix} = \left[M^{(n)}(1)\right]^{-1} \begin{Bmatrix} 0 \\ 0 \\ 0 \\ 0 \end{Bmatrix} = \begin{Bmatrix} 0 \\ 0 \\ 0 \\ 0 \end{Bmatrix}. \tag{3.27}$$

Note that $\left[M^{(n)}(1)\right]$ in (3.27) is invertible when $\lambda_m^{(n)}$ attains values that are distinct and do not differ by an integer value.

Finally, the $r^{\lambda^{(n)}+\beta}$ $(\beta \geq 2)$ terms from (3.20), (3.21), (3.22) and (3.23) are equated resulting in the following recurrence matrix equation for the series coefficients $A_r^{(n,\beta)}$, $A_\theta^{(n,\beta)}$, $A_x^{(n,\beta)}$ and $A_\phi^{(n,\beta)}$:

$$\begin{Bmatrix} A_r^{(n,\beta)} \\ A_\theta^{(n,\beta)} \\ A_x^{(n,\beta)} \\ A_\phi^{(n,\beta)} \end{Bmatrix} = \left[M^{(n)}(\beta)\right]^{-1} \begin{Bmatrix} -\rho^{(n)}\omega^2 A_r^{(\beta-2)} \\ -\rho^{(n)}\omega^2 A_\theta^{(\beta-2)} \\ -\rho^{(n)}\omega^2 A_x^{(\beta-2)} \\ 0 \end{Bmatrix}. \tag{3.28}$$

The recurrence relation (3.28) is evaluated successively for $\beta = 2,3,\ldots,$ to obtain the series coefficients $A_r^{(n,\beta)}$, $A_\theta^{(n,\beta)}$, $A_x^{(n,\beta)}$ and $A_\phi^{(n,\beta)}$. The complete solution, obtained by a superposition of the solutions corresponding to the eight exponents $\lambda_m^{(n)}$, is

$$U_\theta^{(n)}(r)=\sum_{m=1}^{8}\left(B_m^{(n)}\sum_{\beta=0}^{\infty}A_\theta^{(n,\beta)}\,r^{\beta+\lambda_m^{(n)}}\right),\quad U_x^{(n)}(r)=\sum_{m=1}^{8}\left(B_m^{(n)}\sum_{\beta=0}^{\infty}A_x^{(n,\beta)}\,r^{\beta+\lambda_m^{(n)}}\right),$$
$$U_r^{(n)}(r)=\sum_{m=1}^{8}\left(B_m^{(n)}\sum_{\beta=0}^{\infty}A_r^{(n,\beta)}\,r^{\beta+\lambda_m^{(n)}}\right),\quad \Phi^{(n)}(r)=\sum_{m=1}^{8}\left(B_m^{(n)}\sum_{\beta=0}^{\infty}A_\phi^{(n,\beta)}\,r^{\beta+\lambda_m^{(n)}}\right), \tag{3.29}$$

where $B_m^{(n)}$ are unknown constants.

3.3.1. Static Deformation and Forced Vibration Analysis

If the hybrid laminate is subjected to a static or time harmonic load, the angular frequency ω and k are known. The unknown coefficients $B_m^{(n)}$ are obtained by applying four boundary conditions on the outer surface (3.9), four conditions on the inner surface and eight interface conditions (3.6) and (3.7) or (3.8) at each of the (N-1) interfaces between the N laminae, which leads to the following matrix equation:

$$[G(\omega)]\{B\}=\{W\}, \tag{3.30}$$

where $[G(\omega)]$ is a known $8N\times 8N$ matrix, $\{W\}$ is a known vector of length $8N$ and $\{B\}$ is a vector consisting of the $8N$ unknown coefficients $B_m^{(n)}$. The linear systems of equations (3.30) are solved to obtain the $8N$ constants $B_m^{(n)}$ and subsequently the solution for every layer. In the case of static deformation, the angular frequency $\omega = 0$.

3.3.2. Determination of Natural Frequencies and Mode Shapes

The hybrid composite shell is in a state of free vibration if it is not subjected to any applied mechanical or electric loads. For fixed k (i.e. fixed p), the series coefficients $A_r^{(n,\beta)}$, $A_\theta^{(n,\beta)}$, $A_x^{(n,\beta)}$ and $A_\phi^{(n,\beta)}$ are obtained in terms of ω using the recurrence relations (3.28). Applying boundary conditions on the outer surfaces, interfaces between

the laminae and the inner surfaces of the laminate results in the following homogeneous matrix equation:

$$[G(\omega)]\{B\} = \{0\}, \tag{3.31}$$

where $[G(\omega)]$ is a $8N \times 8N$ matrix whose elements are polynomials of ω and $\{B\}$ is a vector consisting of the $8N$ unknown constants $B_m^{(n)}$. A non-trivial solution for the constants $B_m^{(n)}$ is obtained by setting the determinant $|G(\omega)|$ equal to zero. The resulting polynomial equation is solved to obtain a set of eigenvalues that are arranged in ascending order as $\{\omega_k^{(1)}, \omega_k^{(2)}, \omega_k^{(3)}, \ldots\}$, which are the natural frequencies of the shell corresponding to the circumferential mode shape defined by the integer k. The eigenvector $\{B\}$ associated with the eigenvalue $\omega_k^{(j)}$ is determined from the nullspace of $[G(\omega)]$. The displacements, electric potential, stresses and electric displacement at any point within the laminate are determined using the $8N$ constants $B_m^{(n)}$ from eigenvector $\{B\}$.

3.3.3. Implementation of Positive Position Feedback

Active damping is implemented through feedback control. The outer surface of the hybrid composite shell is subjected to a harmonic distributed load of the following form:

$$\sigma_{rr}^{(N)}(\theta, R + H/2, t) = q_0 e^{i\omega t} \sin(\pi\theta/\Theta), \tag{3.32}$$

where the circular frequency ω is prescribed. We use the PPF controller to achieve the active damping. The PPF controller introduces a second order compensator which is forced by the electric potential of the sensor,

$$\ddot{\eta} + 2\zeta_c \omega_c \dot{\eta} + \omega_c{}^2 \eta = \omega_c{}^2 \phi(0, r_s, t), \tag{3.33}$$

where r_s is the radial location where the sensor potential is measured, η is the compensator coordinate, ω_c is the frequency of the compensator and ζ_c is the damping ratio of the compensator.

For steady-state vibration $\eta = \eta_0 e^{i\omega t}$ and $\phi = \phi_0 e^{i\omega t}$; therefore, (3.33) becomes:

$$-\omega^2 \eta_0 + 2i\omega_c \omega \eta_0 + \omega_c{}^2 \eta_0 = \omega_c{}^2 \Phi^{(n_s)}(r_s), \tag{3.34}$$

where the sensor is lamina n_s. Solving for η_0:

$$\eta_0 = \left[\frac{\omega_c{}^2}{\left(\omega_c{}^2 - \omega^2\right) + 2i\zeta_c \omega_c \omega} \right] \Phi^{(n_s)}(r_s). \tag{3.35}$$

The controller coordinate η, magnified by a positive gain, is then fed back as a voltage input ϕ to a piezoelectric shear actuator

$$\begin{aligned} \phi(\theta, t) &= g\omega_c{}^2 \eta_0 e^{i\omega t} \cos(\pi\theta/\Theta), \\ &= \left[\frac{g\omega_c{}^4 \Phi^{(n_s)}(r_s)}{\left(\omega_c{}^2 - \omega^2\right) + 2i\zeta_c \omega_c \omega} \right] e^{i\omega t} \cos(\pi\theta/\Theta), \end{aligned} \tag{3.36}$$

where g is the PPF feedback gain parameter which has units of s^2.

The feedback potential of the PPF controller (3.36) is applied as a boundary condition to the piezoelectric shear actuator. The implementation of the other boundary conditions on the top and bottom surfaces of the laminate and the interface conditions is similar to that of the forced vibration analysis discussed earlier. Since $\phi(\theta, t)$ and $\Phi^{(n_s)}(r_s)$ are functions of the unknown constants $B_m{}^{(n)}$, the controller parameters ω_c, ζ_c and g appear in the left-hand side matrix $[G(\omega)]$ in (3.30). The displacements and stresses are complex since the feedback potential (3.36) is complex. The magnitude and

phase of the displacements, electric potential, stresses and electric displacements with respect to the applied harmonic load can be inferred from their respective real and imaginary parts.

3.4. Finite Element Solution

The analytical solution is compared with a plane strain finite element solution for both the static deformation and natural frequencies to ensure that no algebraic errors are made during the implementation of the exact solution. The commercial finite element package ABAQUS/Standard 6.3-1 (Hibbitt, Karlsson & Sorensen, Inc., 2002) is used. A 2-D plane strain analysis is performed to obtain the natural frequencies and results of a static deformation. This implies that there is no motion in the x-direction and u_r, u_θ and ϕ are functions of r, θ and t. A generalized plane strain analysis is not performed due to the fact that ABAQUS does not possess a piezoelectric element that is capable of that type of analysis. This means that the natural mode shapes with motion in the x-direction will be missed.

The natural frequencies are extracted by finite element analysis using a Lanczos method. The alternative analysis offered by ABAQUS is a subspace iteration eigenvalue extraction. The Lanczos method is recommended in problem such as this because it is typically faster when the problem consists of a large number of degrees-of-freedom.

The element type for both analyses is the CPE8RE for the linear elastic and piezoelectric materials, respectively. The piezoelectric moduli for the linear elastic material are equal to zero. The CPE8RE element is needed for the elastic material due to the fact the potential degree-of-freedom is active for this element. The CPE8RE is a 2-D piezoelectric 8-node biquadratic plane strain element with reduced integration. The

quadratic element types are needed due to the fact that the geometry is inherently curved. A large number of linear elements would be needed to correctly represent the geometry.

The solution for the monolithic PZT-5A and the 4 layer composite shell both consisted of mesh containing 5600 elements and 17,257 nodes. The number of elements and nodes are not refined any further because a single refinement resulted in no change in the reported significant figures of the natural frequencies.

3.5. Results and Discussion

Results are presented for the hybrid laminates with the lamina comprised of either graphite-epoxy (Gr-Ep) or PZT-5A. The properties of these materials are listed in Table 2.1. In this study, both the Gr-Ep and PZT-5A of the hybrid and monolithic shells have their principal material axis in the circumferential direction (refer to Figure 3.1).

The study produced static deflection results, the natural frequencies and mode shapes and a steady-state forced vibration analysis of a [Gr-Ep /PZT-5A/ PZT-5A/Gr-Ep] hybrid shell with an embedded piezoelectric shear actuator and sensor. The natural frequencies and mode shapes are extracted for a monolithic PZT-5A cylindrical shell. Also, the stresses and displacements are examined for the first nine natural frequencies of the configurations studied. The four-layer laminated shell is further studied in a steady-state forced vibration analysis with a PPF control law implemented. The effect of the control law parameters is thoroughly investigated. (Note that the analytical implementation of the exact solution, incorporating active feedback control, can be found in Appendix B.)

3.5.1. Results for a 0° Monolithic Shear PZT-5A Cylindrical Shell

Consider a cylindrical shell of radius 0.25 m and extent angle $\Theta = 90^{\circ}$ in cylindrical bending vibration. The material of the shell is PZT-5A, with its principal material axis in the θ-direction. The radius-to-thickness ratios considered are 5, 10 and 100. This allows for analysis of both thick and thin shells. Also, the shell is considered with two different electrical boundary conditions at $r = R - H/2$ and $R + H/2$. The first of these boundary conditions is where the top and bottom surfaces are electrically closed ($\phi = 0$). The alternative boundary condition is where the top and bottom surfaces are considered electrically open ($D_r = 0$).

The first nine natural frequencies of the PZT-5A cylindrical shell with radius-to-thickness ratio of 5, 10, and 100 can be found in Table 3.1. Analysis using both of the electrical boundary conditions described above is performed and the results are listed in different columns. It should be noted that the mode is listed by the variable $\omega_k^{(m)}$, where k defines the axial mode shape and m defines the thickness mode shape. Also, the finite element solution is listed in parenthesis below the exact solution. Some of the finite element solutions have (--) listed. This is due to the fact that ABAQUS is not capable of performing a generalized plane strain analysis with piezoelectric materials and these modes have motion in the x-direction only. The number of terms used in the exact solution is determined by a convergence study using normalized values of the stress components of mode number 8 as the criterion. The number of terms in the series solution for all the results of this section was 40.

Table 3.1. The first nine natural frequencies of a monolithic 0° PZT-5A cylindrical shell

R/H = 5				*R/H* = 10				*R/H* = 100			
Mode	Closed, Hz	Mode	Open, Hz	Mode	Closed, Hz	Mode	Open, Hz	Mode	Closed, Hz	Mode	Open, Hz
$\omega_1^{(1)}$	271.325 (271.32)	$\omega_1^{(1)}$	271.758 (271.76)	$\omega_1^{(1)}$	137.541 (137.54)	$\omega_1^{(1)}$	137.599 (137.60)	$\omega_1^{(1)}$	13.8187 (13.819)	$\omega_1^{(1)}$	13.8187 (13.819)
$\omega_2^{(1)}$	1370.7 (1370.7)	$\omega_2^{(1)}$	1376.68 (1376.7)	$\omega_2^{(1)}$	731.284 (731.28)	$\omega_2^{(1)}$	732.294 (732.29)	$\omega_2^{(1)}$	74.9266 (74.927)	$\omega_2^{(1)}$	74.9278 (74.929)
$\omega_1^{(2)}$	2104.18 (--)	$\omega_1^{(2)}$	2104.18 (--)	$\omega_3^{(1)}$	1681.33 (1681.3)	$\omega_3^{(1)}$	1685.72 (1685.7)	$\omega_3^{(1)}$	177.695 (177.70)	$\omega_3^{(1)}$	177.701 (177.70)
$\omega_3^{(1)}$	2951.74 (2951.7)	$\omega_3^{(1)}$	2970.63 (2970.6)	$\omega_1^{(2)}$	2101.74 (--)	$\omega_1^{(2)}$	2101.74 (--)	$\omega_4^{(1)}$	321.602 (321.60)	$\omega_4^{(1)}$	321.62 (321.62)
$\omega_1^{(3)}$	3949.77 (3949.8)	$\omega_2^{(2)}$	4207.02 (--)	$\omega_4^{(1)}$	2924.94 (2924.9)	$\omega_4^{(1)}$	2936.31 (2936.3)	$\omega_5^{(1)}$	506.460 (506.47)	$\omega_5^{(1)}$	506.504 (506.51)
$\omega_2^{(2)}$	4207.02 (--)	$\omega_1^{(3)}$	4621.86 (4621.8)	$\omega_1^{(3)}$	3979.78 (3979.8)	$\omega_2^{(2)}$	4203.4 (--)	$\omega_6^{(1)}$	732.100 (732.11)	$\omega_6^{(1)}$	732.19 (732.20)
$\omega_4^{(1)}$	4807.85 (4807.8)	$\omega_4^{(1)}$	4843.19 (4843.2)	$\omega_2^{(2)}$	4203.34 (--)	$\omega_5^{(1)}$	4423.56 (4423.6)	$\omega_7^{(1)}$	998.328 (998.34)	$\omega_7^{(1)}$	998.494 (998.51)
$\omega_3^{(2)}$	6161.66 (--)	$\omega_3^{(2)}$	6161.66 (--)	$\omega_5^{(1)}$	4401.5 (4401.5)	$\omega_1^{(3)}$	4663.46 (4663.4)	$\omega_8^{(1)}$	1304.92 (1304.9)	$\omega_8^{(1)}$	1305.2 (1305.2)
$\omega_5^{(1)}$	6812.92 (6812.9)	$\omega_5^{(1)}$	6864.06 (6864.1)	$\omega_6^{(1)}$	6057.26 (6057.3)	$\omega_6^{(1)}$	6092.94 (6092.9)	$\omega_9^{(1)}$	1651.63 (1651.6)	$\omega_9^{(1)}$	1652.08 (1652.1)

As can be seen from Table 3.1, both the exact and finite element solutions are in excellent agreement. In fact, there are differences only in the fifth significant figure. It is important to note however, that the finite element solution only satisfies the governing equations in a weak sense, whereas the exact solution satisfies the governing equations point-wise throughout the domain. The agreement between the two solutions shows the validity of the approximations undertaken in the finite element solution.

It is also interesting to note that the modes that have motion predominately in the *r*-direction are influenced much more by the electrical boundary condition on the top and bottom surfaces than the other mode types. This fact can be seen from the mode $\omega_1^{(3)}$ when the radius-to-thickness ratio is 5. When the top and bottom surfaces are electrically closed, the first thickness mode occurs at 3949.77 Hz. The first thickness mode shifts to 4621.86 Hz when the boundary condition on the top and bottom changes to electrically open. This is a difference of about 700 Hz, which is a significant difference from a

design standpoint. This point shows the importance of knowing the electrical boundary conditions accurately.

Another important observation from Table 3.1 is that ABAQUS missed three of the first nine natural frequencies when the radius-to-thickness ratio is 5 due to lack of ability of to perform a generalized plain strain analysis. The first nine natural mode shapes corresponding to the natural frequencies listed in Table 3.1, with a radius-to-thickness radius of 5, are depicted in Figure 3.2. Electrically closed boundary conditions were used to generate these mode shapes. It should be noted that the plate extends infinitely in the x-direction in reality. The plate is truncated, however, to make the figure easier to read.

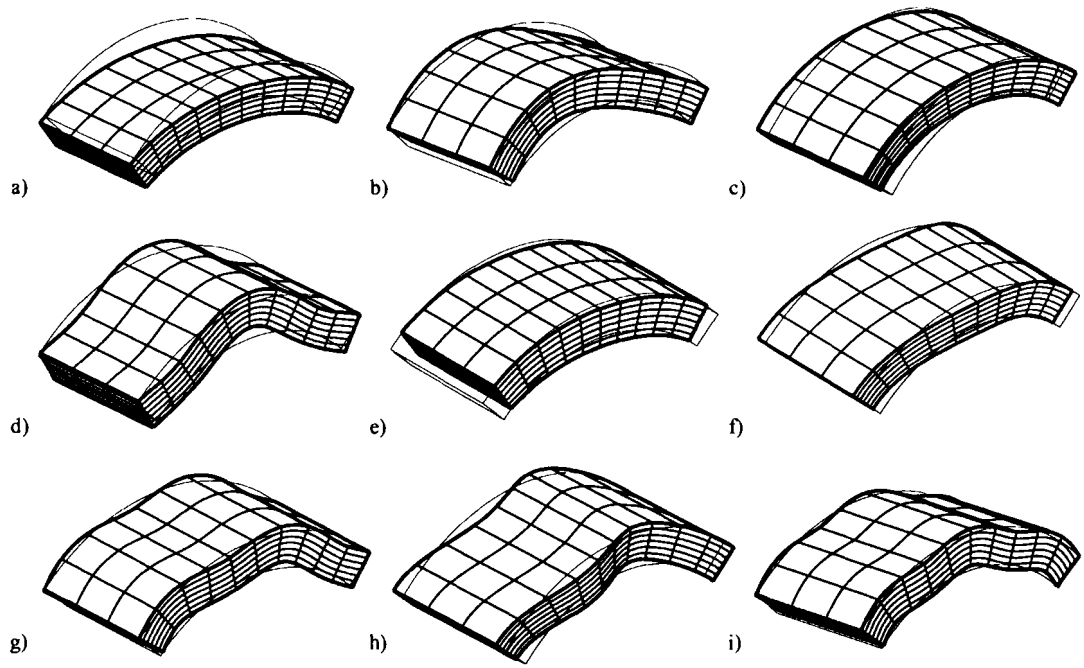

Figure 3.2. The first nine mode shapes of a monolithic PZT-5A cylindrical shell

The bending modes found in Figures 3.2(a), 3.2(b), 3.2(d), 3.2(g) and 3.3(i) are as expected from any classical shell theory. The out-of-plane modes of Figures 3.2(c), 3.2(f) and 3.2(h) can be captured using a generalized plane strain analysis utilizing

classical shell theory techniques. An interesting mode, that cannot be obtained using classical techniques, is also determined. This is the first thickness mode of Figure 3.2(e). The motion of this natural frequency is contraction in the circumferential direction, as well as a contraction and elongation in the thickness direction.

3.5.2. Static Deflection and Free Vibration Results for a [Gr-Ep/PZT-5A/PZT-5A/Gr-Ep] Shell

Consider a four-layer laminated hybrid shell with the following lamination scheme: [Gr-Ep/PZT-5A/PZT-5A/Gr-Ep]. This particular lamination scheme is studied because it will be used later in the active vibration suppression analysis. The exact configuration of the cylindrical shell can be found in Figure 3.3.

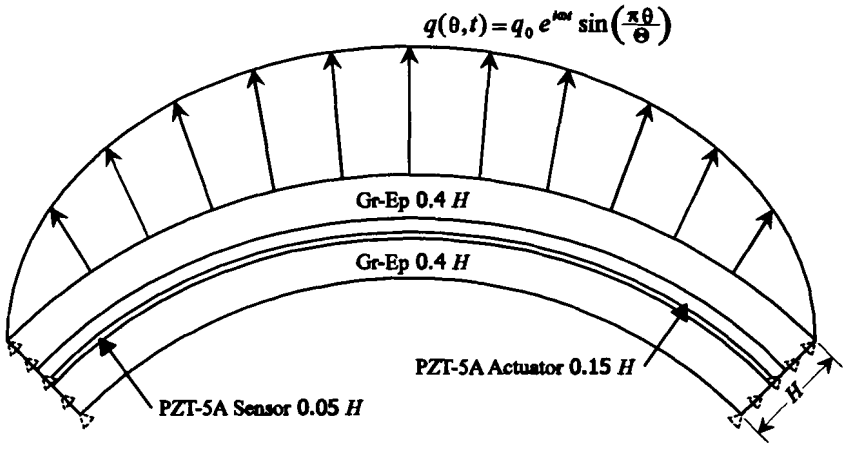

Figure 3.3. The geometrical configuration of a [Gr-Ep/PZT-5A/PZT-5A/Gr-Ep] hybrid shell

As can be seen from Figure 3.3, the Gr-Ep lamina comprises 80% of the total shell thickness. The remaining thickness is 15% for the PZT-5A actuator and 5% for the PZT-5A sensor. The addition of the sensor layer allows for a more realistic approach to the idea of active control since it is possible to accurately measure the electric potential

from a piezoelectric sensor. In the analysis of the laminated flat plate found in Chapter 2, the transverse displacement was used directly for the feedback control. However, direct measurement of the transverse displacement is difficult in practical applications.

Specifically, the cylindrical shell has a radius of 0.25 m, a radius-to-thickness ratio of 5 and an extent angle Θ of 90° (refer to Figure 3.1). The electrical interface and boundary conditions of each lamina are important to predicting the structures response. The inner and outer surfaces of the composite shell are assumed to be charge free. The interface between the actuator and sensor is considered to be at zero potential. The interface between the actuator and Gr-Ep layer is assumed to be electroded, and for the free vibration analysis this potential is assumed to be equal to zero. It is assumed that the potential ϕ and radial electric displacement D_r are continuous at the interface between sensor and Gr-Ep layer

Consider the static deformation of the four-layer hybrid shell depicted in Figure 3.3. The cylindrical shell is subjected to a static electrical potential of the form $\phi = \phi_0 \cos(p\theta)$ on the actuator surface at $r = R + H/10$. The results in Figure 3.4 are in the form of through-thickness plots of $\phi(0,r)$, $u_\theta(0,r)$, $\sigma_{\theta\theta}(\Theta/2,r)$ and $\sigma_{\theta z}(0,r)$. The exact solution consisted of 60 terms in the Frobenius series solution. The normalization constants C_0, ϕ_0 and e_0 have values of 21.1 GPa, 1 V and 12.322 C m^{-2}, respectively. As can be seen from Figure 3.4, the finite element solution agrees very well with the exact solution.

The applied potential causes the hybrid shell to deform radially inward and elongate in the circumferential direction. The circumferential displacement u_θ has a zigzag variation in the radial direction as shown in Figure 3.4(b). The average

circumferential displacement through the thickness of the composite shell is non-zero, unlike that of a statically deformed laminated composite plate with an embedded piezoelectric shear actuator (Vel and Batra, 2001b). This is due to the elastic coupling of the radial and circumferential deflections exhibited by shells. The maximum circumferential normal stress $\sigma_{\theta\theta}$ and transverse shear stress $\sigma_{r\theta}$ occur at the interface between actuator and the top layer of Gr-Ep. The first nine natural frequencies of the hybrid shell in Figure 3.3 are presented in Table 3.2. The finite element solution is listed in brackets next to the exact solution. The natural frequencies are much higher than that for the monolithic PZT-5A shell, even though the geometrical dimensions are exactly the same due to the stiff Gr-Ep layers.

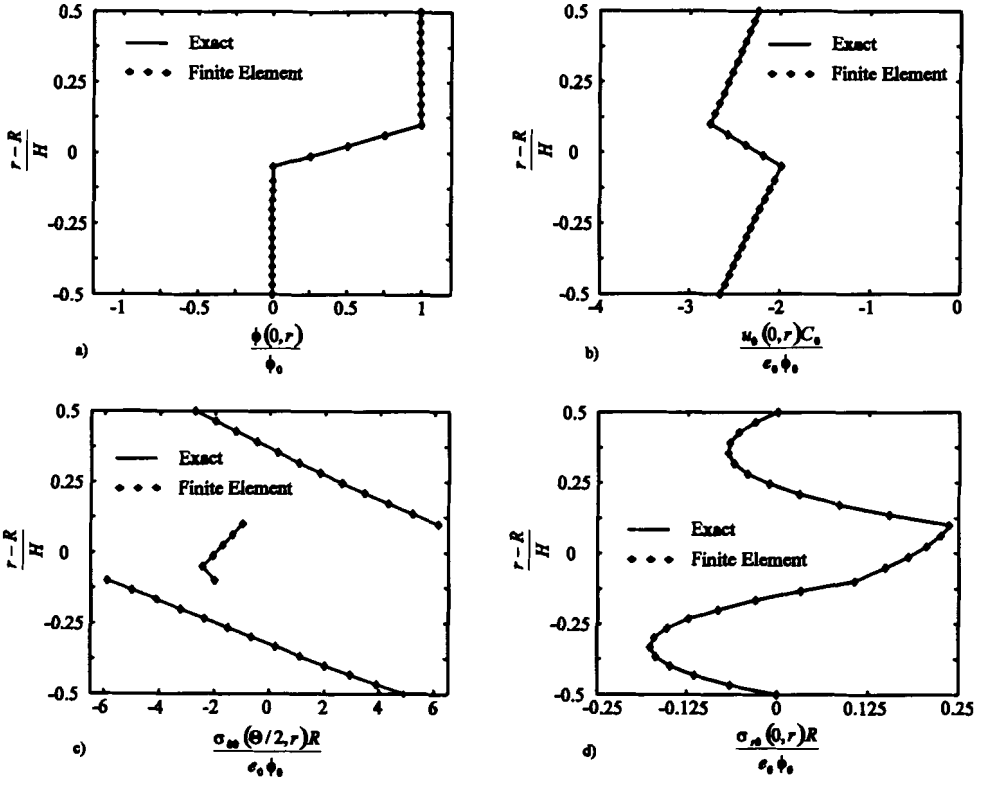

Figure 3.4. Through-thickness plots of potential, displacement and stresses of a statically deformed [Gr-Ep/PZT-5A/PZT-5A/Gr-Ep] shell

Table 3.2. The first nine natural frequencies of a [Gr-Ep/PZT-5A/PZT-5A/Gr-Ep] cylindrical shell

Mode	Natural Frequency, Hz
$\omega_1^{(1)}$	683.229 (683.23)
$\omega_1^{(2)}$	2393.43 (--)
$\omega_2^{(1)}$	2858.45 (2858.5)
$\omega_2^{(2)}$	4780.83 (--)
$\omega_3^{(1)}$	5254.74 (5254.7)
$\omega_3^{(2)}$	7156.76 (--)
$\omega_4^{(1)}$	7636.58 (7636.6)
$\omega_5^{(1)}$	9984.92 (9984.9)
$\omega_1^{(3)}$	10223.9 (10224)

The mode shapes corresponding to the first nine natural frequencies listed in Table 3.2 are depicted in Figure 3.5. The interfaces between each layer are highlighted with a thicker line.

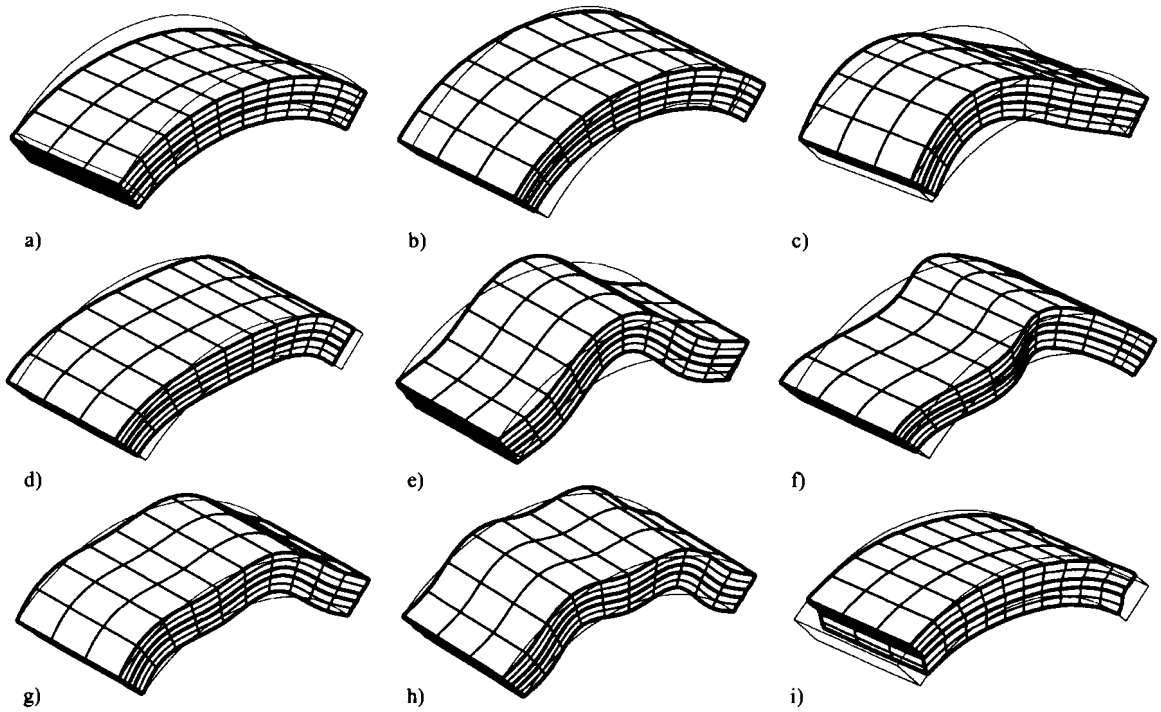

Figure 3.5. The first nine mode shapes of a [Gr-Ep/PZT-5A/PZT-5A/Gr-Ep] shell

As can be seen in Figure 3.5, there are five bending modes (Figures 3.5(a), 3.5(c), 3.5(e), 3.5(g) and 3.5(h)), three out-of-plane modes (Figures 3.5(b), 3.5(d) and 3.5(f)) and one thickness mode (Figure 3.5(i)). The most notable feature of Figure 3.5(i) is the nonlinearity of the circumferential displacement u_θ as a function of the radial coordinate. This displacement in the θ-direction is of the order of the displacement in the transverse direction although Gr-Ep is very stiff in the hoop direction.

The displacement and potential profiles through-the-thickness of the shell corresponding to the mode shapes described in Figure 3.5 can be found in Figure 3.6. The displacement and potential terms are normalized by dividing them by the absolute maximum value found through the thickness. The position along the circumferential direction where the variable has a maximum value is where the data is acquired for the plot.

As can be seen from Figure 3.6, a classical shell theory would do a poor job at predicting the displacements and potential for these modes. A reasonable estimate may be possible for the fundamental mode depicted in Figure 3.6(a) because the u_θ-displacement has an approximately linear profile, and the displacements u_r and u_x have a constant value throughout the thickness. The kinematic assumptions made by most classical theories would not accurately represent the higher modes of vibration. This fact is especially seen in Figure 3.6(h), where the displacement in the θ- and r-direction are highly nonlinear. Although the displacement u_x is constant through the thickness for the lower out-of-plane mode in Figure 3.6(b), it has a nonlinear profile for the higher out-of-plane mode in Figure 3.6(f). The electric potential distribution is approximately linear in

the sensor layer and the maximum potential occurs at the interface between the PZT-5A sensor and Gr-Ep layers except for the thickness mode in Figure 3.6 (i).

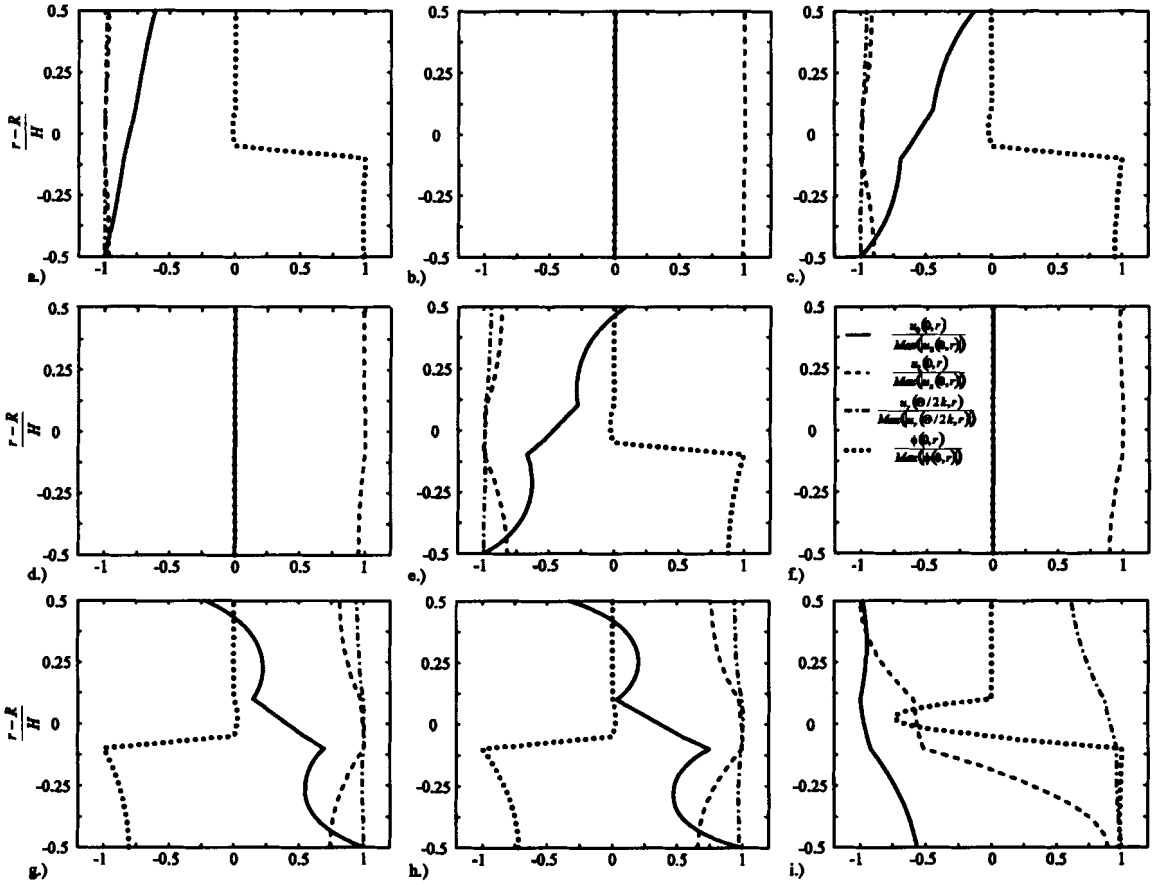

Figure 3.6. Through-thickness plots of displacements and potential for the first nine modes of a [Gr-Ep/PZT-5A/PZT-5A/Gr-Ep] shell

Through-the-thickness profiles of the Cauchy stress components $\sigma_{\theta\theta}$, σ_{rr}, $\sigma_{\theta z}$ and $\sigma_{r\theta}$ are shown in Figure 3.7. The circumferential normal stress $\sigma_{\theta\theta}$ for the bending modes found in Figures 3.7(a), 3.7(c), 3.7(e), 3.7(g) and 3.7(h) has a nonlinear profile for the higher modes of vibration. The transverse shear stress $\sigma_{r\theta}$ deviates from the parabolic profile for the higher modes of vibration.

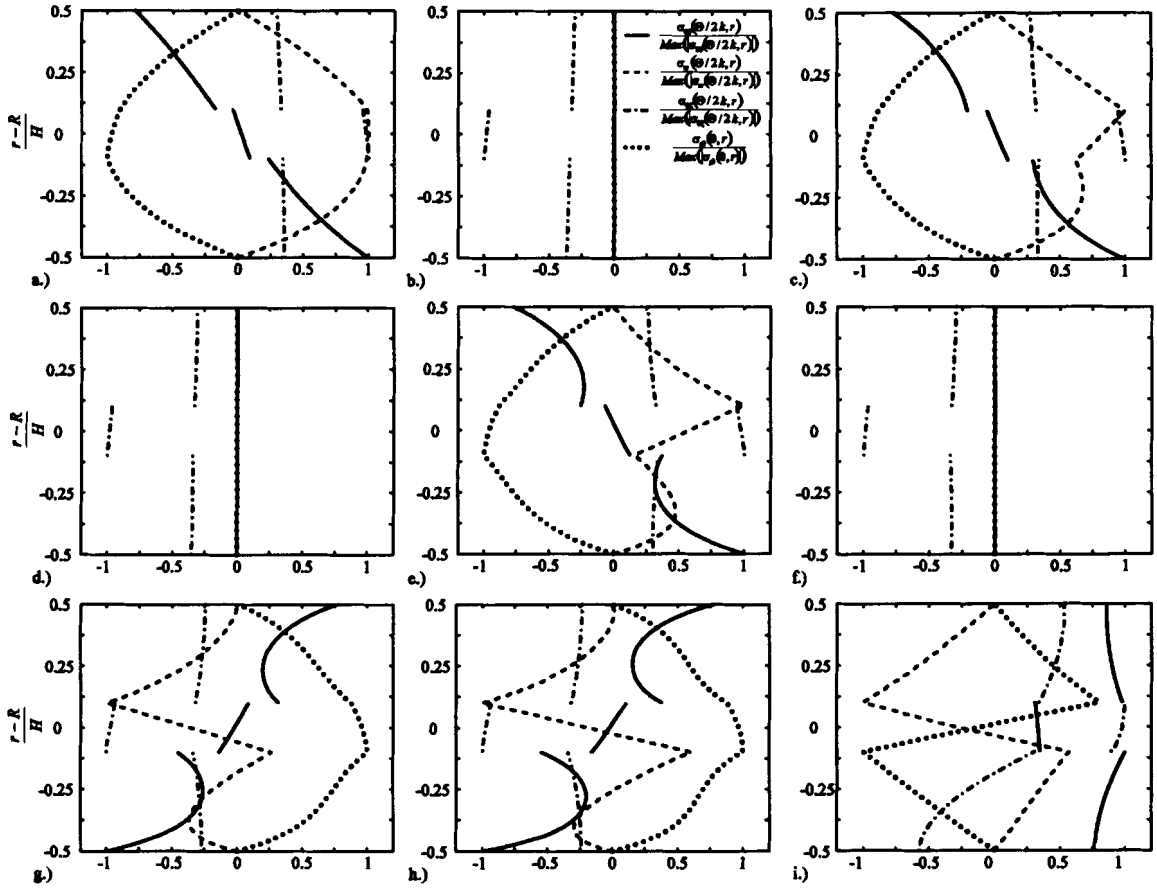

Figure 3.7. Through-thickness plots of stress for the first nine modes of a [Gr-Ep/PZT-5A/PZT-5A/Gr-Ep] shell

Numerical results for the displacements u_θ, u_r, u_x, stresses $\sigma_{\theta\theta}$, $\sigma_{\theta x}$, $\sigma_{r\theta}$, σ_{rr} and electric potential ϕ are listed in Tables 3.3 and 3.4 for the free vibration of the [Gr-Ep/PZT-5A/PZT-5A/Gr-Ep] cylindrical shell. Due to the lack of coupling between the in- and out-of-plane modes, the results are given in two separate tables.

Table 3.3. Numerical results of the bending and thickness modes of a [Gr-Ep/PZT-5A/PZT-5A/Gr-Ep] cylindrical shell with a radius-to-thickness ratio of 5

Mode	$\frac{u_\theta(0,R+H/2)}{u_r(\Theta/(2k),R+H/2)}$	$\frac{u_x(0,R+H/2)}{u_r(\Theta/(2k),R+H/2)}$	$\frac{\sigma_{\theta\theta}(\Theta/(2k),R+H/2)R}{C_0 u_r(\Theta/(2k),R+H/2)}$	$\frac{\sigma_{\theta x}(\Theta/(2k),R+H/2)R}{C_0 u_r(\Theta/(2k),R+H/2)}$
$\omega_1^{(1)}$	49.0339	0.223970	1.79998	-0.00108680
$\omega_2^{(1)}$	3.80600	0.236732	5.96013	-0.00459476
$\omega_3^{(1)}$	-2.34905	0.302802	9.56746	-0.00881569
$\omega_4^{(1)}$	-2.51037	0.166541	12.7747	-0.0129281
$\omega_5^{(1)}$	-2.60712	0.137470	15.8511	-0.0166725
$\omega_1^{(3)}$	-399.009	-1.89209	56.9388	-0.00918122

Mode	$\frac{\sigma_{r\theta}(0,R+H/4)R}{C_0 u_r(\Theta/(2k),R+H/2)}$	$\frac{\sigma_{rr}(\Theta/(2k),R+H/4)R}{C_0 u_r(\Theta/(2k),R+H/2)}$	$\frac{\phi(0,R)e_0}{C_0 u_r(\Theta/(2k),R+H/2)}$
$\omega_1^{(1)}$	16.6069	-0.0648929	0.00123365
$\omega_2^{(1)}$	49.7137	-0.191958	0.00496048
$\omega_3^{(1)}$	104.211	-0.266612	0.0113607
$\omega_4^{(1)}$	79.5715	-0.310141	0.00929069
$\omega_5^{(1)}$	84.5251	-0.346370	0.0105779
$\omega_1^{(3)}$	317.062	-1.77563	-1.12821

Table 3.4. The non-zero numerical results of the out-of-plane modes of a [Gr-Ep/PZT-5A/PZT-5A/Gr-Ep] cylindrical shell with a radius-to-thickness ratio of 5

Mode	$\frac{u_z(0,R+H/2)}{u_z(0,R+H/2)}$	$\frac{\sigma_{zz}(\Theta/(2k),R+H/2)R}{C_0 u_z(0,R+H/2)}$
$\omega_1^{(2)}$	1	-0.00485243
$\omega_2^{(2)}$	1	-0.0194091
$\omega_3^{(2)}$	1	-0.0436683

3.5.3. Results of the First Flexural Mode Active Vibration Suppression Analysis of a [Gr-Ep/PZT-5A/PZT-5A/Gr-Ep] Shell

Consider the [Gr-Ep/PZT-5A/PZT-5A/Gr-Ep] hybrid cylindrical shell discussed in the previous section of R = 0.25 m and R/H = 5. The shell is subjected to a harmonic forcing function of the form found in Figure 3.3. A PPF controller is employed for active vibration suppression. The second order PPF controller is forced by the electric potential

of the sensor at $\theta = 0$ and $r = R - H/10$. The feedback voltage (3.36) is applied to the PZT-5A actuator layer at $r = R + H/10$.

It is assumed that the Gr-Ep and piezoelectric laminae do not exhibit material damping. Therefore, any damping of the hybrid laminated shell is a result of the PPF controller. We seek to quantify the effectiveness of the piezoelectric shear actuator and the PPF controller for vibration suppression. For a given choice of control parameters ω_c, ζ_c and g, the steady-state response of the system is computed for a given forcing frequency ω. The magnitude and phase of the radial deflection is plotted as function of the forcing frequency ω for different controller parameters to obtain frequency response curves.

The effect of the controller parameters is investigated by changing each variable while keeping the others constant. The base PPF controller consists of the following parameters: $\omega_c = \omega_n$, $\zeta_c = 0.05$ and $g = 5 \times 10^{-8}$ s^2, where ω_n is the frequency of the mode targeted for active vibration suppression. The performance of the controller is evaluated for frequency parameters $\omega_c = 1.1\,\omega_n$, $\omega_c = 1.34\,\omega_n$, $\omega_c = 1.4\,\omega_n$, damping parameters $\zeta_c = 0.15$, $\zeta_c = 0.35$, $\zeta_c = 0.5$ and gain parameters $g = 5 \times 10^{-8}$ s^2, $g = 2.5 \times 10^{-8}$ s^2, $g = 7.5 \times 10^{-8}$ s^2 and $g = 9 \times 10^{-8}$ s^2.

The frequency response functions for different PPF controller parameters to achieve active damping of the first flexural mode (683.229 Hz, Table 3.2) of a [Gr-Ep/PZT-5A/PZT-5A/Gr-Ep] hybrid shell are shown in Figure 3.8. The magnitude of u_r at $\theta = \Theta/2$ and $r = R + H/2$ is plotted versus the forcing frequency for Figures 3.8(a), 3.8(c) and 3.8(e). The radial displacement is normalized by the quantities C_0, R and q_0,

which have values of 21.1 GPa, 0.25 m, and 1 Pa, respectively. Figures 3.8(b), 3.8(d) and 3.8(f) show the phase lag of the radial displacement with respect to the applied load.

The decrease in radial deflection in Figure 3.8 demonstrates that active vibration suppression of the first flexural mode is feasible using a PPF control law. As seen in Figure 3.8(a), maximum damping is achieved when ω_c is equal to the first flexural mode of the system contrary to experimental results, where a controller frequency that is either 1.3 or 1.45 times the target frequency resulted in higher system damping (Fagan, 1993; Dosch *et al.*, 1993). The discrepancy between this study and other experimenter's conclusions may be due the lack of material damping in the analytical model.

Upon examination of Figure 3.8(c), it is clear that maximum damping is achieved when the compensator damping ratio is small, which was also observed by Song *et al.* (2002). The response stems from the fact that as the compensator damping parameter is reduced, the active vibration suppression of the shell is extremely focused and it has a limited bandwidth. Therefore, the choice of controller damping ratio in practical applications would depend on how accurately the system dynamics are known. It is found that as the PPF gain parameter g is increased, the system damping ratio also increases

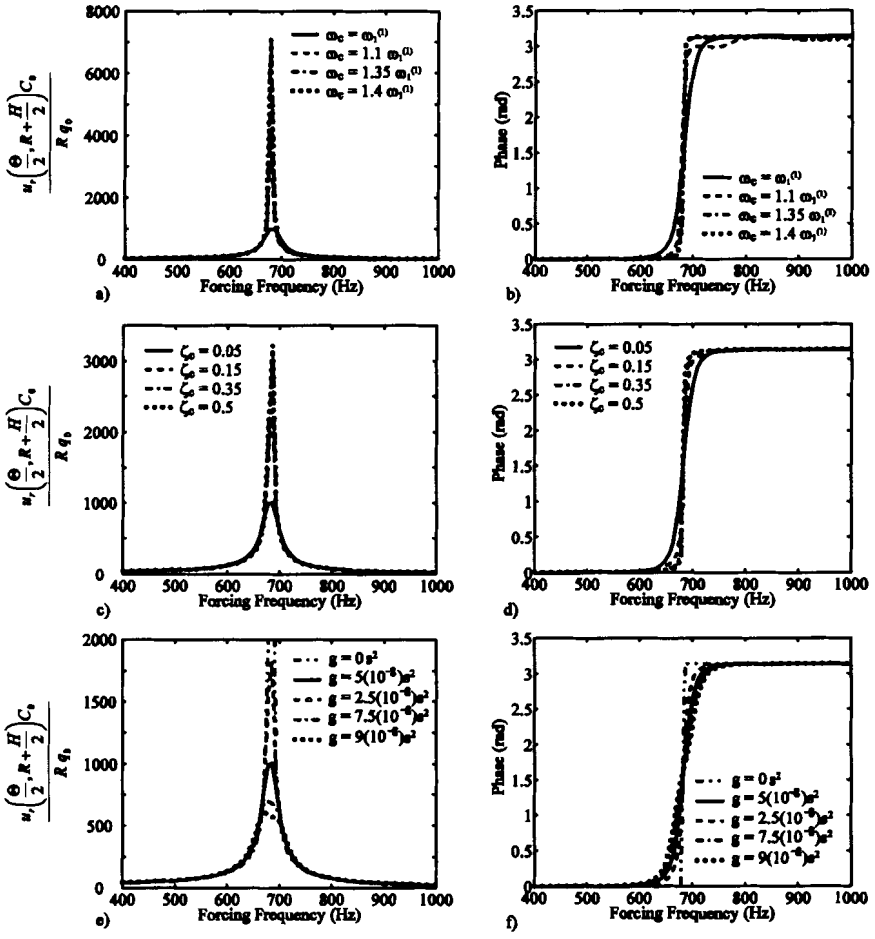

Figure 3.8. PPF compensator variable comparison plots of magnitude and phase for the first flexural mode of a [Gr-Ep/PZT-5A/PZT-5A/Gr-Ep] shell

3.5.4. Results of the First Thickness Mode Active Vibration Suppression Analysis of a [Gr-Ep/PZT-5A/PZT-5A/Gr-Ep] Cylindrical Shell

The efficacy of the PPF controller for the active vibration suppression of the first thickness mode of a [Gr-Ep/PZT-5A/PZT-5A/Gr-Ep] shell is considered next. The geometrical configuration of this study is exactly the same as that for the vibration suppression of the first flexural mode. The first thickness mode for this configuration has a natural frequency of 10223.9 Hz (Table 3.2). Again, as in the previous study of the first flexural mode, the present goal is to determine the effect of the controller parameters on the damping of the first thickness mode. The controller configuration is exactly the same as that for the suppression of the first flexural mode in Section 3.5.3.

Vibration damping of the thickness mode is achieved by the non-zero circumferential electric field component E_θ influencing the radial normal strain ε_{rr} and radial normal stress σ_{rr} through the piezoelectric coefficient e_{13}. Even though the piezoelectric shear actuator does not directly influence thickness motion through the radial electric field and piezoelectric coefficient e_{35}, damping through the secondary mechanism of circumferential electric field and piezoelectric coefficient e_{13} is an important aspect of achieving active vibration suppression.

Parametric studies of active vibration suppression of the first thickness mode of a [Gr-Ep/PZT-5A/PZT-5A/ Gr-Ep] cylindrical shell for different controller parameters are given in Figure 3.9. The normalized radial displacement u_r of the outer surface of the shell at $\theta = \Theta/2$ is plotted as a function of the forcing frequency from 10000 Hz to

10400 Hz. The radial displacement is normalized by C_0, q_0 and R, which have values of 21.1 GPa, 1 Pa and 0.25 m, respectively.

Figure 3.9 demonstrates that active control of the first thickness mode is feasible using piezoelectric shear actuators. Even though the controller uses a secondary piezoelectric effect for suppression, the amplitude at the resonance frequency is reduced. The suppression trend in Figure 3.9(a) is the same as that for the suppression of the first flexural mode in Figure 3.8(a). As the controller frequency is increased, the system damping becomes smaller. Unlike the frequency response function of the flexural mode, as the controller parameter ω_c is increased from ω_n to $1.1\omega_n$, the peak appears to have shifted to the right. As the controller ω_c is further increased to $1.35\omega_n$ and $1.4\omega_n$, the response curve shifts back to the left.

As far as the system response in Figure 3.9(c), the same conclusion as that for the suppression of the first flexural mode applies in terms of compensator damping parameter. As the damping parameter is increased, less system damping occurs, but the effective range of the control law increases. The system damping is observed to increase as the gain parameter is increased. In practice, this parameter is merely limited by the amount of voltage that can be safely applied to the piezoelectric actuator without de-poling it. The peak response shifting to the right as the gain parameter is increased in Figure 3.9(e) is different from that of the first flexural mode in Figure 3.8 (e). This may be due to the fact that a secondary piezoelectric effect is used or related to the dynamics of the thickness mode.

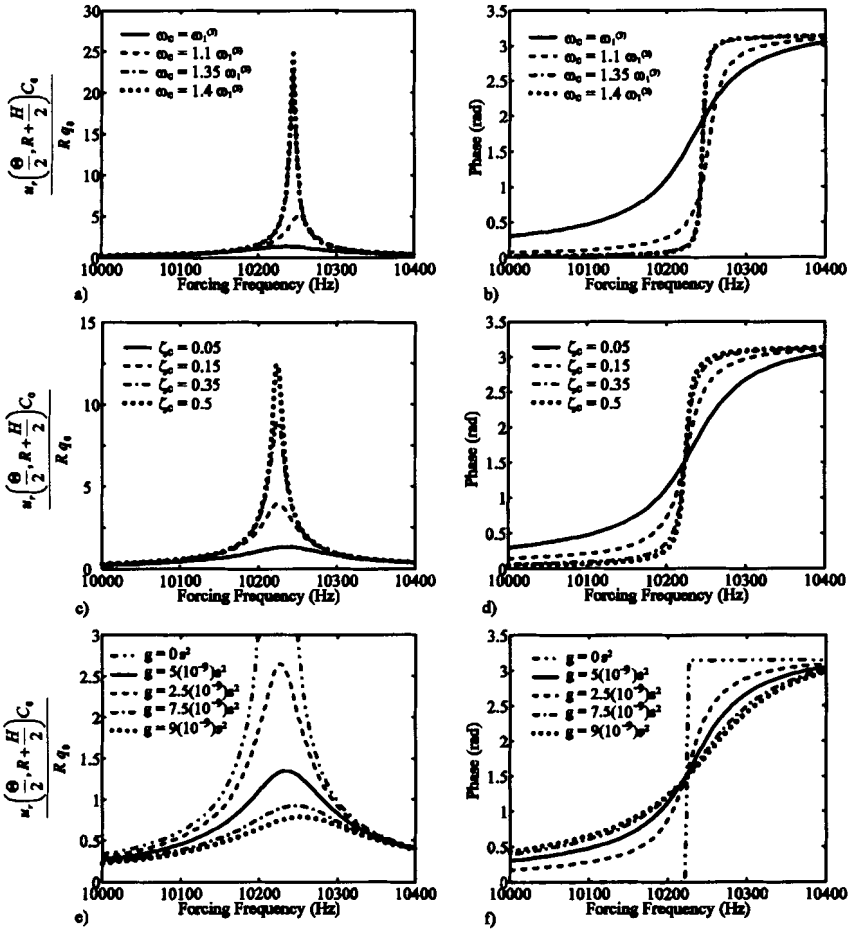

Figure 3.9. PPF compensator variable comparison plots of magnitude and phase for the first thickness mode of a [Gr-Ep /PZT-5A/PZT-5A/ Gr-Ep] shell

Chapter 4

EXPERIMENTAL AND FINITE ELEMENT INVESTIGATION OF ACTIVE VIBRATION SUPPRESSION OF A CANTILEVER SANDWICH BEAM USING PIEZOELECTRIC SHEAR ACTUATORS

This chapter details an experimental and finite element investigation of the active vibration suppression of a cantilever beam using piezoelectric shear actuators. Results are presented for an aluminum sandwich beam containing a foam core and embedded shear actuators. Active vibration suppression is implemented using positive position feedback (PPF) control and strain-rate feedback (SRF) control. Experimentally obtained frequency response curves compare well with those obtained by finite element analysis. The results clearly demonstrated that piezoelectric shear actuators are effective as active elements in a vibration suppression system.

The first section discusses the motivation for the research. The second section describes the experimental setup and the implementation of the feedback control system in real-time. The next section details the finite element model, followed by the results and discussion.

4.1. Rationale

For the past decade, several researchers (Trindade *et al.*, 2000; Raja *et al.*, 2002) have demonstrated the effectiveness of piezoelectric shear actuators for active vibration suppression in smart structures. However, to date all investigations of active damping using piezoelectric shear actuators are limited to analytical or computational research. To the author's knowledge, there has not yet been any experimental work to demonstrate that the piezoelectric shear coefficient can be utilized for the vibration suppression of real structures. Therefore, it is a goal of this work to examine the efficacy of the piezoelectric shear coefficient for active feedback control. PPF and SRF feedback control laws, described in Chapter 1, are utilized for the active control of vibrations. In practical applications, it is prudent to design and develop active vibration suppression systems using theoretical and/or numerical models in order to reduce development time and costs. However, before doing so, we need to validate the theoretical/numerical models by comparing it with experimental results for a simple configuration, such as a sandwich cantilever beam. An accurate analysis of a cantilever beam using the analytical procedure presented in Chapters 2 and 3 is difficult due to edge effects at the clamped and free edges and the three-dimensional stress state near the embedded shear actuators. Therefore, we analyze the vibration suppression of a sandwich cantilever beam using a finite element model and compared the numerical results with experiments.

The first four natural frequencies of the system are determined using experimental and numerical means and then compared. In addition to the finite element natural frequencies, the corresponding mode shapes are also determined. The uncontrolled frequency response functions are found numerically and experimentally and compared.

An experimental parametric study of the PPF controller parameters on the damping of the fundamental mode is then performed. A finite element solution for two cases in the parametric study is found to ensure that the controller is numerically implemented correctly. Next, a smaller parametric study on the active vibration suppression of the second mode of vibration using PPF control is undertaken to determine if the parameters have a different effect on damping of this mode. The feasibility of the active damping of two modes using a single actuator, and the active vibration suppression of the cantilever beam utilizing a SRF control law is also investigated. Finally, the active vibration suppression of the hybrid beam subjected to a harmonic tip force excitation is studied experimentally and numerically.

4.2. Experimental Setup

A sandwich cantilever beam consisting of aluminum facings and a foam core with two embedded piezoelectric shear actuators was fabricated. The components of the sandwich beam were firmly bonded together using an adhesive film which cured at low temperature in an autoclave. The exact configuration of the sandwich beam used in this study is depicted in Figure 4.1. The facings of the beam are composed of 6061-T6 aluminum. The core is composed of foam (Baltek Airex R82.80) and two PZT-5A shear actuators of equal thicknesses. The axially-poled piezoelectric actuators were purchased from Morgan Electro Ceramics.

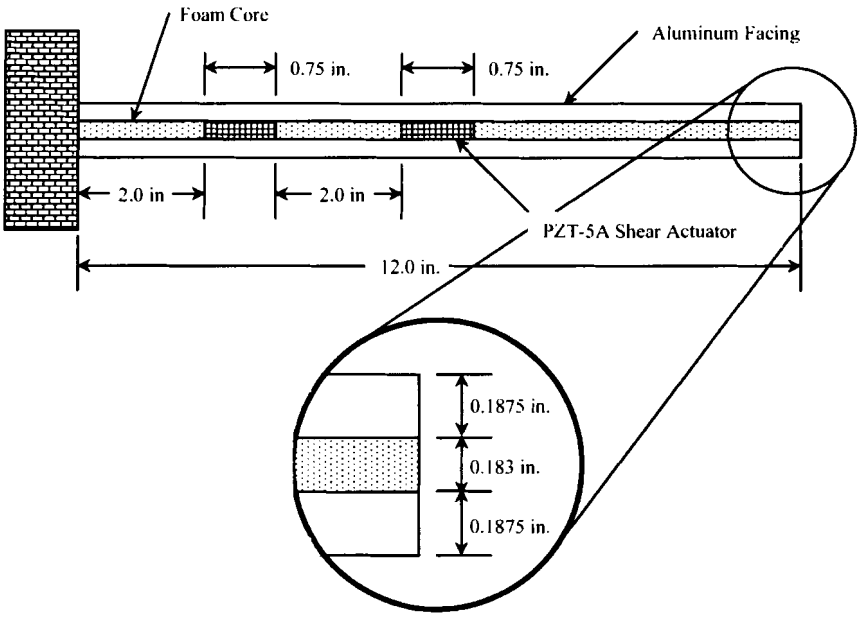

Figure 4.1. The geometrical configuration of the cantilever beam

As can be seen from Figure 4.1, the beam is 0.305 m (12 in.) in length and 0.0142 m (0.558 in.) in total thickness. The Young's modulus, Poisson's ratio and density of the aluminum facings are 69 GPa, 0.33 and 2730 kg / m^3, respectively. The Young's modulus, shear modulus and density of the Baltek Airex R82.80 foam core are 62 MPa, 23 MPa and 80 kg / m^3, respectively (Baltek Corporation, n.d.). The PZT-5A is transversely isotropic with its principal material direction oriented along the longitudinal axis of the beam. The electric field is applied through the thickness of the beam via electrodes at the interface between the actuator and aluminum facings. The manufacturer did not provide the necessary material properties for the piezoelectric material when it is poled in x_1-direction as depicted in Figure 1.1 (Berlincourt and Krueger, n.d.). The relevant material properties were inferred through fourth order and third order tensor transformations of the elasticity and piezoelectric tensors, respectively, of PZT-5A poled in the x_3-direction. Although the material properties thus obtained may not be accurate, it

should provide reasonable values in the absence of published data or the necessary equipment to measure the piezoelectric properties.

The result of these tensor transformations can be found in Table 4.1. It should be noted that the material properties of the axially-poled PZT-5A are different from those used in the analytical studies in the previous chapters. This difference can be attributed to the value of Poisson's ratios ν_{23} and ν_{13} of PZT-5A. In our earlier analyses it was assumed that $\nu_{23} = \nu_{13} = 0.38$, whereas the material properties in Table 4.1 are based on the manufacturer's published values $\nu_{23} = \nu_{13} = 0.4404$. All other material properties are identical.

Table 4.1. The material properties of PZT-5A poled in the x_1-direction (refer Figure 1.1)

Material Property	Value	Material Property	Value
C_{1111} (GPa)	111	e_{111} (C m^{-2})	15.8
C_{2222} (GPa)	121	e_{122} (C m^{-2})	-5.4
C_{3333} (GPa)	121	e_{133} (C m^{-2})	-5.4
C_{1122} (GPa)	75.2	e_{123} (C m^{-2})	0
C_{1133} (GPa)	75.2	e_{113} (C m^{-2})	0
C_{2233} (GPa)	75.4	e_{112} (C m^{-2})	0
C_{2323} (GPa)	22.6	e_{211} (C m^{-2})	0
C_{1313} (GPa)	21.1	e_{222} (C m^{-2})	0
C_{1212} (GPa)	21.1	e_{233} (C m^{-2})	0
ϵ_{11} (10^{-10} F/m)	150.45	e_{223} (C m^{-2})	0
ϵ_{22} (10^{-10} F/m)	153.1	e_{213} (C m^{-2})	0
ϵ_{33} (10^{-10} F/m)	153.1	e_{212} (C m^{-2})	12.3
Density ρ (kg/m^3)	7750	e_{311} (C m^{-2})	0
		e_{322} (C m^{-2})	0
		e_{333} (C m^{-2})	0
		e_{323} (C m^{-2})	0
		e_{313} (C m^{-2})	12.3
		e_{312} (C m^{-2})	0

The experimental setup of the cantilever beam is shown in Figure 4.2. The beam is clamped using a thick steel plate bolted to a heavy block of steel. This required that the beam be constructed 6" longer than the cantilever section with a polycarbonate core to withstand the large clamping force of the bolts.

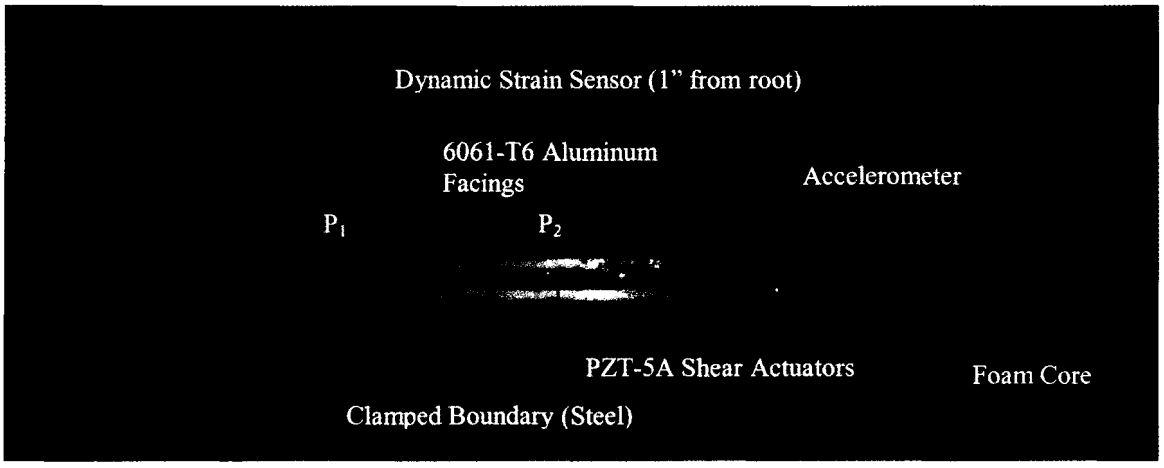

Figure 4.2. Experimental setup of the cantilever beam

The two PZT-5A shear actuators are labeled as P_1 and P_2. In the first part of the study, the excitation actuator that is closest to the clamped end, denoted by P_1, is used as a disturbance actuator to excite the beam. Actuator P_2 is the control actuator that is used for vibration suppression. PZT-5A actuators require an electric field intensity of 100 V/mm to 500 V/mm to obtain significant actuation. Since the piezoelectric shear actuators utilized in this study are 4.648 mm thick, it is necessary to use a voltage amplifier to produce large voltages. In this study, a Trek Piezo Driver (model PZD700) voltage amplifier with dual channels is used. A gain of 68 V / V is used for each channel of the device since the voltage input to the amplifier from the control system is in the range of ±10 V.

In the second part of the study, a low-voltage piezoelectric stack and a steel block are bonded to the tip of the cantilever beam, as depicted in Figure 4.3, to form a proof-

mass actuator that is used as a disturbance source to provide a repeatable vibration input to the beam at any desired frequency and amplitude. The embedded piezoelectric shear actuators P_1 and P_2 are used to suppress the vibration caused by the proof-mass actuator.

One end of the low-voltage piezoelectric stack (Piezo Systems, Inc. model TS18-H5-202, 0.4 in. x 0.4 in. x 0.72 in. in size) is bonded to the end of the cantilever beam depicted in Figure 4.2, and the other end is fixed to a steel block of cross sectional dimensions 0.996 in. x 0.996 in. and 1.006 in. thickness. The steel block and stack actuator have masses of 0.126 kg and 0.015 kg, respectively. When a voltage is applied to the piezoelectric stack actuator, it will extend or contract in the direction perpendicular to the longitudinal axis of the beam. As a harmonic excitation is applied to the stack, the inertia of the stack and steel block causes a force to be generated at the tip of the beam. This simulates a phenomenon akin to an unbalanced motor at the end of the beam. An AVC Instrumentation 790 Series power amplifier with a gain of 10 V/V is used to drive the piezostack.

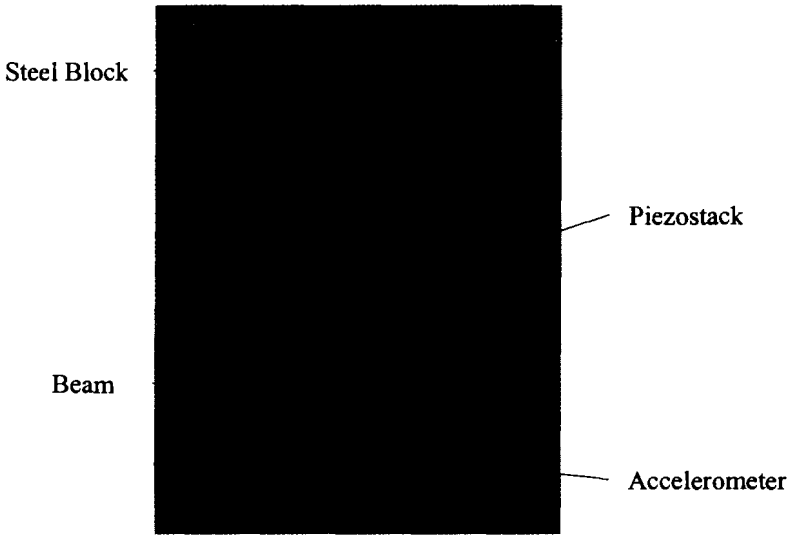

Figure 4.3. The proof-mass actuator used for force excitation at the tip of the beam

Two sensors are integrated with the cantilever beam experimental setup of Figure 4.2. A dynamic strain sensor (PCB model 740802) is used as the feedback control variable, and an accelerometer (PCB model 352A24) is used to measure the tip vibration and to quantify the effectiveness of the vibration suppression system. The outputs from both sensors are passed through a PCB signal conditioner (model 482A20) before acquisition of the respective signals.

The frequency response function and time history plots of the system are determined using the data acquisition hardware SigLab (model 20-22, two analog inputs and two analog outputs), which is a signal-processing unit that acts as a function generator, oscilloscope and network analyzer that can be accessed through a Matlab interface. The unit is capable of capturing frequencies up to 20,000 Hz. The frequency response function and time history plots are determined using the VNA and VOS modules in the SigLab software.

The PPF and SRF control laws are implemented using a dSPACE digital signal processing module (model DS1104). dSPACE is a rapid hardware prototyping system that uses Matlab and Simulink. The PPF and SRF controllers are implemented using a Simulink block diagram. The Simulink block diagrams for the PPF control of a single mode, as well as the control of two modes simultaneously are shown in Figure 4.4.

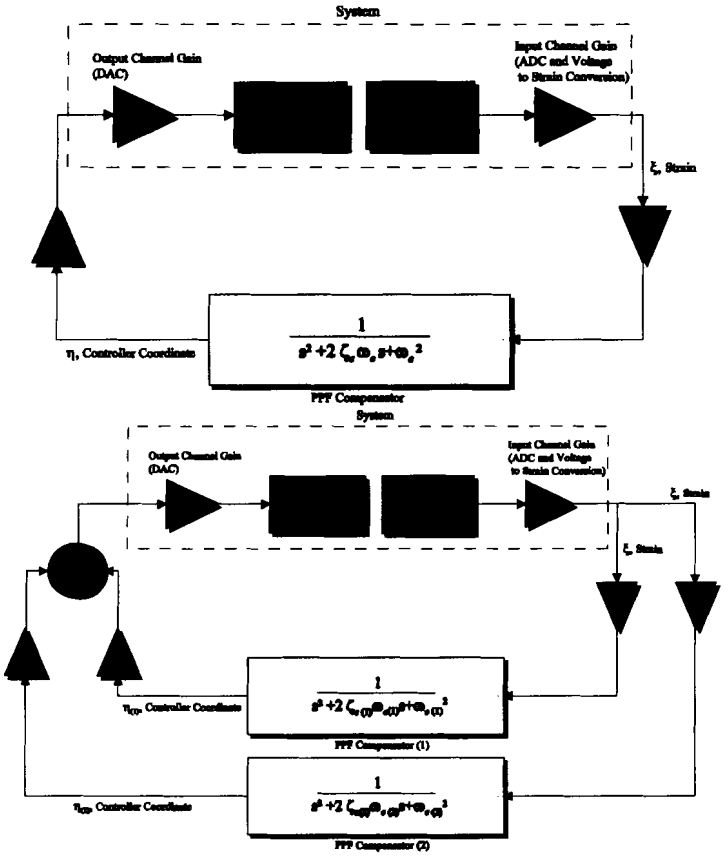

Figure 4.4. Simulink PPF block diagrams for control of one and two modes

The primary difference in the implementation of SRF control is that the derivative of the strain signal is applied to the compensator, and the feedback gain has the opposite sign of that of a PPF controller shown in Figure 4.4 (refer to Appendix C for the block diagram).

4.3. Finite Element Model

The numerical model used in this study utilizes the finite element method to analyze the active feedback control of a cantilever beam. The commercial finite element analysis package ABAQUS/Standard 6.3-1 (Hibbitt, Karlsson & Sorensen, Inc., 2002) is used. A two-dimensional plane stress analysis of the adaptive beam is performed. The CPS8R and CPS8RE 8-node biquadratic plane stress elements with reduced integration

are utilized for the elastic and piezoelectric materials, respectively. A three-dimensional finite element analysis is not performed due to the increased computer resources required for such an analysis.

Three separate analyses were performed using ABAQUS. The natural frequencies and mode shapes are computed using the FREQUENCY subroutine. The frequency response function of the system is computed using the DIRECT, STEADY STATE subroutine. This includes both the uncontrolled and actively controlled response of the cantilever beam. Finally, the transient response of the system without and with PPF control is determined with the IMPLICIT, DYNAMIC subroutine.

4.3.1. Computation of Natural Frequencies and Mode Shapes

The natural frequencies and mode shapes of the uncontrolled system shown in Figure 4.1 are extracted using the Lanczos method. ABAQUS offers both the Lanczos and subspace method for eigenvalue (natural frequency) extraction. The Lanczos method is usually preferred when large numbers of degrees-of-freedom are used; therefore, this method is chosen to extract the natural frequencies in this study.

4.3.2. Computation of Frequency Response Function

The frequency response function of the uncontrolled system is determined by computing the steady-state response of the beam to a harmonically applied potential to the disturbance actuator P_1 at discrete frequencies using the DIRECT, STEADY STATE analysis subroutine of ABAQUS. The complex magnitude of acceleration at the tip of the beam is used to produce the frequency response function.

Computing the frequency response curve of the cantilever beam with feedback control required the development of a custom FORTRAN program that is executed in tandem with the steady-state analysis subroutine in ABAQUS (refer to Appendix D for the FORTRAN program). The frequency of the applied potential to the disturbance actuator P_1 is chosen and the program arbitrarily assigns a complex voltage V to the control actuator P_2. A steady-state finite element solution is obtained using this assumed electric potential. The strain near the root of the beam (refer Figure 4.2) is determined from the finite element solution and the corresponding steady-state feedback control voltage V_c is computed based on either a PPF or SRF control law. The computed value of control potential V_c to P_2 is compared with the assumed potential V to P_2. The analysis procedure is iterated until the difference between the prescribed potential and calculated control potential is zero. This is accomplished by defining a complex function $f(V) = V_c - V$, which calculates the difference between the computed and assumed control voltages. The complex zero of the analytic function $f(V)$ is obtained using Muller's method (Press *et al.*, 1992) which is a generalization of the secant method of root finding using quadratic 3-point interpolation. The root V to the equation $f(V) = 0$ obtained using the Muller's method is the voltage to the control actuator P_2 which satisfies the feedback control law. The process is repeated for several discrete frequency values to create a frequency response curve.

4.3.3. Transient Analysis with Active Vibration Suppression

A transient analysis is also performed using the finite element method by utilizing the IMPLICIT, DYNAMIC subroutine in ABAQUS. This analysis is useful for determining the efficacy of the PPF controller in the time domain. The proof-mass

actuator is used to induce an excitation at the tip of the cantilever beam and the piezoelectric shear actuators P_1 and P_2 are used for active vibration suppression. ABAQUS uses a Newmark-β numerical integration scheme to find the transient solution. In this analysis, the beam is excited by the proof-mass actuator for 0.1 *s*. After that, the vibration amplitude decreases either due to natural damping or to active vibration suppression due to PPF control. The time increment is chosen so as to attain fifty data points for each cycle of structural response during the excitation, and twenty data points during the free vibration for 1 s after the excitation is stopped. The forcing function is chosen to equal the fundamental frequency of the system (74.443 Hz); therefore, the time increment is chosen to be 2.6866×10^{-4} s and 6.7165×10^{-4} s during the excitation and free vibration, respectively.

A PPF control law is incorporated into the transient analysis (refer to Appendix E for custom FORTRAN subroutines linked to ABAQUS). The second order controller is modeled directly as second order system (refer Equation 1.2) in the ABAQUS model as a spring-mass-damper system. After each time step, the strain near the root (1" from base) of the beam is found and multiplied by the square of the compensator frequency ω_c and applied as a force to the spring-mass-damper compensator. In addition, after every time increment the displacement of the mass, which is the compensator coordinate, is multiplied by the square of the compensator frequency and a PPF scalar gain and applied as the feedback voltage to the control actuator P_2. Since the value of the control voltage at the next time increment is determined from the present state of deformation, the algorithm is inherently explicit. Basing the future values not only upon values at the present time step, but also the slope (determined from the present and previous values) at

this point minimizes the controller voltage error generated. A small time step also limits the error.

The spring stiffness, mass and damping ratio are determined from chosen values of PPF controller frequency ω_c and damping parameter ζ_c. The value of the scalar gain parameter g is set equal to that used in the experimental investigation. The spring-mass-damper system that simulates a PPF compensator system is analyzed simultaneously with the transient finite element model of the cantilever beam in ABAQUS. A CONN2D2 connector element is utilized to model the spring and damper of the PPF compensator.

A Rayleigh structural damping model is implemented in the transient finite element analyses to obtain a realist response for the uncontrolled free vibration of the cantilever beam. One of the disadvantages of the Rayleigh damping model is that the damping coefficient depends on the frequency through only two constants that are usually chosen by matching the damping coefficient to the experimental values at two of the system's natural frequencies. Damping can also be analyzed using a viscoelastic material model of the foam core. However, the viscoelastic material properties of the core in the time or frequency domain are not known. Determination of these properties is not easily accomplished and beyond the scope of this thesis.

The experimentally measured value of the damping ratio using the logarithmic decrement (Rao, 1995) is $\zeta = 0.007773$. For a Rayleigh damping model, the damping ratio is related to structural frequency in the following manner:

$$\zeta_i = \frac{\alpha}{2\omega_i} + \frac{\beta\omega_i}{2} \tag{4.1}$$

where ζ_i and ω_i are the damping ratio and frequency of the i^{th} mode, respectfully, α is the mass proportional damping constant and β is the stiffness proportional damping constant. Since we are primarily interested in the first mode of vibration, we have assumed a stiffness proportional damping ($\alpha = 0$) whereby the damping ratio is proportional to the i^{th} natural frequency. The damping parameter β is determined from the experimentally measured damping ratio and frequency of the fundamental mode of vibration. There is assumed to be no damping in the natural frequency extraction and dynamic steady-state analyses.

A mesh convergence study is performed to ensure that the finite element model produces solutions that have converged to an acceptable limit. The fourth natural frequency of the system without the proof-mass actuator is used as the convergence criterion. The results of this study can be found in Figure 4.5 as a plot of the number elements in the mesh versus the fourth natural frequency.

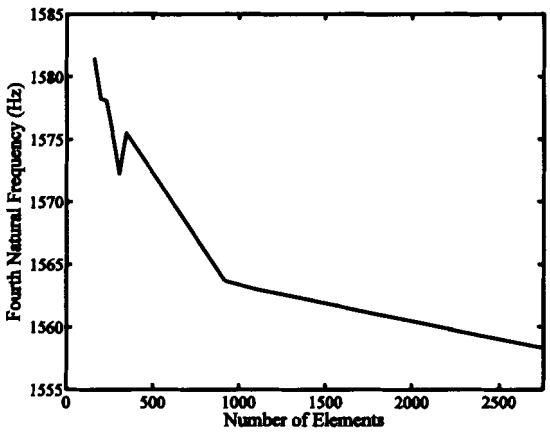

Figure 4.5. A convergence study of the fourth natural frequency of the beam

As can be seen from Figure 4.5, the solution has indeed converged by the time the number of elements in the mesh reaches 2754 elements. Therefore, 2754 elements and

8893 nodes are used to model the hybrid cantilever beam. The resulting mesh for the beam used in all of the finite element analyses can be found in Figure 4.6.

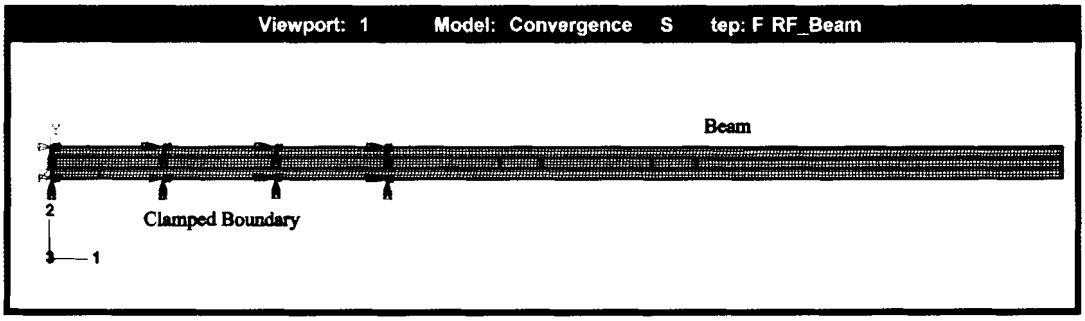

Figure 4.6. The finite element mesh of the hybrid beam

The proof-mass actuator (refer Figure 4.3) is also incorporated into the finite element model. The piezostack is modeled as a monolithic piezoelectric material. Due to the lack of reliable properties of the piezostack from the manufacturer, the equivalent piezoelectric strain coefficient of the stack was obtained by comparing experimental results with numerical simulations. This resulted in a piezoelectric strain coefficient of 7.955×10^{-8} m / V for the stack. It is noted that this value was not independently confirmed due lack of facilities to make a direct measurement. The finite element mesh for the proof-mass actuator is shown in Figure 4.7.

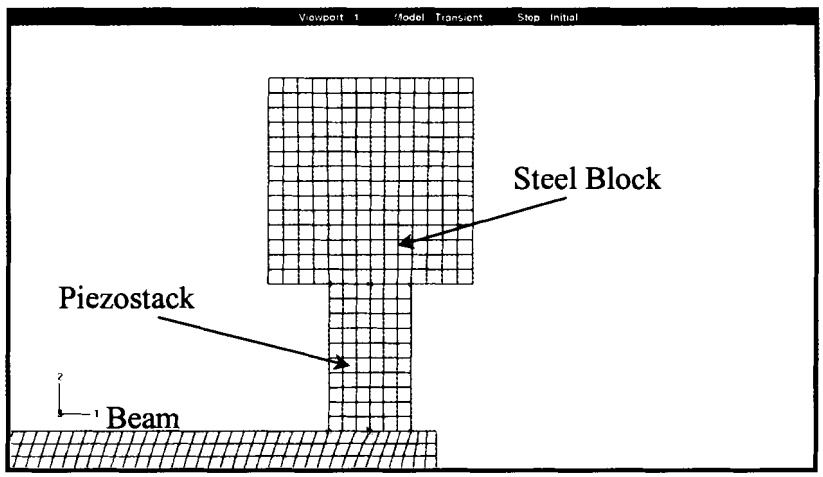

Figure 4.7. Finite element model of the proof-mass actuator

4.4. Results and Discussion

In this section, the first four natural frequencies of the beam are determined using the experimental setup and the finite element model. The corresponding numerically obtained mode shapes are also presented. Experimental and finite element frequency response functions for the system are compared next, followed by an experimental parametric study to determine the effect of PPF controller parameters on system damping. The active vibration suppression of the cantilever beam using SRF control is also examined through experiments and numerical simulations. Finally, the transient response of the PPF controlled cantilever beam is analyzed.

4.4.1. Comparison of Natural Frequencies and Frequency Response Functions

The first four experimental and finite element (FE) natural frequencies of the system are presented in Table 4.2. The percent difference between the two values, with respect to the FE result, is listed in the third column. It is clear that the finite element model accurately predicts the first four natural frequencies of the cantilever beam. The largest error of 2.9858% occurs in the first mode. In this mode, the numerical model seems to be either slightly stiffer or possess a different mass distribution. This error is still within acceptable engineering limits, however.

Table 4.2. Comparison of the first four natural frequencies of the experimental setup and finite element model

Mode	Experimental Natural Frequency (Hz)	Finite Element Natural Frequency (Hz)	% Diff.
1	123.0625	126.85	2.9858
2	495.7125	495.12	0.11967
3	1098.275	1094.6	0.33574
4	1538.200	1558.3	1.2899

It is interesting to note that for the second mode the finite element model is in excellent agreement with the experimental result. The difference is only 0.11967%. The agreement for the last two modes is still good, but the differences, in terms of the number of Hz, start to increase as mode number increases. This is expected due to the fact as the mode number increases the experimental natural frequencies are more dependent on any small differences in material properties, construction defects, etc. The finite element model is an idealization; therefore, as mode number increases subtle differences between the two become more apparent.

The mode shapes corresponding to the first four FE natural frequencies listed in Table 4.2 are shown in Figure 4.8. As can be seen in Figure 4.8(a), the deformed shape of the beam is as one would expect for the fundamental mode of a cantilever beam. The second mode, depicted in Figure 4.8(b), deviates slightly from what would be expected for a cantilever beam. This discrepancy stems from the fact that the PZT shear actuators have much higher stiffness than the foam core material. Figures 4.8(c) and 4.8(d) show that the effect of the stiffness discontinuities is more pronounced for modes 3 and 4.

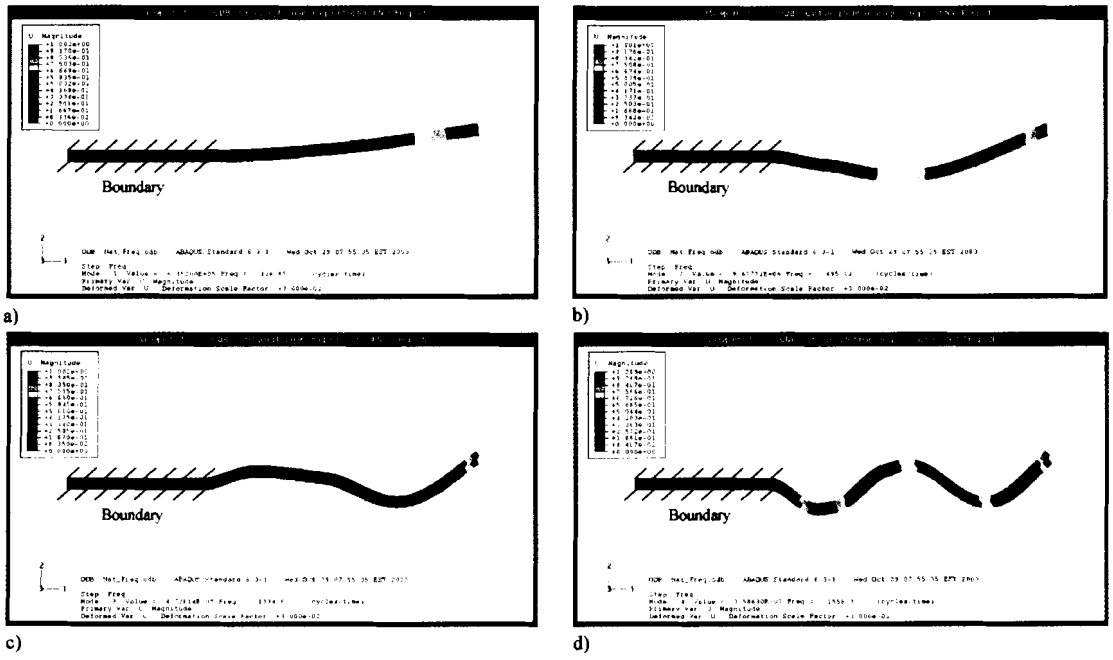

Figure 4.8. The first four natural mode shapes of the cantilever beam using the finite element method

The frequency response function of the uncontrolled cantilever beam is compared with experimental results. A harmonic potential of constant magnitude is applied to the piezoelectric actuator P_1, and the ratio of the steady-state tip acceleration to the excitation voltage is plotted as a function of the forcing frequency. The experimental and finite element frequency response functions are shown in Figure 4.9 on the decibel scale.

As can be seen from Figure 4.9, there is good agreement between the experimental and finite element results. The finite element result is very good at predicting the resonance frequencies of the system. In most engineering applications, these are the locations of most interest. The amplitude of the peaks on the frequency response curves of the finite element solution at resonance are larger than the experimental results since the finite element analysis did not include any structural damping. The finite element model yields peaks that tend toward infinity at resonance.

At other frequencies, the two results seem to have discrepancy that increases as the forcing frequency increases. This could be attributed to a number of factors. First, there is no way to confirm that the PZT actuators have the piezoelectric coefficients that are reported from Morgan Electro Ceramics. The experimental characterization of these coefficients is very difficult and beyond the scope of this thesis. If the piezoelectric coefficient e_{35} is less than the reported 12.3 C / m^2, then the structural response will be less for a given excitation voltage. In addition, at higher frequencies the dynamic response of the system is very sensitive to fabrication defects, boundary conditions etc.

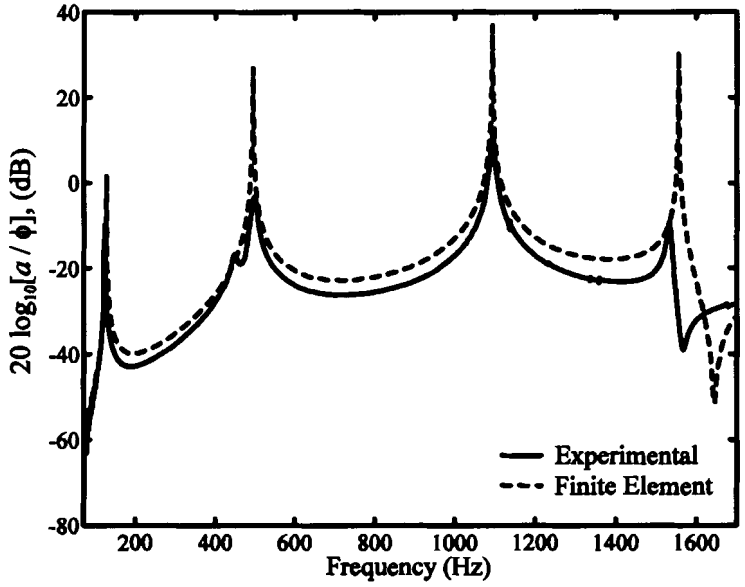

Figure 4.9. The experimental and finite element model comparison of the frequency response function of the cantilever beam (a – tip acceleration; ϕ - potential)

4.4.2. Active Damping of the Cantilever Beam in the Frequency Domain Using PPF Control

The effect of using PPF control to actively suppress vibration of a cantilever beam is first examined in the frequency domain. The frequency response function gives an

indication of the damping present in the system; therefore, it is logical to examine the effectiveness of the PPF controller using the frequency response of the system. A parametric study is performed to quantify the effect of PPF controller parameters on system damping.

In the first part of the study, the fundamental frequency of the cantilever beam is targeted for suppression. The PZT-5A shear actuator P_1 acts as the disturbance source, and shear actuator P_2 is used for active vibration suppression. As before, the ratio of the tip acceleration and the disturbance potential is plotted as a function of the disturbance frequency. The strain sensor near the root of the beam acts as the forcing function to the PPF compensator. The base compensator utilized in the parametric study consisted of a controller frequency ω_c that is 1.3 times the fundamental frequency (ω = 123.0625 Hz), a compensator damping parameter ζ_c equal to 0.05 and a scalar gain g of 17.0×10^{-6} s^2 V. First, the effect of the controller frequency ω_c parameter on system damping is investigated while keeping the compensator damping and scalar gain constant. Four different controller frequencies of ω, 1.1ω, 1.3ω and 1.45ω are studied. Next, the compensator frequency ω_c and scalar gain g are kept constant, and four different controller damping parameter ζ_c of 0.05, 0.15, 0.35 and 0.5 are tried. These value span the range of the recommended values by other researchers (refer to Section 1.2.3). Last, the frequency response curves are computed for different scalar gains g equal to 3.4×10^{-6} s^2 V, 8.5×10^{-6} s^2 V, 17.0×10^{-6} s^2 V and 34.0×10^{-6} s^2 V. The frequency response curves are shown in Figure 4.10.

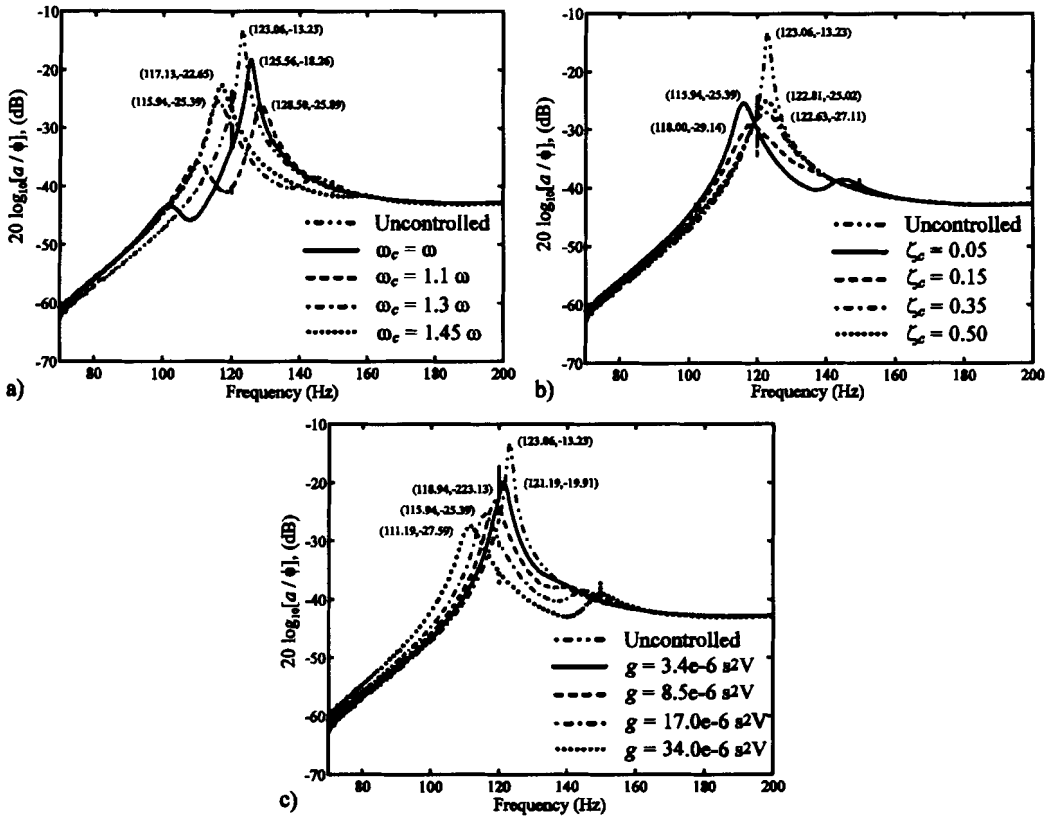

Figure 4.10. An experimental parametric study using a PPF controller to actively suppress the fundamental frequency of the beam (a – tip acceleration; ϕ - potential)

As can be seen from Figure 4.10(a), the compensator frequencies ω_c equal to 1.1ω and 1.3ω produce peak responses of –25.89 dB and –25.39 dB, respectively. This is a significant reduction in peak response of –13.23 dB in the absence of active feedback controls. It is interesting to note, however, that the peak response occur at 128.5 Hz and 115.94 Hz when ω_c is set equal to 1.1ω and 1.3ω, respectively. This is a significant shift in system resonance frequency as a result of the compensator. The PPF compensator when the controller frequency ω_c is equal to the fundamental frequency is not as effective since the peak response is –18.26 dB.

Figure 4.10(b) reveals that the optimum compensator damping parameter is 0.15, resulting in a peak response of –29.14 dB. The peak shifts to the right as the controller damping parameter is increased. The peak response occur at 118.0 Hz and 122.81 Hz for controller damping parameters of ζ_c = 0.05 and 0.5, respectively. The influence of the compensator scalar gain g shown in Figure 4.10(c) is as expected. System damping increases as the gain is increased. The peak response reduces from –13.23 dB without feedback control to –27.59 dB for $g = 34.0\times10^{-6}$ s^2 V.

Next, the experimental results from the parametric study in Figure 4.10 are compared to that of the finite element solution using the same PPF controller parameters. The finite element and experimental frequency response curves are shown in Figure 4.11(a) for PPF compensator frequency $\omega_c = 1.1\omega$, damping ratio $\zeta_c = 0.05$ and gain $g = 17.0\times10^{-6}$ s^2 V. Figure 4.11(b) contains results for $\omega_c = 1.3\omega$, $\zeta_c = 0.35$ and $g = 17.0\times10^{-6}$ s^2 V. An excitation potential of 120 V is applied to the shear actuator P_1 in the finite element model.

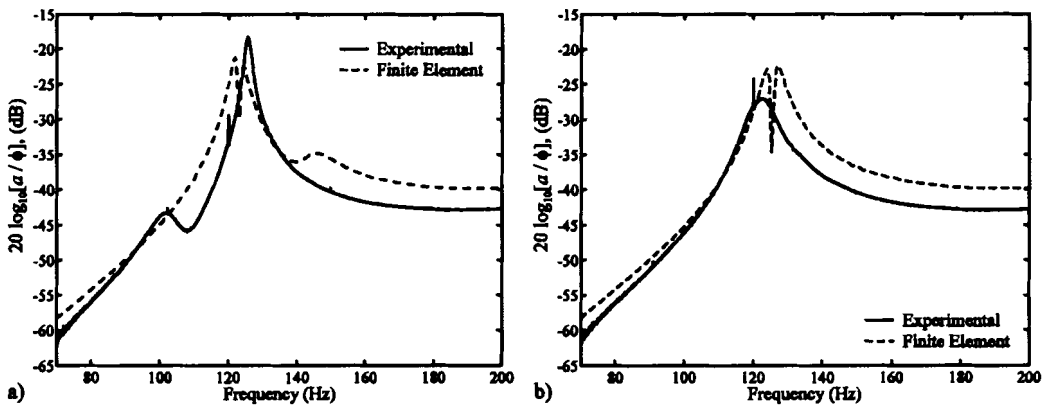

Figure 4.11. The experimental and finite element comparison of the active feedback control of the cantilever beam using PPF control (a – tip acceleration; ϕ - potential)

As can be seen from Figure 4.11, the experimental and finite element results compare reasonably well. Although the peaks occur at slightly different frequencies, it should be remembered that the uncontrolled natural frequencies were off by approximately 4 Hz. It should be noted that the uncontrolled beam does not posses any damping in the finite element model; therefore, the finite amplitude at resonance is a results of the PPF compensator. A careful examination of Figure 4.10 reveals a sharp decrease in tip acceleration when the forcing frequency nears the target frequency. This phenomenon was not observed in the experimentally obtained frequency response curves. This may be attributed to the lack of structural damping in our finite element model.

Next, the effectiveness of the PPF compensator in suppressing the second mode of vibration is examined experimentally. A parametric study of the effect of PPF compensator frequency and damping ratio is performed. The base compensator has a compensator frequency $\omega_c = 1.3\omega$, damping parameter $\zeta_c = 0.3$ and scalar gain $g = 15.3 \times 10^{-6}$ s^2 V, where $\omega = 495.71$ Hz. The results of the parametric study for different compensator frequencies are given in Figure 4.12(a). The response reduces from -3.69 dB to -11.96 dB when the compensator frequency is 1.3 times the second natural frequency. The compensator frequency that produces the least amount of suppression is when it is equal to the second natural frequency. This produces a reduction in peak response of only -8.72 dB. The compensator damping parameter ζ_c that produces the greatest reduction in peak response is the chosen base compensator value of $\zeta_c = 0.30$, as shown in Figure 4.12(b).

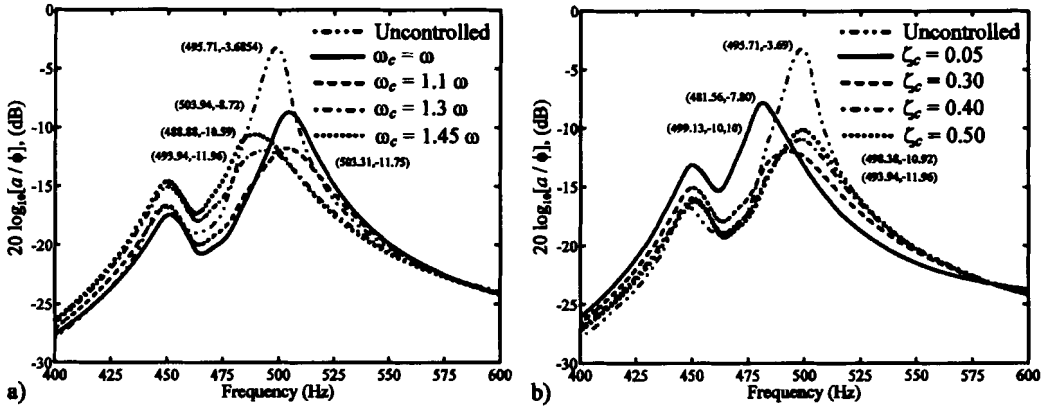

Figure 4.12. An experimental parametric study using a PPF controller to actively suppress the second mode of vibration of the beam (a – tip acceleration; ϕ - potential)

In the next investigation, we attempt to use a single actuator to suppress the first two modes of vibration simultaneously. This is accomplished by placing two compensators in parallel in the Simulink PPF block diagram as shown in Figure 4.3. The sum of the outputs of two PPF compensators, with parameters equal to the values that exhibited the most reduction in peak response for each individual mode in the previous two parametric studies, is amplified and applied to the shear actuator P_2. The PPF compensator used to target the fundamental mode has a compensator frequency $\omega_c = 1.1\omega$, compensator damping $\zeta_c = 0.15$ and a scalar gain $g = 17.0 \times 10^{-6}$ s^2 V. The other PPF compensator targets the second natural frequency and it has a compensator frequency $\omega_c = 1.3\omega$, compensator damping $\zeta_c = 0.30$ and a scalar gain $g = 15.3 \times 10^{-7}$ s^2 V. The experimental and finite element frequency response functions from 70 Hz to 600 Hz are shown in Figure 4.13. There is very good agreement between the finite element and experimental values near the first natural frequency. The peak responses are almost indiscernible. The experimental response at the fundamental frequency is -28.19

dB at a forcing frequency of 113.13 Hz, which is only slightly more than that when a single controller is used to target the fundamental mode.

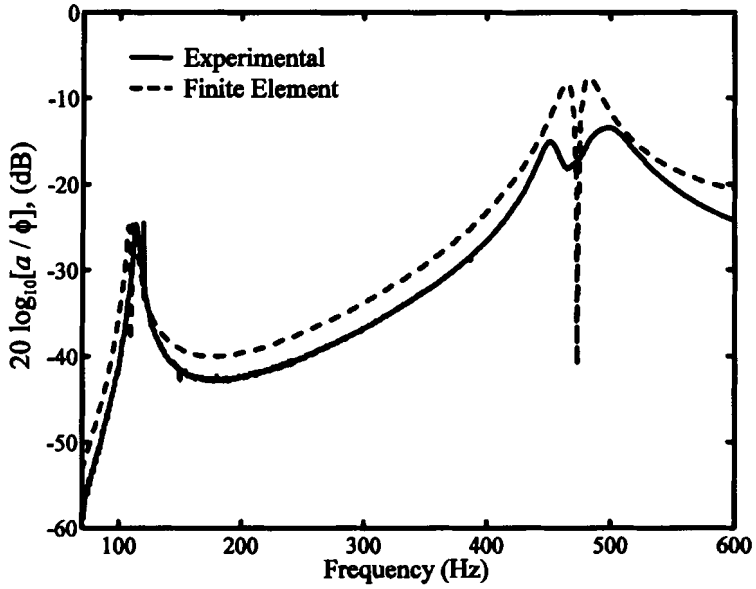

Figure 4.13. Experimental and finite element active control of two distinct modes using a single actuator (a – tip acceleration; ϕ - potential)

The frequency response functions near the second natural frequency do not compare as well as that at the fundamental frequency. The finite element solution, for the most part, produces larger amplitude for a given frequency. At the target frequency, however, the response reduces very rapidly. This behavior is seen in the finite element active feedback control of the first mode as well. Perhaps the numerical model may not exhibit this behavior if damping were included.

The experimental peak response in Figure 4.13 is -16.41 dB at 498.75 Hz. It is interesting that this response is less than that when the second mode is targeted by a single PPF compensator. As can be seen from Figure 4.12, the peak response from the suppression of the beam using a single compensator is -11.96 dB at 493.94 Hz. The peak response not only decreases, but the peak has shifted to the right as a result of the

addition of a second compensator that targets the first natural frequency. This fact makes sense once Equation (2.35) is examined. As the forcing frequency deviates from the target frequency, the real portion of the denominator of Equation (2.35) becomes larger. This results in less potential applied to control the system. Since the fundamental frequency lies to the left on the frequency spectrum, relative to the second mode, the compensator targeting mode 1 applies more potential to the frequencies to the left of the second resonance peak. Augmenting this phenomenon with the response from the compensator targeting mode 2 produces a response that has shifted to the right with smaller amplitude.

4.4.3. Active Damping of the Cantilever Beam in the Frequency Domain Using SRF Control

This portion of the study focuses on the active feedback control using SRF control and to analyze the efficacy of an SRF controller for active vibration suppression. First, a parametric study, similar to that depicted in Figure 4.12, is performed to understand how the SRF control parameters influence the structural response. The base compensator utilized in the study consists of a compensator frequency $\omega_c = 1.3\omega$, compensator damping ratio $\zeta_c = 0.05$ and scalar gain $G = 17.0 \times 10^{-9}$ s^3 V. The Simulink block diagram for SRF control is given in Appendix C. The results of the SRF parametric study can be found in Figure 4.14. A harmonic disturbance is applied using shear actuator P_1, and active vibration suppression is achieved using actuator P_2.

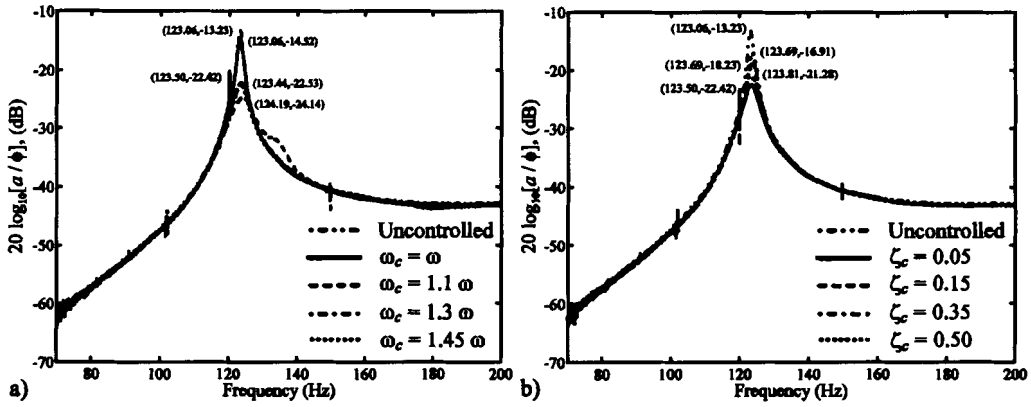

Figure 4.14. An experimental parametric study on the influence of SRF control parameters on the response of the cantilever beam (a – tip acceleration; ϕ - potential)

It is found that the compensator produces the largest structural damping when the controller frequency is 1.1 times the fundamental frequency. The corresponding maximum response is -24.14 dB. It is noted that unlike a PPF compensator, the frequency location of the peak structural response does not change much when an SRF compensator is employed. As the filter damping parameter is decreased, the peak system response also decreases. This response is different from that of the PPF controller where the best choice of controller damping parameter was about 0.15.

A finite element solution with SRF control is obtained for two sets of controller parameters and compared with experimental results. The results of the comparison of the experimental and finite element values are given in Figure 4.15. The first analysis, shown in Figure 4.15(a), has SRF compensator frequency $\omega_c = 1.1\omega$ and controller damping parameter $\zeta_c = 0.05$. The second analysis, shown in Figure 4.15(b), has SRF compensator frequency $\omega_c = 1.3\omega$ and controller damping parameter $\zeta_c = 0.15$. The scalar gain $G=17.0\times10^{-9}$ s^3 V for both analyses.

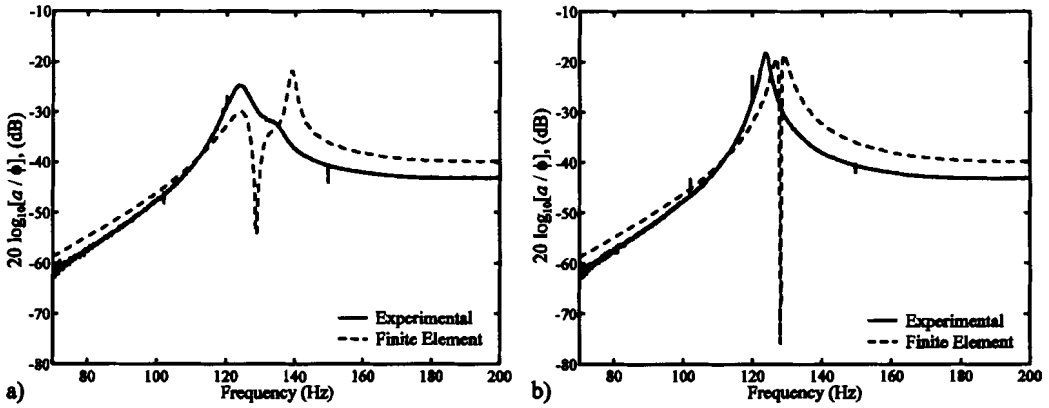

Figure 4.15. An experimental and finite element comparison of using SRF control to suppress the first natural mode of the beam (a – tip acceleration; ϕ - potential)

As can be seen from Figure 4.15(a), there are qualitative and quantitative differences between the experimental and finite element results. However, the peak responses compare reasonably well. The comparison is much better for Figure 4.15(b). The frequencies where the peaks occur are different. Interestingly, the sharp decrease in structural response at the target frequency of the finite element model is also seen when SRF control is utilized. Therefore, this phenomenon is not unique to the finite element implementation of PPF control.

4.4.4. Experimental and Finite Element Active Damping of the Cantilever Beam in the Time Domain Using PPF Control

The active feedback control of the cantilever beam in the time domain is the subject of the rest of the study. So far, the effect of the PPF controller was examined in the frequency domain. It is important to analyze the response of the system in the time domain as well. The beam is harmonically excited at the fundamental frequency using the proof-mass actuator (piezostack and steel block) depicted in Section 4.3. The addition of the proof-mass actuator causes the experimental fundamental frequency to

drop to 75.66 Hz. The beam is first allowed to reach steady-state vibration due to the harmonic excitation by the proof-mass actuator. Starting at time t = 1 s, shear actuator P_1 is used to suppress the vibration using a PPF controller. At time t = 2 s, shear actuator P_2 is also switched on provide additional vibration suppression. The corresponding Simulink block diagram is given in Appendix C. The PPF compensator utilized for this portion of the study has of a compensator frequency ω_c equal to 1.3 times the fundamental frequency of 75.66 Hz and filter damping parameter ζ_c of 0.3. The scalar gain for both shear actuators P_1 and P_2 is 17.0×10^{-5} s^2 V. A sampling rate of 390.6 μs / sample and record length of 8192 were used for data acquisition system. The result of the steady-state active feedback control study can be found in Figure 4.16.

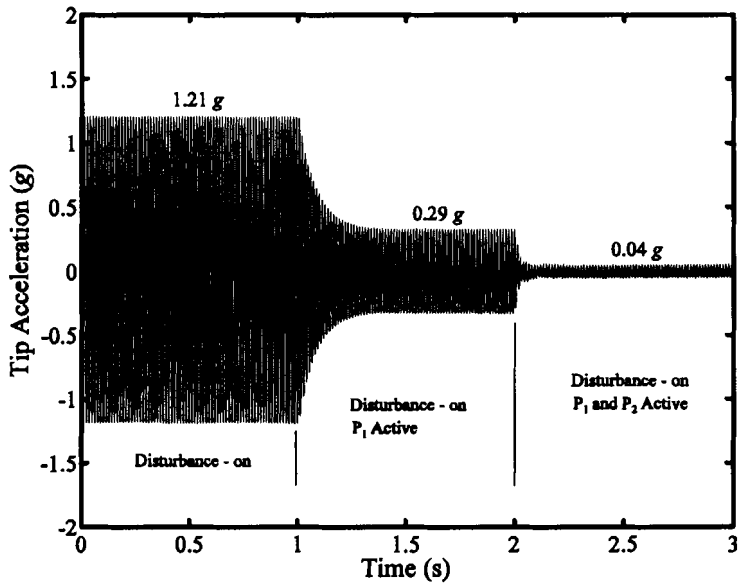

Figure 4.16. The steady-state response of the cantilever beam subjected to PPF control using both shear actuators

Figure 4.16 shows the shear actuators are very effective in reducing the amplitude of vibration of the cantilever beam. When only actuator P_1 is employed, the tip acceleration reduces from approximately 1.21g to 0.29g. This is a significant reduction

in tip acceleration. The tip acceleration reduces even further to 0.04g when both P_1 and P_2 are utilized for vibration suppression. This represents a reduction in amplitude of 96.9 %.

In the next portion of the study, the settling time of the cantilever beam is experimentally determined. The beam is harmonically excited using the proof-mass actuator until it reaches steady-state. The excitation is then stopped and the vibration is allowed to decay without feedback control. The experiment is repeated again except this time the PPF controller is switched on using both shear actuators as soon as the excitation is stopped.

The excitation is precisely controlled in both experiments using Simulink and dSPACE. The same PPF controller utilized previously for the transient experiment is also used in this portion of the study. The results between the uncontrolled and PPF controlled transient responses of the cantilever beam are shown in Figure 4.17.

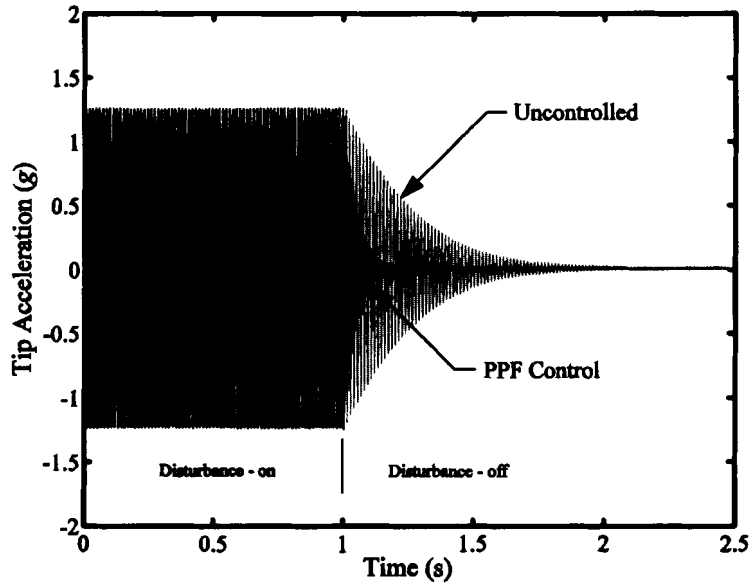

Figure 4.17. Settling time comparison between the uncontrolled and actively controlled cantilever beam

As can be seen from Figure 4.17, the settling time for the actively controlled cantilever beam is dramatically less than that of the uncontrolled structural response. We define the settling time as the time after which the amplitude if vibration is always less than 2% of the steady-state response. It is found that the settling time of the uncontrolled structural response is nearly 1.08 s. When the shear actuators are used for vibration suppression, the settling time is only 0.23 s. This represents a reduction in settling time of 78.7 %.

Lastly, the PPF control is examined using the finite element method and compared to experimental values. The cantilever beam is excited by the proof-mass actuator for 0.1 s and then allowed to decay naturally. The process is repeated again except this time the PPF controller is activated after excitation. The proof-mass actuator is excited with 15.0 V of potential. The PPF controller utilizes both shear actuators and contains the same parameters as for the previous two studies in this section. Again, the excitation to the proof-mass actuator is precisely controlled using Simulink and dSPACE. The experimental and finite element vibration damping comparisons can be found in Figures 4.18(a) and 4.18(b), respectively.

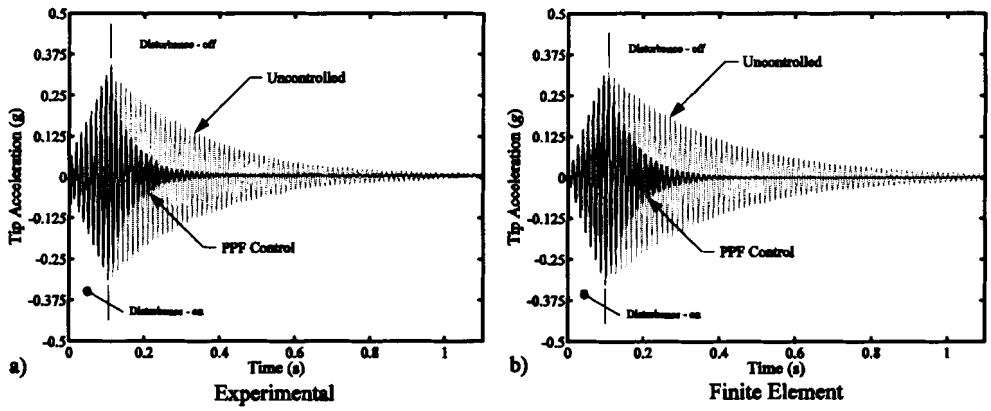

Figure 4.18. Experimental and finite element comparison of the settling time of the cantilever beam

As can be seen from Figure 4.18(b), the finite element model does a good job at predicting the settling time of the system with and without controls. The settling time is defined as the time after which the amplitude if vibration is always less than 2% of the peak response of the beam. The experimental settling time shifts from approximately 0.90 s to 0.272 s with the activation of the PPF controller. This is a reduction of 69.8 % in settling time. The finite element model predicts that the settling time changes from approximately 1.0 s to 0.267 s after the PPF controller is activated. The predicted settling time is reduced by 73.3 %.

Chapter 5

CONCLUSIONS AND RECOMMENDATIONS FOR FUTURE WORK

This chapter summarizes the results of this thesis and the direction of future work. In the first section, the exact analysis and vibration suppression of laminated plates and shells with embedded piezoelectric shear actuators is discussed. Next, the experimental and finite element investigation of the active vibration suppression of a sandwich cantilever beam is summarized. The second section of this chapter details the unanswered question from this thesis and recommendations for future research.

5.1. Summary

Utilization of the piezoelectric shear coefficient for the purpose of active vibration suppression of smart structures was the topic of this thesis. A through investigation of the literature showed that, although the shear-mode of piezoelectric materials, in terms of sensing, has been used in accelerometers since the 1960's, it has been only recently suggested that they be used in smart structures. Prior analytical and numerical research suggests that piezoelectric shear actuators and sensors may be better suited for smart structures applications than the traditional thickness-poled extension actuators/sensors. It is important that the interaction between the shear actuator and host structure be well understood using theoretical and experimental means in order to use them effectively in practical applications.

In the second chapter of this thesis an exact analytical solution to the vibration and active damping of a laminated composite plate with embedded piezoelectric shear actuators is developed. Suitable displacement and electric potential functions are assumed that identically satisfy the simply supported boundary conditions, which reduce the equation of motion and charge equation of electrostatics to a set of coupled ordinary differential equations of the thickness coordinate x_3. A power series method is used to solve the system of differential equations. PPF and velocity control laws are implemented into a steady-state forced vibration analysis. The natural frequencies, mode shapes and through-thickness profile plots of displacement, potential and stress are given for various laminate configurations. Also, numerical values of displacements, stresses and potential are presented. System identification is important to any control scheme, and these results are utilized in a parametric study of PPF and velocity control parameters on the active damping of the fundamental frequency. Results indicate that piezoelectric shear actuators are effective for the active damping of laminated composite plates. The active control of the first thickness mode is also accomplished.

The third chapter details static deformation, vibration and active damping analyses of a laminated cylindrical shell with embedded piezoelectric shear actuators. Suitable functions for the displacements and electric potential are assumed that exactly satisfy the boundary conditions at the simply supported edges. The assumed form of displacements and electric potential reduce the equations of motion and charge equation of electrostatics to a set coupled of ordinary differential equations of the radial coordinate r, which can be solved using the Frobenius method. As with Chapter 2, a PPF control law is implemented into a steady-state forced vibration analysis. Static deformation

thickness plots of potential, circumferential displacement and stresses are presented. The natural frequencies, mode shapes and through-thickness plots of displacements, potential and stresses are also given. A parametric study on the effect of PPF controller parameters is presented, and it is found that the piezoelectric shear coefficient is effective in suppressing the fundamental mode of vibration. Also, the first thickness mode is actively suppressed using a PPF control law. These results suggest that piezoelectric shear actuators are a viable option when developing active vibration suppression systems for cylindrical composite shells.

The experimental active control of a sandwich cantilever beam is the focus of Chapter 4. The beam consisted of two aluminum face sheets, a foam core and two piezoelectric shear actuators. PPF and SRF control laws are utilized for the vibration suppression. Replication of the experimental results using theoretical means is a goal of this portion of the study. The exact analyses developed in the previous chapters are not applicable to this problem; therefore, a finite element model is developed to model the experimental behavior of the hybrid beam. Parametric studies in the frequency domain of the PPF and SRF control law parameters are performed using experimental and numerical means. The active control in the frequency domain of two distinct modes using a single actuator is performed numerically and experimentally. The experimental behavior of the sandwich cantilever beam shows significant reduction in tip acceleration as a result of both PPF and SRF control. The finite element model is able to predict the experimental behavior of sandwich cantilever beam in the frequency domain reasonably well. Several tests were conducted in the time domain to examine how the PPF controller affected the sandwich beam response. It was found that there is significant reduction in amplitude of

the tip acceleration as a result of the active feedback control. A finite element model of the PPF control in the time domain compares well with the observed experimental response.

5.2. Recommendations for Future Work

The research contained in this thesis has shown great potential for the use of piezoelectric shear actuators and sensors for active vibration suppression applications. The exact solutions to the analysis and active vibration suppression of laminated plates and shells with embedded piezoelectric shear actuators provide a strong foundation from which approximate plate and shell theories can be developed for design engineers.

Other researchers have indicated that piezoelectric shear actuators perform better than the tradition extensional actuators in certain configurations (if the structure is stiff, if the actuator is fairly thick compared to the length, etc.). A detailed experimental comparison between the two movement mechanisms is needed. This will allow for an informed decision when designing an optimum active feedback control system using piezoelectric materials.

PPF and velocity feedback control laws are the only algorithms utilized in this analysis. The use of other control laws could lead to active vibration suppression of the structure using less control effort (less power). An active vibration suppression system that utilizes less control effort is advantageous because it will use less energy and require smaller voltage amplifiers.

Experimental studies on the optimal actuator placement are needed. Previous researchers have concluded that active element placement for a piezoelectric shear actuator is not as critical as that for extension actuators. An experimental investigation

into this claim is warranted because flexibility in actuator placement is advantageous if certain inertial requirements are needed of the structure.

Another very important aspect is the development of techniques to manufacture piezoelectric shear actuators. Polarization of a shear actuator is not as straightforward as that for the traditional extensional piezoelectric element. A fast, low-cost manufacturing method must be developed before widespread use of the piezoelectric shear actuator is adopted.

REFERENCES

Agrawal, B.N., and Treanor, K.E., 1999, Shape control of a beam using piezoelectric actuators, *Smart Materials and Structures* 8: 729-740.

Aldraihem, O. J., and Khdeir, A.A., 2003, Exact deflection solutions of beams with shear piezoelectric actuators, *International Journal of Solids and Structures* 40: 1-12.

Bailey, T., and Hubbard, J.E., Jr., 1985, Distributed piezoelectric polymer active vibration control of a cantilever beam, *AIAA Journal of Guidance, Control and Dynamics* 8: 605-611.

Baltek Corporation, n.d., Airex R82, *Baltek Product Data Sheet*, < http://www.baltek.com/data/pdfs/products/BEMSPDSairexr82.pdf> (04 November 2003).

Batra, R.C., and Liang, X.Q., 1997, Finite dynamic deformations of smart structures, *Computational Mechanics* 20: 427-438.

Batra, R.C., Liang, X.Q., and Yang, J.S., 1996, The vibration of a simply supported rectangular elastic plate due to piezoelectric actuators, *International Journal of Solids and Structures* 33: 1597-1618.

Benjeddou, A., 2000, Advances in hybrid active-passive vibration and noise control via piezoelectric and viscoelastic constrained layer treatments, *Journal of Vibration and Control* 7: 565-602.

Benjeddou, A., and Deü, J.-F., 2001a, Piezoelectric transverse shear actuation and sensing of plates, Part 1: A three-dimensional mixed state space formulation, *Journal of Intelligent Material Systems and Structures* 12: 435-449.

Benjeddou, A., and Deü, J.-F., 2001b, Piezoelectric transverse shear actuation and sensing of plates, Part 2: Application and analysis, *Journal of Intelligent Material Systems and Structures* 12: 451-467.

Benjeddou, A., and Deü, J.-F., 2002, A two-dimensional closed-form solution for the free-vibration analysis of piezoelectric sandwich plates, *International Journal of Solids and Structures* 39: 1463-1486.

Benjeddou, A., Gorge, V., and Ohayon, R., 2001a, Use of piezoelectric shear response in adaptive sandwich shells of revolution – Part 1: Theoretical formulation, *Journal of Intelligent Material Systems and Structures* 12: 235-245.

Benjeddou, A., Gorge, V., and Ohayon, R., 2001b, Use of piezoelectric shear response in adaptive sandwich shells of revolution – Part 2: Finite element implementation, *Journal of Intelligent Material Systems and Structures* 12: 247-257.

Benjeddou, A., Trindade, M.A., and Ohayon, R., 1999, New shear actuated smart structure beam finite element, *AIAA Journal* 37(3): 378-383.

Bent, A., 1997, Active fiber composites for structural actuation, Ph.D. dissertation, MIT.

Berlincourt, D., and Krueger, H. H. A., n.d., Properties of morgan electroceramic ceramics, Revised by C. Near, <http://www.morganelectroceramics.com/pdfs/tp226.pdf> (05 August 2002).

Bisegna, P., and Maceri, F., 1996, An exact three-dimensional solution for simply supported rectangular piezoelectric plates, *Journal of Applied Mechanics* 63: 628-638.

Bradley, W., Jr., and Bergman, G.B., 1963, Annular Accelerometer, US Patent 3,104,334.

Chen, C.-Q., and Shen, Y.-P., 1998, Three-dimensional analysis for the free vibration of finite-length orthotropic circular cylindrical panel in cylindrical bending, *Journal of Vibration of Acoustics* 120: 194-198.

Chen, C.-Q., Shen, Y.-P., and Wang, X.-M., 1996, Exact solution of orthotropic cylindrical shell with piezoelectric layers under cylindrical bending, *International Journal of Solids and Structures* 33: 4481-4494.

Clark, R.L., and Fuller, C.R., 1992, Experiments on active control of structurally radiated sound using multiple piezoelectric actuators, *The Journal of Acoustical Society of America* 91: 3313-3320.

Clephas, B., 1999, Piezoelectric actuators, In *Adaptronics and Smart Structures: Basics, Materials, Design, and Application*, Edited by Hartmut Janocha, Berlin; New York: Springer.

Crawley, E.F., and Anderson, E.H., 1990, Detailed models of piezoceramic actuation of beams, *Journal of Intelligent Material Systems and Structures* 1: 4-25.

Crawley, E.F., and de Luis, J., 1987, Use of piezoelectric actuators as elements of intelligent structures, *AIAA Journal* 25: 1373-1385.

Culshaw, B., 1996, Signal processing and control for smart structures, *Smart Structures and Materials*, Chapter 5, Boston: Artech House.

DeGuilio, A.P., 2000, A comprehensive experimental evaluation of actively controlled piezoceramics with positive position feedback for structural damping, Master's thesis, Virginia Polytechnic Institute and State University.

Dosch, J.J., Inman, D.J., and Garcia, E., 1992, Self-sensing piezoelectric actuator for collocated control, *Journal of Intelligent Material Systems and Structures* 3(1): 166-185.

Dumir, P.C., Dube, G.P., and Kapuria, S., 1997, Exact piezoelastic solution of simply-supported orthotropic circular cylindrical panel in cylindrical bending, *International Journal of Solids and Structures* 34(6): 685-702.

Fagan, G.T., 1993, An experimental investigation into active damage control using positive position feedback for AVC, Master's thesis, Virginia Polytechnic Institute and State University.

Fanson, J.L., and Caughey, T.K., 1990, Positive position feedback control for large space structures, *AIAA Journal* 28(4): 717-724.

Friswell, M.I., and Inman, D.J., 1999, The relationship between positive position feedback and output feedback controllers, *Smart Materials and Structures* 8: 285-291.

Fuller, C.R., Elliott, S.J., and Nelson, P.A., 1996, *Active Control of Vibration*, San Diego: Academic Press.

Garcia, E., Dosch, J., and Inman, D.J., 1992, The application of smart structures to the vibration suppression problem, *Journal of Intelligent Material Systems and Structures* 3: 659-667.

Glazounov, A.E., and Zhang, Q.M., 1998, Piezoelectric actuator generating torsional displacement from piezoelectric d_{15} shear response, *Applied Physics Letters* 72 (20): 2526-2528.

Goh, C.J., and Caughey, T.K., 1985, On the stability problem caused by finite actuator dynamics in the collocated control of large space structures, *International Journal of Control* 41(3): 787-802.

Hagood, N.W., and von Flotow, A., 1991, Damping of structural vibrations with piezoelectric materials and passive electrical networks, *Journal of Sound and Vibrations* 142(2): 243-268.

Han, J.-H., and Lee, I., 1997, Active damping enhancements of composite plates with electrode designed piezoelectric materials, *Journal of Intelligent Material Systems and Structures* 8(3): 294-259.

Hegewald, T., 2000, Vibration suppression using smart materials in the presence of temperature changes, Master's thesis, Virginia Polytechnic Institute and State University.

Heyliger, P., 1994, Static behavior of laminated elastic/piezoelectric plates, *AIAA Journal* 32: 2481-2484.

Heyliger, P., 1997, Exact solutions for simply supported laminated piezoelectric plates, *Journal of Applied Mechanics* 64: 628-638.

Heyliger, P., and Brooks, S., 1995, Free-vibration of piezoelectric laminates in cylindrical bending, *International Journal of Solids and Structures* 32: 2945-2960.

Heyliger, P., and Brooks, S., 1996, Exact solutions for laminated piezoelectric plates in cylindrical bending, *Journal of Applied Mechanics* 63: 903-910.

Heyliger, P., and Saravanos, D.A., 1995, Exact free-vibration analysis of laminated plates with embedded piezoelectric layers, *Journal of the Acoustical Society of America* 98: 1547-1557.

Hibbitt, Karlsson & Sorensen, Inc., 2002, *ABAQUS Users Manual*, Version 6.3.

Hsu, C.Y., Lin, C.C., and Gaul, L., 1998, Vibration and sound radiation controls of beams using layered modal sensors and actuators, *Smart Materials and Structures* 7: 446-455.

Huang, J.H., and Wu, T.L., 1996, Analysis of hybrid multilayered piezoelectric plates, *International Journal of Engineering Science* 34: 171-181.

Kerwin, E.M., Jr., 1959, Damping of flexural waves by a constrained viscoelastic layer, *Journal of the Acoustical Society of America* 31(7): 952-962.

Khdeir, A.A., and Aldraihem, O.J., 2001, Deflection analysis of beams with extension and shear piezoelectric patches using discontinuity functions, *Smart Materials and Structures* 10: 212-220.

Koconis, D.B., Kollar, L.P., and Springer, G.S., 1994, Shape control of composite plates and shells with embedded actuators. II. Desired shape specified, *Journal of Composite Materials* 28: 459-482.

Kreyszig, E., 1999, *Advanced Engineering Mathematics*, Eighth Edition, New York: John Wiley & Sons, Inc.

Lam, K.Y., Peng, X.Q., Liu, G.R., and Reddy, J.N., 1997, Finite-element model for piezoelectric composite laminates, *Smart Materials and Structures* 6(5): 583-591.

Lee, C.K., 1990, Theory of laminated piezoelectric plates for the design of distributed sensors/actuators. Part 1: governing equations and reciprocal relationships, *Journal of the Acoustic Society of America* 87: 1144-1158.

Lee, J.S., and Jiang, L.Z., 1996, Exact electroelastic analysis of piezoelectric laminae via state space approach, *International Journal of Solids and Structures* 33: 977-990.

Lee, Y.S., Elliott, S.J., and Gardonio, P., 2001, Distributed four-layer PVDF actuator/sensor arrangement for the control of beam motion, *Proceedings of SPIE – The International Society for Optical Engineering* 4326: 284-294.

Lim, Y.-H., Varadan, V.V., and Varadan, V.K., 1999, Closed loop finite element modeling of active structural damping in the time domain, *Smart Materials and Structures* 8(3): 390-400.

Lim, Y.-H., Varadan, V.V., and Varadan, V.K., 1997, Closed loop finite element modeling of active structural damping in the frequency domain, *Smart Materials and Structures* 6(2): 161-168.

Meyer, J.L., Harrington, W.B., Agrawal, B.N., and Song, G., 1998, Vibration suppression of a spacecraft flexible appendage using smart materials, *Smart Materials and Structures* 7(1): 95-104.

Mitchell, J.A., and Reddy, J.N., 1995, A refined hybrid plate theory for composite laminates with piezoelectric laminae, *International Journal of Solids and Structures* 32: 2345-2367.

Mueller, V., and Zhang, Q.M., 1998, Shear response of lead zirconate titanate piezoceramics, *Journal of Applied Physics* 83 (7): 3754-3761.

Newman, S.M., 1992, Active damping control of a flexible space structure using piezoelectric sensors and actuators, Master's thesis, U.S. Naval Postgraduate School.

Nye, J. F., 1957, Piezoelectricity Third-Rank Tensors, In *Physical Properties of Crystals: Their Representation by Tensors and Matices*, Oxford: Clarendon Press.

Press, W.H., Teukolsky, S.A., Vetterling, W.T., and Flannery, B.P., 1992, *Numerical Recipes in C*, Cambridge: Cambridge University Press.

Raja, S., Prathap, G., and Sinha, P.K., 2002, Active vibration control composite sandwich beams with piezoelectric extension-bending and shear actuators, *Smart Materials and Structures* 11: 63-71.

Rao, S.S., 1995, *Mechanical Vibrations*, 3d ed., Reading: Addison-Wesley.

Ray, M.C., Rao, K.M., and Samanta, B., 1993, Exact solution for static analysis of intelligent structures under cylindrical bending, *Computers and Structures* 47: 1031-1042.

Ruggiero, E.J., 2002, Active dynamic analysis and vibration control of gossamer structures using smart materials, Master's thesis, Virginia Polytechnic Institute and State University.

Song, G., Qiao, P.Z., and Binienda, W.K., 2001, Active vibration damping of a composite beam using smart sensors and actuators, *Collection of Technical Papers - AIAA/ASME/ASCE/AHS/ASC Structures, Structural Dynamics, and Materials Conference* 5: 3347-3357.

Sun, C.T., and Zhang, X.D., 1995, Use of thickness-shear mode in adaptive sandwich structures, *Smart Materials and Structures* 4: 202-206.

Trindade, M.A., Benjeddou, A., and Ohayon, R., 2000, Parametric analysis of the vibration control of sandwich beams through shear-based piezoelectric actuation, *Journal of Intelligent Material Systems and Structures* 10(5): 377-385.

Trindade, M.A., Benjeddou, A., and Ohayon, R., 2001a, Finite element modeling of hybrid active-passive vibration damping of multilayer piezoelectric sandwich beams – part I: Formulation, *International Journal for Numerical Methods in Engineering* 51: 835-854.

Trindade, M.A., Benjeddou, A., and Ohayon, R., 2001b, Finite element modeling of hybrid active-passive vibration damping of multilayer piezoelectric sandwich beams – part II: System analysis, *International Journal for Numerical Methods in Engineering* 51: 855-864.

Vel, S.S., and Batra, R.C., 2000a, Cylindrical bending of laminated plates with distributed and segmented piezoelectric actuators/sensors, *AIAA Journal* 38: 857-867.

Vel, S.S., and Batra, R.C., 2000b, Three-dimensional analytical solutions for hybrid multilayered piezoelectric plates, *Journal of Applied Mechanics* 67: 558-567.

Vel, S.S., and Batra, R.C., 2001a, Analysis of piezoelectric bimorphs and plates with segmented actuators, *Thin-walled Structures* 39: 23-44.

Vel, S.S., and Batra, R.C., 2001b, Exact solution for the cylindrical bending of laminated plates with embedded piezoelectric shear actuators, *Smart Materials and Structures* 10: 240-251.

Vel, S.S., and Batra, R.C., 2001c, Exact solution for rectangular sandwich plates with embedded piezoelectric shear actuators, *AIAA Journal* 39(7): 1363-1373.

Yang, J.S., Batra, R.C., and Liang, X.Q., 1994, The cylindrical bending vibration of a laminated elastic plate due to piezoelectric actuators, *Smart Materials and Structures* 3: 485-493.

Zhang, X.D., and Sun, C.T., 1996, Formulation of an adaptive sandwich beam, *Smart Materials and Structures* 5: 814-823.

Zhang, X.D., and Sun, C.T., 1999, Analysis of a sandwich plate containing a piezoelectric core, *Smart Materials and Structures* 8: 31-40.

APPENDICIES

Appendix A

Mathematica Program for the Exact Solution of a Piezoelectric Plate

Exact solution for the cylindrical bending vibration of laminated cylindrical shells with shear actuators

Date: July 16, 2003
Authors: Senthil Vel and Brian Baillargeon
Department of Mechanical Engineering
Univeristy of Maine
Orono, ME 04469

Load Packages

```
Off[General::spell, General::spell1]

<< "F:\\Documents and Settings\\Baillargeon\\My Documents\\Publications\\Vibration of
   Piezoelectric Shear Shells in Cylindrical Bending\\4 Layer Composite\\FortranWrite"
<< Graphics`Graphics`;
<< Graphics`Legend`;
<< Graphics`MultipleListPlot`;
<< Graphics`Arrow`;
<< NumericalMath`SplineFit`;
<< LinearAlgebra`MatrixManipulation`;
(*Usage: FortranWrite["inp_file1.txt", array];*)
```

Program Input

- Number of terms in the series solution

```
Nmax = 40;
```

- Number of layers

```
NL = 4;
```

- Axial mode shape

```
k = 1;
```

- The thickness mode

```
NMode = 1;
```

- The width and the total thickness of laminate

```
L = 25 / 100.0; SR = 10;
H = L / SR;
```

- Constants for the normalization of equations

```
L0 = L;
Sigma0 = 100.0 x 10^9;
Eps0 = 150.0 x 10^-10;
V0 = L0 Sqrt[Sigma0 / Eps0];
e0 = Sigma0 x L0 / V0;
ρ0 = 7750.0;

H = H / L0;
L = L / L0;
```

- Location of the bottom surface, interfaces and top surface for each segment

```
Zk = {-H / 2, -H / 10, H / 10, H / 2};
```

- Elastic properties of the NL laminae

```
C11 = {183.443 x 10^9, 86.856 x 10^9, 183.443 x 10^9} / Sigma0;
C22 = {11.662 x 10^9, 99.201 x 10^9, 11.662 x 10^9} / Sigma0;
C33 = {11.662 x 10^9, 99.201 x 10^9, 11.662 x 10^9} / Sigma0;
C12 = {4.363 x 10^9, 50.778 x 10^9, 4.363 x 10^9} / Sigma0;
C13 = {4.363 x 10^9, 50.778 x 10^9, 4.363 x 10^9} / Sigma0;
C23 = {3.918 x 10^9, 54.016 x 10^9, 3.918 x 10^9} / Sigma0;
C44 = {2.870 x 10^9, 22.593 x 10^9, 2.870 x 10^9} / Sigma0;
C55 = {7.170 x 10^9, 21.1 x 10^9, 7.170 x 10^9} / Sigma0;
C66 = {7.170 x 10^9, 21.1 x 10^9, 7.170 x 10^9} / Sigma0; C16 = {0, 0, 0} / Sigma0;
C26 = {0, 0, 0} / Sigma0;
C36 = {0, 0, 0} / Sigma0;
C45 = {0, 0, 0} / Sigma0;
```

- Density of the NL laminae

```
ρ = {1590, 7750, 1590} / ρ0;
```

- Piezoelectric and electric properties of the NL laminae

```
e11 = {0, 15.118, 0} / e0;
e12 = {0, -7.209, 0} / e0;
e13 = {0, -7.209, 0} / e0;
e16 = {0, 0, 0} / e0;
e21 = {0, 0, 0} / e0;
e22 = {0, 0, 0} / e0;
e23 = {0, 0, 0} / e0;
e26 = {0, 12.322, 0} / e0;
e34 = {0, 0, 0} / e0;
e35 = {0, 12.322, 0} / e0;
e11 = {153 x 10^-10, 150 x 10^-10, 153 x 10^-10} / Eps0;
e12 = {0, 0, 0} / Eps0;
e22 = {153 x 10^-10, 153 x 10^-10, 153 x 10^-10} / Eps0;
e33 = {153 x 10^-10, 153 x 10^-10, 153 x 10^-10} / Eps0;
```

Exact solution

- Given normalized x3, find the lamina that the point belongs to.

```
LayerNum = Function[x3,
   Do[If [(x3 ≥ Zk[[n]]) && (x3 ≤ Zk[[n + 1]]), Return[n]], {n, NL}]];
```

- Parameter p

```
p = k π / L;
```

- Empty table of length NL

```
ET = Table[0, {NL}] ;
```

- Layer thicknesses and midsurface location of each layer

```
Hk = ET; Mk = ET;
For[n = 1, n ≤ NL, n++, {
   Hk[[n]] = Zk[[n + 1]] - Zk[[n]]}];
For[n = 1, n ≤ NL, n++, {
   Mk[[n]] = (Zk[[n + 1]] + Zk[[n]]) / 2}];
```

■ Series solution for the displacements and electric potential

```
u1 = ET; u2 = ET; u3 = ET; ϕ = ET;
ε11 = ET; ε22 = ET; ε33 = ET; ε23 = ET; ε13 = ET; ε12 = ET;
E1 = ET; E2 = ET; E3 = ET;
σ11 = ET; σ22 = ET; σ33 = ET; σ23 = ET; σ13 = ET; σ12 = ET;
D1 = ET; D2 = ET; D3 = ET;


For[n = 1, n ≤ NL, n++, {
  U1series = Sum[U1t[n, β] x3^β, {β, 0, Nmax}] + O[x3]^(Nmax + 1);
  U2series = Sum[U2t[n, β] x3^β, {β, 0, Nmax}] + O[x3]^(Nmax + 1);
  U3series = Sum[U3t[n, β] x3^β, {β, 0, Nmax}] + O[x3]^(Nmax + 1);
  Φseries = Sum[Φt[n, β] x3^β, {β, 0, Nmax}] + O[x3]^(Nmax + 1);

  KMAT = ⎛ C55[[n]]  C45[[n]]     0       e35[[n]] ⎞
         ⎜ C45[[n]]  C44[[n]]     0       e34[[n]] ⎟
         ⎜    0         0     C33[[n]]      0     ⎟
         ⎝ e35[[n]]  e34[[n]]     0      -e33[[n]] ⎠;
```

AMAT =

$$\begin{pmatrix} C11[[n]]\,p^2 - \rho[[n]]\,\omega^2 & C16[[n]]\,p^2 & 0 & e11[[n]]\,p^2 \\ C16[[n]]\,p^2 & C66[[n]]\,p^2 - \rho[[n]]\,\omega^2 & 0 & e16[[n]]\,p^2 \\ 0 & 0 & C55[[n]]\,p^2 - \rho[[n]]\,\omega^2 & 0 \\ e11[[n]]\,p^2 & e16[[n]]\,p^2 & 0 & -e11[[n]]\,p^2 \end{pmatrix};$$

EMAT =

$$\begin{pmatrix} 0 & 0 & -(C13[[n]] + C55[[n]])\,p & 0 \\ 0 & 0 & -(C36[[n]] + C45[[n]])\,p & 0 \\ (C13[[n]] + C55[[n]])\,p & (C36[[n]] + C45[[n]])\,p & 0 & (e13[[n]] + e \\ 0 & 0 & -(e13[[n]] + e35[[n]])\,p & 0 \end{pmatrix};$$

```
  Do[{{U1t[n, β + 2]}, {U2t[n, β + 2]}, {U3t[n, β + 2]}, {Φt[n, β + 2]}} =
    Simplify[1/((β + 2) (β + 1)) Inverse[KMAT].AMAT.{{U1t[n, β]}, {U2t[n, β]},
        {U3t[n, β]}, {Φt[n, β]}} + 1/(β + 2) Inverse[KMAT].EMAT.{{U1t[n, β + 1]},
        {U2t[n, β + 1]}, {U3t[n, β + 1]}, {Φt[n, β + 1]}}], {β, 0, Nmax - 2}];

  u1[[n]] = U1series Cos[p x1];
  u2[[n]] = U2series Cos[p x1];
  u3[[n]] = U3series Sin[p x1];
  ϕ[[n]] = Φseries Cos[p x1];

  ε11[[n]] = ∂x1 u1[[n]];
  ε22[[n]] = 0;
```

```
ε33[[n]] = ∂x3 u3[[n]];
ε23[[n]] = (∂x3 u2[[n]] + ∂x2 u3[[n]]) / 2;
ε13[[n]] = (∂x3 u1[[n]] + ∂x1 u3[[n]]) / 2;
ε12[[n]] = (∂x2 u1[[n]] + ∂x1 u2[[n]]) / 2;
E1[[n]] = -∂x1 ϕ[[n]];
E2[[n]] = -∂x2 ϕ[[n]];
E3[[n]] = -∂x3 ϕ[[n]];
```

$$\begin{pmatrix} \sigma11[[n]] \\ \sigma22[[n]] \\ \sigma33[[n]] \\ \sigma23[[n]] \\ \sigma13[[n]] \\ \sigma12[[n]] \end{pmatrix} = \begin{pmatrix} C11[[n]] & C12[[n]] & C13[[n]] & 0 & 0 & C16[[n]] \\ C12[[n]] & C22[[n]] & C23[[n]] & 0 & 0 & C26[[n]] \\ C13[[n]] & C23[[n]] & C33[[n]] & 0 & 0 & C36[[n]] \\ 0 & 0 & 0 & C44[[n]] & C45[[n]] & 0 \\ 0 & 0 & 0 & C45[[n]] & C55[[n]] & 0 \\ C16[[n]] & C26[[n]] & C36[[n]] & 0 & 0 & C66[[n]] \end{pmatrix} \cdot$$

$$\begin{pmatrix} \varepsilon11[[n]] \\ \varepsilon22[[n]] \\ \varepsilon33[[n]] \\ 2\,\varepsilon23[[n]] \\ 2\,\varepsilon13[[n]] \\ 2\,\varepsilon12[[n]] \end{pmatrix} - \begin{pmatrix} e11[[n]] & e21[[n]] & 0 \\ e12[[n]] & e22[[n]] & 0 \\ e13[[n]] & e23[[n]] & 0 \\ 0 & 0 & e34[[n]] \\ 0 & 0 & e35[[n]] \\ e16[[n]] & e26[[n]] & 0 \end{pmatrix} \cdot \begin{pmatrix} E1[[n]] \\ E2[[n]] \\ E3[[n]] \end{pmatrix};$$

$$\begin{pmatrix} D1[[n]] \\ D2[[n]] \\ D3[[n]] \end{pmatrix} = \begin{pmatrix} e11[[n]] & e12[[n]] & e13[[n]] & 0 & 0 & e16[[n]] \\ e21[[n]] & e22[[n]] & e23[[n]] & 0 & 0 & e26[[n]] \\ 0 & 0 & 0 & e34[[n]] & e35[[n]] & 0 \end{pmatrix} \cdot \begin{pmatrix} \varepsilon11[[n]] \\ \varepsilon22[[n]] \\ \varepsilon33[[n]] \\ 2\,\varepsilon23[[n]] \\ 2\,\varepsilon13[[n]] \\ 2\,\varepsilon12[[n]] \end{pmatrix} +$$

$$\begin{pmatrix} e11[[n]] & e12[[n]] & 0 \\ e12[[n]] & e22[[n]] & 0 \\ 0 & 0 & e33[[n]] \end{pmatrix} \cdot \begin{pmatrix} E1[[n]] \\ E2[[n]] \\ E3[[n]] \end{pmatrix};$$

```
}]
```

- **Apply boundary conditions on the top and bottom surfaces and interfaces**

```
u1d = ET; u2d = ET; u3d = ET; ϕd = ET;
σ11d = ET; σ22d = ET; σ33d = ET; σ23d = ET; σ13d = ET; σ12d = ET;
D3d = ET;

For[n = 1, n ≤ NL, n++, {
  u1d[[n]] = Simplify[Normal[u1[[n]] / Cos[p x1]]];
  u2d[[n]] = Simplify[Normal[u2[[n]] / Cos[p x1]]];
  u3d[[n]] = Simplify[Normal[u3[[n]] / Sin[p x1]]];
  ϕd[[n]] = Simplify[Normal[ϕ[[n]] / Cos[p x1]]];
  σ13d[[n]] = Simplify[Normal[σ13[[n]] / Cos[p x1]]];
  σ23d[[n]] = Simplify[Normal[σ23[[n]] / Cos[p x1]]];
  σ33d[[n]] = Simplify[Normal[σ33[[n]] / Sin[p x1]]];
  D3d[[n]] = Simplify[Normal[D3[[n]] / Cos[p x1]]];
 }]
```

```
BCBOTTOM = {σ13d[[1]] /. {x3 → -Hk[[1]] / 2},
    σ23d[[1]] /. {x3 → -Hk[[1]] / 2},
    σ33d[[1]] /. {x3 → -Hk[[1]] / 2},
    ϕd[[1]] /. {x3 → -Hk[[1]] / 2}};

INTERFACE1 = {
    (u1d[[1]] /. {x3 → Hk[[1]] / 2}) - (u1d[[2]] /. {x3 → -Hk[[2]] / 2}),
    (u2d[[1]] /. {x3 → Hk[[1]] / 2}) - (u2d[[2]] /. {x3 → -Hk[[2]] / 2}),
    (u3d[[1]] /. {x3 → Hk[[1]] / 2}) - (u3d[[2]] /. {x3 → -Hk[[2]] / 2}),
    (ϕd[[1]] /. {x3 → Hk[[1]] / 2}),
    (σ13d[[1]] /. {x3 → Hk[[1]] / 2}) - (σ13d[[2]] /. {x3 → -Hk[[2]] / 2}),
    (σ23d[[1]] /. {x3 → Hk[[1]] / 2}) - (σ23d[[2]] /. {x3 → -Hk[[2]] / 2}),
    (σ33d[[1]] /. {x3 → Hk[[1]] / 2}) - (σ33d[[2]] /. {x3 → -Hk[[2]] / 2}),
    (ϕd[[2]] /. {x3 → -Hk[[2]] / 2})
  };

INTERFACE2 = {
    (u1d[[2]] /. {x3 → Hk[[2]] / 2}) - (u1d[[3]] /. {x3 → -Hk[[3]] / 2}),
    (u2d[[2]] /. {x3 → Hk[[2]] / 2}) - (u2d[[3]] /. {x3 → -Hk[[3]] / 2}),
    (u3d[[2]] /. {x3 → Hk[[2]] / 2}) - (u3d[[3]] /. {x3 → -Hk[[3]] / 2}),
    (ϕd[[2]] /. {x3 → Hk[[2]] / 2}),
    (σ13d[[2]] /. {x3 → Hk[[2]] / 2}) - (σ13d[[3]] /. {x3 → -Hk[[3]] / 2}),
    (σ23d[[2]] /. {x3 → Hk[[2]] / 2}) - (σ23d[[3]] /. {x3 → -Hk[[3]] / 2}),
    (σ33d[[2]] /. {x3 → Hk[[2]] / 2}) - (σ33d[[3]] /. {x3 → -Hk[[3]] / 2}),
    (ϕd[[3]] /. {x3 → -Hk[[3]] / 2})
  };

BCTOP = {σ13d[[3]] /. {x3 → Hk[[3]] / 2},
    σ23d[[3]] /. {x3 → Hk[[3]] / 2},
    σ33d[[3]] /. {x3 → Hk[[3]] / 2},
    ϕd[[3]] /. {x3 → Hk[[3]] / 2}};

BC = Join[BCBOTTOM, INTERFACE1, INTERFACE2, BCTOP];
```

```
M = {};
For[n = 1, n ≤ 24, n++, {
  M = Append[M, {
     Coefficient[BC[[n]], U1t[1, 0]], Coefficient[BC[[n]], U2t[1, 0]],
     Coefficient[BC[[n]], U3t[1, 0]], Coefficient[BC[[n]], Bt[1, 0]],
     Coefficient[BC[[n]], U1t[1, 1]], Coefficient[BC[[n]], U2t[1, 1]],
     Coefficient[BC[[n]], U3t[1, 1]], Coefficient[BC[[n]], Bt[1, 1]],

     Coefficient[BC[[n]], U1t[2, 0]], Coefficient[BC[[n]], U2t[2, 0]],
     Coefficient[BC[[n]], U3t[2, 0]], Coefficient[BC[[n]], Bt[2, 0]],
     Coefficient[BC[[n]], U1t[2, 1]], Coefficient[BC[[n]], U2t[2, 1]],
     Coefficient[BC[[n]], U3t[2, 1]], Coefficient[BC[[n]], Bt[2, 1]],

     Coefficient[BC[[n]], U1t[3, 0]], Coefficient[BC[[n]], U2t[3, 0]],
     Coefficient[BC[[n]], U3t[3, 0]], Coefficient[BC[[n]], Bt[3, 0]],
     Coefficient[BC[[n]], U1t[3, 1]], Coefficient[BC[[n]], U2t[3, 1]],
     Coefficient[BC[[n]], U3t[3, 1]], Coefficient[BC[[n]], Bt[3, 1]]
    }]
 }]
```

■ Natural Frequencies

```
f[x_] := Det[M /. {ω → x}];

Nω = 25; Minω = 0; Maxω = 1;
Fun = {};
For[m = 0, m <= Nω, Fun = Join[Fun, {{
       (Minω + m (Maxω - Minω) / Nω), f[Minω + m (Maxω - Minω) / Nω]} }] ; m++]
ListPlot[Fun, PlotJoined → True]
```

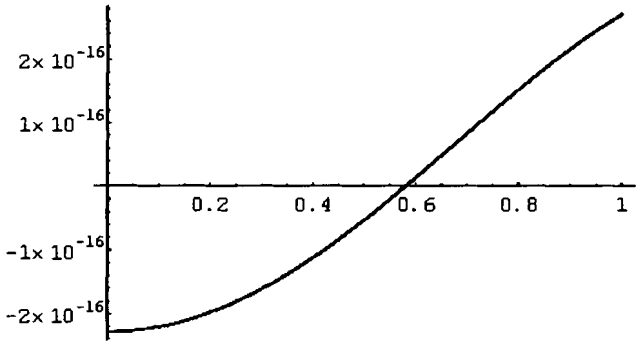

- Graphics -

```
Bisection[a0_, b0_, m_] := Module[{},
  a = N[a0]; b = N[b0]; c = (a + b) / 2;
  k = 0;
  Print[" f[a] =", NumberForm[f[a], 16]];
  Print[" f[b] =", NumberForm[f[b], 16]];
  While[k < m,
   If[Sign[f[b]] = Sign[f[c]], b = c, a = c;];
   c = (a + b) / 2;
   k = k + 1];
  Print[" Final b-a= ±", (b - a)];
  Print[" f[c]==", NumberForm[f[c], 16]]; Print[" c =", NumberForm[c, 16]];]

Bisection[6.2, 6.6, 50]
```

```
 f[a] =-1.14235499466492×10^-14

 f[b] =1.17110821972079×10^-14

 Final b-a= ±8.88178×10^-16

 f[c]= 4.535583968406345×10^-29

 c =6.41687076927594
```

```
Simplify[(c) (1/L0 Sqrt[Sigma0/ρ0]) / (2 π)]
```

```
14674.1
```

```
ωRule = {ω → c};
```

■ Determine the unknowns for the specified natural frequency

```
Coeffs = Flatten[NullSpace[M /. ωRule]];
```

```
URule = {U1t[1, 0] → Coeffs[[1]], U2t[1, 0] → Coeffs[[2]],
  U3t[1, 0] → Coeffs[[3]], Φt[1, 0] → Coeffs[[4]], U1t[1, 1] → Coeffs[[5]],
  U2t[1, 1] → Coeffs[[6]], U3t[1, 1] → Coeffs[[7]], Φt[1, 1] → Coeffs[[8]],

  U1t[2, 0] → Coeffs[[9]], U2t[2, 0] → Coeffs[[10]],
  U3t[2, 0] → Coeffs[[11]], Φt[2, 0] → Coeffs[[12]], U1t[2, 1] → Coeffs[[13]],
  U2t[2, 1] → Coeffs[[14]], U3t[2, 1] → Coeffs[[15]], Φt[2, 1] → Coeffs[[16]],

  U1t[3, 0] → Coeffs[[17]], U2t[3, 0] → Coeffs[[18]],
  U3t[3, 0] → Coeffs[[19]], Φt[3, 0] → Coeffs[[20]], U1t[3, 1] → Coeffs[[21]],
  U2t[3, 1] → Coeffs[[22]], U3t[3, 1] → Coeffs[[23]], Φt[3, 1] → Coeffs[[24]]
 }
```

$$\{U1t[1,0] \to -0.0156191,\ U2t[1,0] \to -3.57411\times10^{-16},\ U3t[1,0] \to -0.20014,$$
$$\Phi t[1,0] \to 8.04693\times10^{-17},\ U1t[1,1] \to 0.52328,\ U2t[1,1] \to 1.86949\times10^{-15},$$
$$U3t[1,1] \to -0.0182025,\ \Phi t[1,1] \to 3.30397\times10^{-15},\ U1t[2,0] \to -1.02147\times10^{-16},$$
$$U2t[2,0] \to -4.33848\times10^{-16},\ U3t[2,0] \to -0.200459,\ \Phi t[2,0] \to -4.83124\times10^{-17},$$
$$U1t[2,1] \to 0.575248,\ U2t[2,1] \to 8.00012\times10^{-17},\ U3t[2,1] \to -6.94682\times10^{-17},$$
$$\Phi t[2,1] \to -0.0000229496,\ U1t[3,0] \to 0.0156191,\ U2t[3,0] \to -3.6847\times10^{-16},$$
$$U3t[3,0] \to -0.20014,\ \Phi t[3,0] \to -2.34847\times10^{-31},\ U1t[3,1] \to 0.52328,$$
$$U2t[3,1] \to 1.69804\times10^{-16},\ U3t[3,1] \to 0.0182025,\ \Phi t[3,1] \to 1.08744\times10^{-29}\}$$

- **The displacements, potential, stresses and electric displacement corresponding to the specified natural frequency**

```
For[n = 1, n ≤ NL, n++, {
  u1[[n]] = Simplify[Normal[u1[[n]]] /. URule /. ωRule];
  u2[[n]] = Simplify[Normal[u2[[n]]] /. URule /. ωRule];
  u3[[n]] = Simplify[Normal[u3[[n]]] /. URule /. ωRule];
  ϕ[[n]] = Simplify[Normal[ϕ[[n]]] /. URule /. ωRule];
  σ11[[n]] = Simplify[Normal[σ11[[n]]] /. URule /. ωRule];
  σ22[[n]] = Simplify[Normal[σ22[[n]]] /. URule /. ωRule];
  σ33[[n]] = Simplify[Normal[σ33[[n]]] /. URule /. ωRule];
  σ23[[n]] = Simplify[Normal[σ23[[n]]] /. URule /. ωRule];
  σ13[[n]] = Simplify[Normal[σ13[[n]]] /. URule /. ωRule];
  σ12[[n]] = Simplify[Normal[σ12[[n]]] /. URule /. ωRule];
  D1[[n]] = Simplify[Normal[D1[[n]]] /. URule /. ωRule];
  D2[[n]] = Simplify[Normal[D2[[n]]] /. URule /. ωRule];
  D3[[n]] = Simplify[Normal[D3[[n]]] /. URule /. ωRule];
 }]
```

■ Solution as a function of x3

```
u1e[x_, z_] := ((u1[[LayerNum[z]]]) /. {x1 → x, x3 → z - Mk[[LayerNum[z]]]});
u2e[x_, z_] := ((u2[[LayerNum[z]]]) /. {x1 → x, x3 → z - Mk[[LayerNum[z]]]});
u3e[x_, z_] := ((u3[[LayerNum[z]]]) /. {x1 → x, x3 → z - Mk[[LayerNum[z]]]});
ϕe[x_, z_] := ((ϕ[[LayerNum[z]]]) /. {x1 → x, x3 → z - Mk[[LayerNum[z]]]});

σ11e[x_, z_] := ((σ11[[LayerNum[z]]]) /. {x1 → x, x3 → z - Mk[[LayerNum[z]]]});
σ22e[x_, z_] := ((σ22[[LayerNum[z]]]) /. {x1 → x, x3 → z - Mk[[LayerNum[z]]]});
σ33e[x_, z_] := ((σ33[[LayerNum[z]]]) /. {x1 → x, x3 → z - Mk[[LayerNum[z]]]});
σ23e[x_, z_] := ((σ23[[LayerNum[z]]]) /. {x1 → x, x3 → z - Mk[[LayerNum[z]]]});
σ13e[x_, z_] := ((σ13[[LayerNum[z]]]) /. {x1 → x, x3 → z - Mk[[LayerNum[z]]]});
σ12e[x_, z_] := ((σ12[[LayerNum[z]]]) /. {x1 → x, x3 → z - Mk[[LayerNum[z]]]});

D1e[x_, z_] := ((D1[[LayerNum[z]]]) /. {x1 → x, x3 → z - Mk[[LayerNum[z]]]});
D2e[x_, z_] := ((D2[[LayerNum[z]]]) /. {x1 → x, x3 → z - Mk[[LayerNum[z]]]});
D3e[x_, z_] := ((D3[[LayerNum[z]]]) /. {x1 → x, x3 → z - Mk[[LayerNum[z]]]});
```

■ Store results to file

```
NP = 1000; (*NP is the number of plot points*)

Res = {};
For[kp = 0, kp <= NP, Res = Join[Res, {{
     (-H / 2 + kp H / NP) / H,
     u1e[0, -H / 2 + kp H / NP],
     u2e[0, -H / 2 + kp H / NP],
     u3e[L / 2, -H / 2 + kp H / NP],
     ϕe[0, -H / 2 + kp H / NP],
     σ11e[L / 2, -H / 2 + kp H / NP],
     σ22e[L / 2, -H / 2 + kp H / NP],
     σ33e[L / 2, -H / 2 + kp H / NP],
     σ23e[0, -H / 2 + kp H / NP],
     σ13e[0, -H / 2 + kp H / NP],
     σ12e[L / 2, -H / 2 + kp H / NP],
     D1e[L / 2, -H / 2 + kp H / NP],
     D2e[L / 2, -H / 2 + kp H / NP],
     D3e[0, -H / 2 + kp H / NP]
    }}]; kp++]

FortranWrite["F:\\Documents\\Research\\Papers\\ShearVib\Results.txt", Res];
```

Appendix B

Mathematica Program for the Exact Solution of a Piezoelectric Shell

Exact solution for the cylindrical bending vibration of laminated cylindrical shells with shear actuators

Date: July 16, 2003
Authors: Senthil Vel and Brian Baillargeon
Department of Mechanical Engineering
Univeristy of Maine
Orono, ME 04469

Load Packages

```
Off[General::spell, General::spell1]

<< "F:\\Documents and Settings\\Baillargeon\\My Documents\\Publications\\Vibration of
   Piezoelectric Shear Shells in Cylindrical Bending\\4 Layer Composite\\FortranWrite"
<< Graphics`Graphics`;
<< Graphics`Legend`;
<< Graphics`MultipleListPlot`;
<< Graphics`Arrow`;
<< NumericalMath`SplineFit`;
<< LinearAlgebra`MatrixManipulation`;
(*Usage: FortranWrite["inp_file1.txt", array];*)
```

Program Input

- Number of terms in the series solution

```
Nmax = 40;
```

- Number of layers

```
NL = 4;
```

- Axial mode shape

```
k = 1;
```

■ The thickness mode shape

```
NMode = 1;
```

■ The geometry of the laminate

```
SR = 5;
H = 0.25 / SR;
R = 0.25;
Θ = 90 (π / 180);

(*a=0.3;R=10;
 Θ=a/R;
 SR=10;
 H = a/SR;*)

(*L=0.25; SR=4;
H =L/SR;*)
```

■ Constants for the normalization scheme

```
L0 = R;
Sigma0 = 100.0 x 10^9 ;
Eps0 = 150.0 x 10^-10;
V0 = L0 Sqrt[Sigma0 / Eps0] ;
e0 = (Sigma0 x L0) / V0;
ρ0 = 7750.0;
C0 = 21.1 x 10^9;
e02 = 12.322;

(*H = H/L0;*)
R = R / L0;
H = H / L0;
```

■ Applied load

```
q0 = 1.0 / Sigma0;
```

■ Location of the bottom, interfaces and top surfaces

```
Zk = {R - H / 2, R - H / 10, R - H / 20, R + H / 10, R + H / 2};
```

■ Elastic properties of the NL laminae

```
C11 = {183.443×10^9, 86.856×10^9, 86.856×10^9, 183.443×10^9} / Sigma0;
C22 ={11.662×10^9, 99.201×10^9, 99.201×10^9, 11.662×10^9} / Sigma0;
C33 = {11.662×10^9, 99.201×10^9, 99.201×10^9, 11.662×10^9} / Sigma0;
C12 = {4.363×10^9, 50.778×10^9, 50.778×10^9, 4.363×10^9} / Sigma0;
C13 = {4.363×10^9, 50.778×10^9, 50.778×10^9, 4.363×10^9} / Sigma0;
C23 = {3.918×10^9, 54.016×10^9, 54.016×10^9, 3.918×10^9} / Sigma0;
C44 = {2.870×10^9, 22.593×10^9, 22.593×10^9, 2.870×10^9} / Sigma0;
C55 = {7.170×10^9, 21.1×10^9, 21.1×10^9, 7.170×10^9} / Sigma0;
C66 = {7.170×10^9, 21.1×10^9, 21.1×10^9, 7.170×10^9} / Sigma0; C16 = {0, 0, 0, 0} / Sigma0;
C26 = {0, 0, 0, 0} / Sigma0;
C36 = {0, 0, 0, 0} / Sigma0;
C45 = {0, 0, 0, 0} / Sigma0;
```

■ Density of the NL laminae

```
ρ = {1590, 7750, 7750, 1590} / ρ0;
```

■ Piezoelectric and electric properties of the NL laminae

```
e11 = {0, 15.118, 15.118, 0} / e0;
e12 = {0, -7.209, -7.209, 0} / e0;
e13 = {0, -7.209, -7.209, 0} / e0;
e16 = {0, 0, 0, 0} / e0;
e21 = {0, 0, 0, 0} / e0;
e22 = {0, 0, 0, 0} / e0;
e23 = {0, 0, 0, 0} / e0;
e26 = {0, 12.322, 12.322, 0} / e0;
e34 = {0, 0, 0, 0} / e0;
e35 = {0, 12.322, 12.322, 0} / e0;
ε11 = {153×10^-10, 150×10^-10, 150×10^-10, 153×10^-10} / Eps0;
ε12 = {0, 0, 0, 0} / Eps0;
ε22 = {153×10^-10, 153×10^-10, 153×10^-10, 153×10^-10} / Eps0;
ε33 = {153×10^-10, 153×10^-10, 153×10^-10, 153×10^-10} / Eps0;
```

■ Frequency

```
(*ω=0.0;*)
```

■ PPF controller

$$\omega n = 686.118\ (2\pi)\ L0\ \sqrt{\frac{\rho 0}{Sigma0}}\ ;$$ (*Normalized controller frequency*)

```
ωf = ωn
```

```
0.300033
```

```
ξ = 0.05; g = 0.1;
```

Exact solution

- Given normalized r, find the lamina that the point belongs to.

```
LayerNum = Function[r,
   Do[If [(r ≥ Zk[[n]]) && (r ≤ Zk[[n+1]]), Return[n]], {n, NL}]];
```

- Empty table of length NL

```
ET = Table[0, {NL}] ;
```

- Layer thicknesses and midsurface location of each layer

```
Hk = ET; Mk = ET;
For[n = 1, n ≤ NL, n++, {
   Hk[[n]] = Zk[[n+1]] - Zk[[n]]}];
For[n = 1, n ≤ NL, n++, {
   Mk[[n]] = (Zk[[n+1]] + Zk[[n]]) / 2}];
```

- Parameter p

```
p = kπ/Θ;
```

- The series equations (LHS)

```
EQ1[β_, n_] := C13[[n]] Ar[β] (β+λ) -
   (C13[[n]] + C55[[n]]) p Aθ[β] (β+λ) + C33[[n]] Ar[β] (β+λ) (β+λ-1) -
   (C36[[n]] + C45[[n]]) p Ar[β] (β+λ) - (e13[[n]] + e35[[n]]) p Aφ[β] (β+λ) -
   C55[[n]] p² Ar[β] + C55[[n]] p Aθ[β] + (C33[[n]] - C13[[n]]) Ar[β] (β+λ) -
   C11[[n]] Ar[β] + C11[[n]] p Aθ[β] + C16[[n]] p Ar[β] + e11[[n]] p Aφ[β];

EQ2[β_, n_] := C45[[n]] Ar[β] (β+λ) (β+λ-1) +
   (C13[[n]] + C55[[n]]) p (β+λ) Ar[β] + C55[[n]] Aθ[β] (β+λ) (β+λ-1) +
   e35[[n]] Aφ[β] (β+λ) (β+λ-1) + C11[[n]] p (Ar[β] - p Aθ[β]) -
   C16[[n]] p² Ar[β] - e11[[n]] p² Aφ[β] + 2 C45[[n]] Ar[β] (β+λ) +
   C55[[n]] (p Ar[β] - Aθ[β]) + C55[[n]] Aθ[β] (β+λ) + 2 e35[[n]] Aφ[β] (β+λ);

EQ3[β_, n_] := C44[[n]] Ar[β] (β+λ) (β+λ-1) +
   (C45[[n]] + C36[[n]]) p Ar[β] (β+λ) + C45[[n]] Aθ[β] (β+λ) (β+λ-1) +
   e34[[n]] Aφ[β] (β+λ) (β+λ-1) + C16[[n]] p (Ar[β] - p Aθ[β]) - C66[[n]] p² Ar[β] -
   e16[[n]] p² Aφ[β] + C44[[n]] Ar[β] (β+λ) + e35[[n]] Aφ[β] (β+λ);
```

```
EQ4[β_, n_] := e34[[n]] Ax[β] (β + λ) (β + λ - 1) +
   (e13[[n]] + e35[[n]]) p (β + λ) Ax[β] + e35[[n]] (β + λ) (β + λ - 1) Aθ[β] -
   e33[[n]] (β + λ) (β + λ - 1) Aϕ[β] + e11[[n]] p (Ar[β] - p Aθ[β]) - e16[[n]] p^2 Ax[β] +
   e11[[n]] p^2 Aϕ[β] + e34[[n]] Ax[β] (β + λ) - e33[[n]] Aϕ[β] (β + λ);
```

- The matrix M required to find λ and for the recursive relations

```
M[β_, n_] := {{Coefficient[EQ1[β, n], Ar[β]], Coefficient[EQ1[β, n], Aθ[β]],
    Coefficient[EQ1[β, n], Ax[β]], Coefficient[EQ1[β, n], Aϕ[β]]},
   {Coefficient[EQ2[β, n], Ar[β]], Coefficient[EQ2[β, n], Aθ[β]],
    Coefficient[EQ2[β, n], Ax[β]], Coefficient[EQ2[β, n], Aϕ[β]]},
   {Coefficient[EQ3[β, n], Ar[β]], Coefficient[EQ3[β, n], Aθ[β]],
    Coefficient[EQ3[β, n], Ax[β]], Coefficient[EQ3[β, n], Aϕ[β]]},
   {Coefficient[EQ4[β, n], Ar[β]], Coefficient[EQ4[β, n], Aθ[β]],
    Coefficient[EQ4[β, n], Ax[β]], Coefficient[EQ4[β, n], Aϕ[β]]}
  };
```

- Determine λ from the indicial equation obtained by setting the determinant of M[0] to zero

```
For[kt = 1, kt ≤ NL,
  Ruleλ[kt] = Solve[Det[M[0, kt]] == 0, λ];
  ; kt++];

λs[n_] := {λ /. Ruleλ[n][[1]], λ /. Ruleλ[n][[2]], λ /. Ruleλ[n][[3]], λ /. Ruleλ[n][[4]],
   λ /. Ruleλ[n][[5]], λ /. Ruleλ[n][[6]], λ /. Ruleλ[n][[7]], λ /. Ruleλ[n][[8]]};
```

- The coefficient $A\theta[0]$, Ar[0], Ax[0] and $A\phi[0]$ are obtained from the nullspace of M[0] for each eigenvalue λ

```
NAr[k_, n_] := Flatten[NullSpace[M[0, n] /. (Ruleλ[n][[k]]), Tolerance → 10^-10]][[1]];
NAθ[k_, n_] := Flatten[NullSpace[M[0, n] /. (Ruleλ[n][[k]]), Tolerance → 10^-10]][[2]];
NAx[k_, n_] := Flatten[NullSpace[M[0, n] /. (Ruleλ[n][[k]]), Tolerance → 10^-10]][[3]];
NAϕ[k_, n_] := Flatten[NullSpace[M[0, n] /. (Ruleλ[n][[k]]), Tolerance → 10^-10]][[4]];
```

- Assign unknown multiplicative constants for each eigenvalue λ, based on whether λ is real or complex

```
λs[1]
λs[2]
λs[3]
λs[4]
```

```
{-10.6735, -3.16118, -2., -1.11476, 1.11476, 2., 3.16118, 10.6735}
```

```
{-2.75033, -1.97247, -1.93279, -0.9162, 0.9162, 1.93279, 1.97247, 2.75033}
```

```
{-2.75033, -1.97247, -1.93279, -0.9162, 0.9162, 1.93279, 1.97247, 2.75033}
```

```
{-10.6735, -3.16118, -2., -1.11476, 1.11476, 2., 3.16118, 10.6735}
```

```
Unknowns[1] = {B1[1], B2[1], B3[1], B4[1], B5[1], B6[1], B7[1], B8[1]};
Unknowns[2] = {B1[2], B2[2], B3[2], B4[2], B5[2], B6[2], B7[2], B8[2]};
Unknowns[3] = {B1[3], B2[3], B3[3], B4[3], B5[3], B6[3], B7[3], B8[3]};
Unknowns[4] = {B1[4], B2[4], B3[4], B4[4], B5[4], B6[4], B7[4], B8[4]};
```

■ Series solution for the displacements and electric potential

```
Urseries = ET; Uθseries = ET; Uzseries = ET; θseries = ET;
For[kt = 1, kt ≤ NL,
 For[k = 1, k ≤ 8, k++, {

   (* The zeroth order terms *)
   TAr[0, kt] = NAr[k, kt];
   TAθ[0, kt] = NAθ[k, kt];
   TAz[0, kt] = NAz[k, kt];
   TAϕ[0, kt] = NAϕ[k, kt];

   (* The first order terms *)
   {{TAr[1, kt]}, {TAθ[1, kt]}, {TAz[1, kt]}, {TAϕ[1, kt]}} = (Inverse[M[1, kt] /. Ruleλ[kt][[k]]]).{{0}, {0}, {0}, {0}};

   (* Recursive relations for higher order terms *)
   For[β = 2, β ≤ Nmax, β++, {
     {{TAr[β, kt]}, {TAθ[β, kt]}, {TAz[β, kt]}, {TAϕ[β, kt]}} =

       Simplify[(Inverse[M[β, kt] /. Ruleλ[kt][[k]]]).{{-ρ[[kt]] ω^2 TAr[β - 2, kt]}, {-ρ[[kt]] ω^2 TAθ[β - 2, kt]}, {-ρ[[kt]] ω^2 TAz[β - 2, kt]}, {0}}];

    }];

   Urseries[[kt]] = Urseries[[kt]] + Unknowns[kt][[k]] (Sum[TAr[β, kt] r^(β+λs[kt][[k]]), {β, 0, Nmax}]);

   Uθseries[[kt]] = Uθseries[[kt]] + Unknowns[kt][[k]] (Sum[TAθ[β, kt] r^(β+λs[kt][[k]]), {β, 0, Nmax}]);

   Uzseries[[kt]] = Uzseries[[kt]] + Unknowns[kt][[k]] (Sum[TAz[β, kt] r^(β+λs[kt][[k]]), {β, 0, Nmax}]);

   θseries[[kt]] = θseries[[kt]] + Unknowns[kt][[k]] (Sum[TAϕ[β, kt] r^(β+λs[kt][[k]]), {β, 0, Nmax}]);

  }];
 kt++];
```

■ The displacement and electric potential

```
For[kt = 1, kt ≤ NL,
  Urseries[[kt]] = Urseries[[kt]] + O[r] ^ (Nmax + 1);
  Uθseries[[kt]] = Uθseries[[kt]] + O[r] ^ (Nmax + 1);
  Uxseries[[kt]] = Uxseries[[kt]] + O[r] ^ (Nmax + 1);
  Φseries[[kt]] = Φseries[[kt]] + O[r] ^ (Nmax + 1); kt++];

uθ = ET; ux = ET; ur = ET; ϕ = ET;
For[kt = 1, kt ≤ NL,
  uθ[[kt]] = Uθseries[[kt]] Cos[p θ];
  ux[[kt]] = Uxseries[[kt]] Cos[p θ];
  ur[[kt]] = Urseries[[kt]] Sin[p θ];
  ϕ[[kt]] = Φseries[[kt]] Cos[p θ]; kt++];
```

■ The strains and the electric field

```
εθθ = ET; εrr = ET; εxx = ET; εrθ = ET; εθx = ET; εxr = ET; Eθ = ET; Er = ET; Ex = ET;
For[kt = 1, kt ≤ NL,
  εθθ[[kt]] = 1/r (∂θ uθ[[kt]] + ur[[kt]]);
  εrr[[kt]] = ∂r ur[[kt]];
  εxx[[kt]] = ∂x ux[[kt]];
  εrθ[[kt]] = 1/2 (1/r ∂θ ur[[kt]] + ∂r uθ[[kt]] - uθ[[kt]]/r);
  εθx[[kt]] = 1/2 (1/r ∂θ ux[[kt]]);
  εxr[[kt]] = 1/2 (∂r ux[[kt]]);
  Eθ[[kt]] = -1/r ∂θ ϕ[[kt]];
  Er[[kt]] = -∂r ϕ[[kt]];
  Ex[[kt]] = -∂x ϕ[[kt]]; kt++];
```

■ The stresses and electric displacements

```
σθθ = ET; σxx = ET; σrr = ET; σxr = ET; σrθ = ET; σθx = ET; Dθ = ET; Dx = ET; Dr = ET;
For[kt = 1, kt ≤ NL,

{{σθθ[[kt]]}, {σxx[[kt]]}, {σrr[[kt]]}, {σxr[[kt]]}, {σrθ[[kt]]}, {σθx[[kt]]}} =

{{C11[[kt]], C12[[kt]], C13[[kt]], 0, 0, C16[[kt]]},
 {C12[[kt]], C22[[kt]], C23[[kt]], 0, 0, C26[[kt]]},
 {C13[[kt]], C23[[kt]], C33[[kt]], 0, 0, C36[[kt]]},
 {0, 0, 0, C44[[kt]], C45[[kt]], 0},
 {0, 0, 0, C45[[kt]], C55[[kt]], 0},
 {C16[[kt]], C26[[kt]], C36[[kt]], 0, 0, C66[[kt]]}} . {{εθθ[[kt]]}, {εxx[[kt]]}, {εrr[[kt]]}, {2 εxr[[kt]]}, {2 εrθ[[kt]]}, {2 εθx[[kt]]}} -

{{e11[[kt]], e21[[kt]], 0},
 {e12[[kt]], e22[[kt]], 0},
 {e13[[kt]], e23[[kt]], 0},
 {0, 0, e34[[kt]]},
 {0, 0, e35[[kt]]},
 {e16[[kt]], e26[[kt]], 0}} . {{Eθ[[kt]]}, {Ex[[kt]]}, {Er[[kt]]}};

{{Dθ[[kt]]}, {Dx[[kt]]}, {Dr[[kt]]}} = {{e11[[kt]], e12[[kt]], e13[[kt]], 0, 0, e16[[kt]]},
 {e21[[kt]], e22[[kt]], e23[[kt]], 0, 0, e26[[kt]]},
 {0, 0, 0, e34[[kt]], e35[[kt]], 0}} .

{{εθθ[[kt]]}, {εxx[[kt]]}, {εrr[[kt]]}, {2 εxr[[kt]]}, {2 εrθ[[kt]]}, {2 εθx[[kt]]}} + {{e11[[kt]], e12[[kt]], 0},
 {e12[[kt]], e22[[kt]], 0},
 {0, 0, e33[[kt]]}} . {{Eθ[[kt]]}, {Ex[[kt]]}, {Er[[kt]]}}; kt++];
```

■ Check if the equations of motion and charge equation are satisfied

```
(*Chop[Simplify[Normal[∂r σrr[[1]] + 1/r ∂θ σrθ[[1]] +
      1/r (σrr[[1]] - σθθ[[1]]) + ρ[[1]] ω^2 ur[[1]]]/.{r→1.25}], 10^-9]
Chop[Simplify[Normal[∂r σrθ[[1]] + 1/r ∂θ σθθ[[1]] + 2/r σrθ[[1]] + ρ[[1]] ω^2 uθ[[1]]]/.
    {r→1.25}],10^-9]
Chop[Simplify[Normal[∂r σxr[[1]] + 1/r ∂θ σθx[[1]] + 1/r σxr[[1]] + ρ[[1]] ω^2 ux[[1]]]/.
    {r→1.25}],10^-9]
Chop[Simplify[Normal[∂r Dr[[1]] + 1/r (∂θ Dθ[[1]] + Dr[[1]])]/.{r→1.25}]]*)
```

■ PPF control

```
φf = Chop[Simplify[Normal[φ[[2]]] /. {θ → θ/2, r → Mk[[2]] - Hk[[2]]/2}]];
```

$$\eta = \frac{\omega n^2}{((\omega f^2 - \omega^2) + (2\,\xi)\,I\,\omega f\,\omega)}\,\phi f;$$

$$\phi 0 = \left(\frac{g\,Sigma0\,\omega f^2}{L0\,\rho 0\,V0}\right)\eta;$$

$$\phi 0;$$

- **Apply boundary conditions to determine the unknown coefficients**

```
uθd = ET; urd = ET; uxd = ET; φd = ET; σxrd = ET; σrθd = ET; σrrd = ET; Drd = ET;

For[kt = 1, kt ≤ NL,
  uθd[[kt]] = Simplify[Normal[uθ[[kt]] /. {θ -> 0}]];
  uxd[[kt]] =Simplify[Normal[ux[[kt]] /. {θ -> 0}]];
  urd[[kt]] = Simplify[Normal[ur[[kt]] /. {θ → π / (2 p)}]];
  φd[[kt]] =Simplify[Normal[φ[[kt]] /. {θ -> 0}]];
  σxrd[[kt]] = Simplify[Normal[σxr[[kt]] /. {θ -> 0}]];
  σrθd[[kt]] = Simplify[Normal[σrθ[[kt]] /. {θ -> 0}]];
  σrrd[[kt]] = Simplify[Normal[σrr[[kt]] /. {θ → π / (2 p)}]];
  Drd[[kt]] = Simplify[Normal[Dr[[kt]] /. {θ → 0}]]; kt++];
```

```
BCBOTTOM = {σrθd[[1]] /. {r → Mk[[1]] - Hk[[1]] / 2},
   σrrd[[1]] /. {r → Mk[[1]] - Hk[[1]] / 2},
   σrrd[[1]] /. {r → Mk[[1]] - Hk[[1]] / 2},
   ϕd[[1]] /. {r → Mk[[1]] - Hk[[1]] / 2}};

INTERFACE1 = {
   (uθd[[1]] /. {r → Mk[[1]] + Hk[[1]] / 2}) - (uθd[[2]] /. {r → Mk[[2]] - Hk[[2]] / 2}),
   (urd[[1]] /. {r → Mk[[1]] + Hk[[1]] / 2}) - (urd[[2]] /. {r → Mk[[2]] - Hk[[2]] / 2}),
   (urd[[1]] /. {r → Mk[[1]] + Hk[[1]] / 2}) - (urd[[2]] /. {r → Mk[[2]] - Hk[[2]] / 2}),
   (Drd[[1]] /. {r → Mk[[1]] + Hk[[1]] / 2}),
   (σrθd[[1]] /. {r → Mk[[1]] + Hk[[1]] / 2}) - (σrθd[[2]] /. {r → Mk[[2]] - Hk[[2]] / 2}),
   (σrrd[[1]] /. {r → Mk[[1]] + Hk[[1]] / 2}) - (σrrd[[2]] /. {r → Mk[[2]] - Hk[[2]] / 2}),
   (σrrd[[1]] /. {r → Mk[[1]] + Hk[[1]] / 2}) - (σrrd[[2]] /. {r → Mk[[2]] - Hk[[2]] / 2}),
   (Drd[[2]] /. {r → Mk[[2]] - Hk[[2]] / 2})
  };

INTERFACE2 = {
   (uθd[[2]] /. {r → Mk[[2]] + Hk[[2]] / 2}) - (uθd[[3]] /. {r → Mk[[3]] - Hk[[3]] / 2}),
   (urd[[2]] /. {r → Mk[[2]] + Hk[[2]] / 2}) - (urd[[3]] /. {r → Mk[[3]] - Hk[[3]] / 2}),
   (urd[[2]] /. {r → Mk[[2]] + Hk[[2]] / 2}) - (urd[[3]] /. {r → Mk[[3]] - Hk[[3]] / 2}),
   (ϕd[[2]] /. {r → Mk[[2]] + Hk[[2]] / 2}),
   (σrθd[[2]] /. {r → Mk[[2]] + Hk[[2]] / 2}) - (σrθd[[3]] /. {r → Mk[[3]] - Hk[[3]] / 2}),
   (σrrd[[2]] /. {r → Mk[[2]] + Hk[[2]] / 2}) - (σrrd[[3]] /. {r → Mk[[3]] - Hk[[3]] / 2}),
   (σrrd[[2]] /. {r → Mk[[2]] + Hk[[2]] / 2}) - (σrrd[[3]] /. {r → Mk[[3]] - Hk[[3]] / 2}),
   (ϕd[[3]] /. {r → Mk[[3]] - Hk[[3]] / 2})
  };

INTERFACE3 = {
   (uθd[[3]] /. {r → Mk[[3]] + Hk[[3]] / 2}) - (uθd[[4]] /. {r → Mk[[4]] - Hk[[4]] / 2}),
   (urd[[3]] /. {r → Mk[[3]] + Hk[[3]] / 2}) - (urd[[4]] /. {r → Mk[[4]] - Hk[[4]] / 2}),
   (urd[[3]] /. {r → Mk[[3]] + Hk[[3]] / 2}) - (urd[[4]] /. {r → Mk[[4]] - Hk[[4]] / 2}),
   (ϕd[[3]] /. {r → Mk[[3]] + Hk[[3]] / 2} - ϕ0),
   (σrθd[[3]] /. {r → Mk[[3]] + Hk[[3]] / 2}) - (σrθd[[4]] /. {r → Mk[[4]] - Hk[[4]] / 2}),
   (σrrd[[3]] /. {r → Mk[[3]] + Hk[[3]] / 2}) - (σrrd[[4]] /. {r → Mk[[4]] - Hk[[4]] / 2}),
   (σrrd[[3]] /. {r → Mk[[3]] + Hk[[3]] / 2}) - (σrrd[[4]] /. {r → Mk[[4]] - Hk[[4]] / 2}),
   (ϕd[[4]] /. {r → Mk[[4]] - Hk[[4]] / 2} - ϕ0)
  };

BCTOP = {σrθd[[4]] /. {r → Mk[[4]] + Hk[[4]] / 2},
   σrrd[[4]] /. {r → Mk[[4]] + Hk[[4]] / 2},
   σrrd[[4]] /. {r → Mk[[4]] + Hk[[4]] / 2},
   ϕd[[4]] /. {r → Mk[[4]] + Hk[[4]] / 2}};

BC = Join[BCBOTTOM, INTERFACE1, INTERFACE2, INTERFACE3, BCTOP];
```

```
MB = {};
For[n = 1, n ≤ 32, n++, {
  MB = Append[MB, {
     Coefficient[BC[[n]], B1[1]], Coefficient[BC[[n]], B2[1]],
     Coefficient[BC[[n]], B3[1]], Coefficient[BC[[n]], B4[1]],
     Coefficient[BC[[n]], B5[1]], Coefficient[BC[[n]], B6[1]],
     Coefficient[BC[[n]], B7[1]], Coefficient[BC[[n]], B8[1]],

     Coefficient[BC[[n]], B1[2]], Coefficient[BC[[n]], B2[2]],
     Coefficient[BC[[n]], B3[2]], Coefficient[BC[[n]], B4[2]],
     Coefficient[BC[[n]], B5[2]], Coefficient[BC[[n]], B6[2]],
     Coefficient[BC[[n]], B7[2]], Coefficient[BC[[n]], B8[2]],

     Coefficient[BC[[n]], B1[3]], Coefficient[BC[[n]], B2[3]],
     Coefficient[BC[[n]], B3[3]], Coefficient[BC[[n]], B4[3]],
     Coefficient[BC[[n]], B5[3]], Coefficient[BC[[n]], B6[3]],
     Coefficient[BC[[n]], B7[3]], Coefficient[BC[[n]], B8[3]],

     Coefficient[BC[[n]], B1[4]], Coefficient[BC[[n]], B2[4]],
     Coefficient[BC[[n]], B3[4]], Coefficient[BC[[n]], B4[4]],
     Coefficient[BC[[n]], B5[4]], Coefficient[BC[[n]], B6[4]],
     Coefficient[BC[[n]], B7[4]], Coefficient[BC[[n]], B8[4]]
    }]
 }]
```

- Forcing terms on RHS

```
RHS = {0, 0, 0, 0, 0, 0, 0, 0, 0, 0, 0, 0,
   0, 0, 0, 0, 0, 0, 0, 0, 0, 0, 0, 0, 0, 0, 0, 0, 0, 0, 0, q0, 0};
```

- Solve for unknown constants

```
Coeffs[ωr_] := Inverse[MB /. {ω -> ωr}].(RHS /. {ω -> ωr});

URule[ωr_] := {B1[1] → Coeffs[ωr][[1]], B2[1] → Coeffs[ωr][[2]],
   B3[1] → Coeffs[ωr][[3]], B4[1] → Coeffs[ωr][[4]], B5[1] → Coeffs[ωr][[5]],
   B6[1] → Coeffs[ωr][[6]], B7[1] → Coeffs[ωr][[7]], B8[1] → Coeffs[ωr][[8]],

   B1[2] → Coeffs[ωr][[9]], B2[2] → Coeffs[ωr][[10]],
   B3[2] → Coeffs[ωr][[11]], B4[2] → Coeffs[ωr][[12]], B5[2] → Coeffs[ωr][[13]],
   B6[2] → Coeffs[ωr][[14]], B7[2] → Coeffs[ωr][[15]], B8[2] → Coeffs[ωr][[16]],

   B1[3] → Coeffs[ωr][[17]], B2[3] → Coeffs[ωr][[18]],
   B3[3] → Coeffs[ωr][[19]], B4[3] → Coeffs[ωr][[20]], B5[3] → Coeffs[ωr][[21]],
   B6[3] → Coeffs[ωr][[22]], B7[3] → Coeffs[ωr][[23]], B8[3] → Coeffs[ωr][[24]],

   B1[4] → Coeffs[ωr][[25]], B2[4] → Coeffs[ωr][[26]],
   B3[4] → Coeffs[ωr][[27]], B4[4] → Coeffs[ωr][[28]], B5[4] → Coeffs[ωr][[29]],
   B6[4] → Coeffs[ωr][[30]], B7[4] → Coeffs[ωr][[31]], B8[4] → Coeffs[ωr][[32]]};
```

lisplacements, potential, stresses and electric displacement as function of r

```
uθe[x_, z_, ωf_] :=
  ((Normal[uθ[[LayerNum[z]]] /. {ω -> ωf}] /. URule[ωf]) /. {θ → x, r → z});
uxe[x_, z_, ωf_] :=
  ((Normal[ux[[LayerNum[z]]] /. {ω -> ωf}] /. URule[ωf]) /. {θ → x, r → z});
ure[x_, z_, ωf_] :=
  ((Normal[ur[[LayerNum[z]]] /. {ω -> ωf}] /. URule[ωf]) /. {θ → x, r → z});
φe[x_, z_, ωf_] := ((Normal[φ[[LayerNum[z]]] /. {ω -> ωf}] /. URule[ωf]) /. {θ → x, r → z});

σθθe[x_, z_, ωf_] :=
  ((Normal[σθθ[[LayerNum[z]]] /. {ω -> ωf}] /. URule[ωf]) /. {θ → x, r → z});
σxxe[x_, z_, ωf_] :=
  ((Normal[σxx[[LayerNum[z]]] /. {ω -> ωf}] /. URule[ωf]) /. {θ → x, r → z});
σrre[x_, z_, ωf_] :=
  ((Normal[σrr[[LayerNum[z]]] /. {ω -> ωf}] /. URule[ωf]) /. {θ → x, r → z});
σxre[x_, z_, ωf_] :=
  ((Normal[σxr[[LayerNum[z]]] /. {ω -> ωf}] /. URule[ωf]) /. {θ → x, r → z});
σrθe[x_, z_, ωf_] :=
  ((Normal[σrθ[[LayerNum[z]]] /. {ω -> ωf}] /. URule[ωf]) /. {θ → x, r → z});
σθxe[x_, z_, ωf_] :=
  ((Normal[σθx[[LayerNum[z]]] /. {ω -> ωf}] /. URule[ωf]) /. {θ → x, r → z});

Dθe[x_, z_, ωf_] :=
  ((Normal[Dθ[[LayerNum[z]]] /. {ω -> ωf}] /. URule[ωf]) /. {θ → x, r → z});
Dxe[x_, z_, ωf_] :=
  ((Normal[Dx[[LayerNum[z]]] /. {ω -> ωf}] /. URule[ωf]) /. {θ → x, r → z});
Dre[x_, z_, ωf_] := ((Normal[Dr[[LayerNum[z]]] /. {ω -> ωf}] /. URule[ωf]) /. {θ → x, r → z});

(*Plot[Abs[ure[θ/2,R+H/2,ωf]],{ωf,0.1,0.5}]*)
```

■Store results to file

```
NP = 100; (*NP is the number of plot points*)
STF = 0.1;
ENDF = 1;

Res = {};
For[kp = 0, kp <= NP, Res = Join[Res, {{
      (STF + (kp * (ENDF - STF))/NP) 1/(2 π L0) Sqrt[Sigma0/ρ0],
      (Re[ure[θ/2, R+H/2, (STF + (kp * (ENDF - STF))/NP)]]^2 +
         Im[ure[θ/2, R+H/2, (STF + (kp * (ENDF - STF))/NP)]]^2)^(1/2) (C0/(q0 Sigma0)),
      N[ArcTan[Re[ure[θ/2, R+H/2, (STF + (kp * (ENDF - STF))/NP)]],
        Im[ure[θ/2, R+H/2, (STF + (kp * (ENDF - STF))/NP)]]]]
    }}]; kp++];

FortranWrite["F:\\Documents and Settings\\Baillargeon\\My Documents\\
    Publications\\Vibration of Piezoelectric Shear Shells in Cylindrical
    Bending\\4 Layer Composite\Results_Composite_PPF_Model.txt", Res];

Res
```

Appendix C

Simulink Block Diagrams for Active Feedback Control

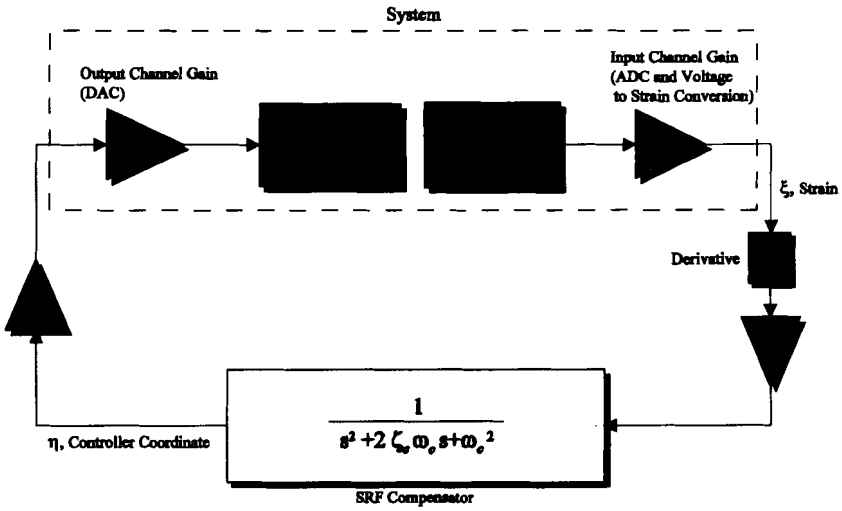

Figure C.1. Simulink block diagram for the SRF control algorithm

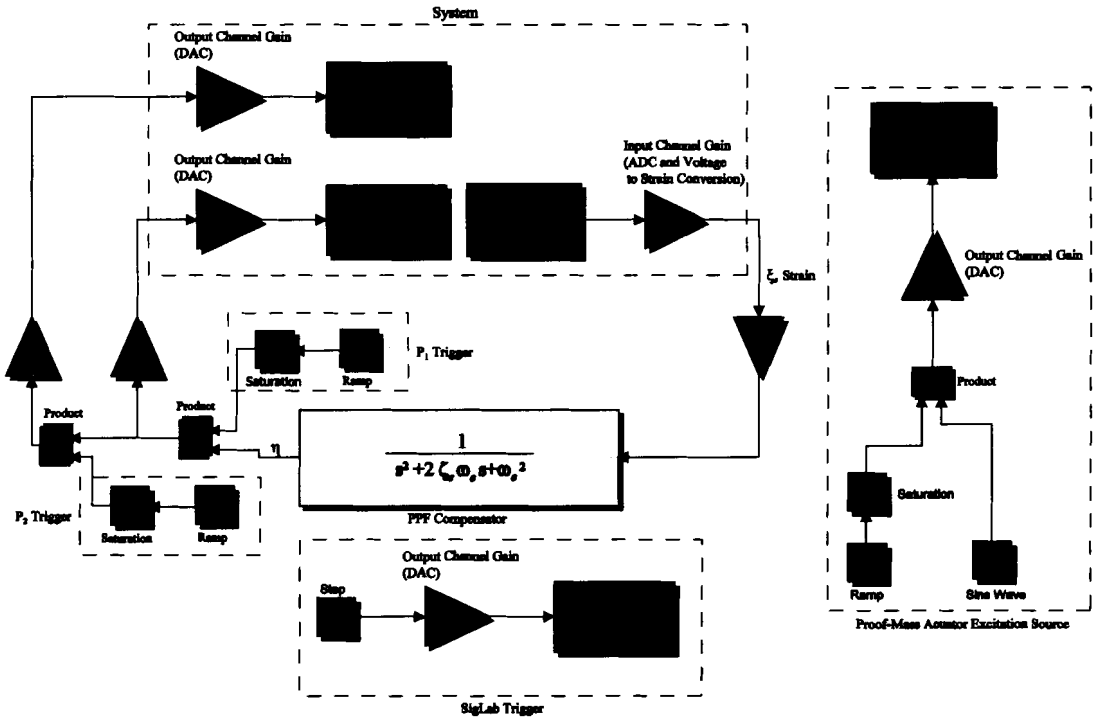

Figure C.2. Simulink block diagram for PPF control using two actuators

Appendix D

FORTRAN Program for Computing the Frequency Response Function Using ABAQUS

```
      PROGRAM PPF_CONTROL
************************************************************************
*
* THIS PROGRAM ANALYZES THE ACTIVE FEEDBACK CONTROL OF A CANTILEVER
* BEAM
* USING A POSITIVE POSITION FEEDBACK (PPF) CONTROL LAW.  THE STEADY
* STATE
* VIBRATION RESPONSE IS FOUND VERSUS FORCING FREQUENCY.
*
* AN ITERATIVE PROCESS IS USED TO DETERMINE THE ACTUATOR CONTROL
* VOLTAGE
* VERSUS FORCING FREQUENCY.  A MULLER'S METHOD IS USED TO FIND THE
* SOLUTION.
*
* WRITTEN BY BRIAN P. BAILLARGEON
* OCT. 21, 2003
*
* INPUT
* FREQ_I          : THE INITIAL FORCING FREQUENCY
* FREQ_F          : THE FINAL FORCING FREQUENCY
* NUM_POINTS      : THE NUMBER OF FREQUENCY POINTS IN THE RANGE FROM
*                   FREQ_I TO FREQ_F
* GUESS_V(N)      : THE FIRST 3 GUESS ACTUATOR VOLTAGES
* MAX_ITER        : THE MAXIMUM NUMBER OF ITERATIONS ALLOWED FOR EACH
*                   FORCING FREQUENCY
* TOL             : THE TOLERANCE USED TO DETERMINE IF THE SOLUTION HAS
*                   CONVERGED
*
* OUTPUT
* FREQ            : THE CURRENT FORCING FREQUENCY
* ACT_MAG         : THE MAGNITUDE OF VOLTAGE APPLIED TO THE ACTUATOR FOR A
*                   GIVEN FREQUENCY
* ACT_PHASE       : THE PHASE OF THE VOLTAGE APPLIED TO THE ACTUATOR FOR A
*                   GIVEN FREQUENCY
* STRAIN_MAG      : THE MAGNITUDE OF STRAIN AT THE SENSOR LOCATION FOR A
*                   GIVEN FREQUENCY
* STRAIN_PHASE    : THE PHASE OF THE STRAIN AT THE SENSOR LOCATION FOR A
*                   GIVEN FREQUENCY
* ACCEL_MAG       : THE MAGNITUDE OF ACCELERATION AT THE TIP OF THE BEAM
*                    FOR A GIVEN FREQUENCY
*
************************************************************************
      DIMENSION GUESS_V(3),RESID_V(3)
      REAL FREQ,POT_REAL,POT_IMAG,TOL,ACCEL_MAG,
     1 ACT_MAG,ACT,PHASE,STRAIN_MAG,STRAIN_PHASE,FREQ_I,
```

```
     2 FREQ_F
      COMPLEX GUESS_V,RESID,RESID_V,Q,A,B,C,DENOM_1,
     1 DENOM_2,DENOM,NEXT_V
      INTEGER MAX_ITER,ITER,NUM_POINTS,INC
      LOGICAL G,J,Y,NUM
      COMMON RESID
C
C READ THE INPUT PARAMETERS STORED IN Input_Parameters.txt
      OPEN(UNIT=102, FILE='Input_Parameters.txt', STATUS='OLD')
      READ(102,*)
      READ(102,*)FREQ_I,FREQ_F,NUM_POINTS
      READ(102,*)
      READ(102,*)POT_REAL,POT_IMAG
      GUESS_V(1) = (POT_REAL,POT_IMAG)
      READ(102,*)POT_REAL,POT_IMAG
      GUESS_V(2) = (POT_REAL,POT_IMAG)
      READ(102,*)POT_REAL,POT_IMAG
      GUESS_V(3) = (POT_REAL,POT_IMAG)
      READ(102,*)
      READ(102,*)MAX_ITER
      READ(102,*)
      READ(102,*)TOL
      CLOSE(102)
C
C INITIALIZE THE INCREMENT TO BE ZERO (NUM IS USED FOR STALL LOOP)
      INC = 0
      NUM = 0
C
C OPEN THE RESULTS FILES (Accel.txt, Strain.txt, Act_Pot.txt)
      OPEN(UNIT=105,FILE='Accel.txt', STATUS='OLD')
      OPEN(UNIT=106,FILE='Strain.txt', STATUS='OLD')
      OPEN(UNIT=107,FILE='Act_Pot.txt', STATUS='OLD')
C
80    CONTINUE
C
C DETERMINE THE CURRENT FORCING FREQUENCY
      FREQ = FREQ_I + ((FREQ_F-FREQ_I)/NUM_POINTS)*INC
      PRINT *, FREQ
C
C INITIALIZE THE INTERATION TO BE ZERO
      ITER = 0
C
C
C FIND THE RESIDUAL BASED ON INITIAL GUESS #1
      CALL RESID_EST(GUESS_V(1),FREQ)
      RESID_V(1) = RESID
C WAIT FOR THE SCRATCH FILES TO BE WRITTEN THEN DELETE THEM
      G = FALSE
      J = FALSE
      Y = FALSE
140   CONTINUE
       INQUIRE (FILE='Act_Scratch.txt',EXIST=G)
       INQUIRE (FILE='Strain_Scratch.txt',EXIST=J)
       INQUIRE (FILE='Accel_Scratch.txt',EXIST=Y)
      IF (G.EQ.FALSE.OR.J.EQ.FALSE.OR.Y.EQ.FALSE) THEN
        GOTO 140
```

```
      ENDIF
      OPEN(UNIT=112,FILE='Act_Scratch.txt',STATUS='OLD')
      OPEN(UNIT=111,FILE='Strain_Scratch.txt',STATUS='OLD')
      OPEN(UNIT=110,FILE='Accel_Scratch.txt',STATUS='OLD')
      CLOSE(UNIT=112, STATUS='DELETE')
      CLOSE(UNIT=111, STATUS='DELETE')
      CLOSE(UNIT=110, STATUS='DELETE')
C
C FIND THE RESIDUAL BASED ON INITIAL GUESS #2
      CALL RESID_EST(GUESS_V(2),FREQ)
      RESID_V(2) = RESID
C WAIT FOR THE SCRATCH FILES TO BE WRITTEN THEN DELETE THEM
      G = FALSE
      J = FALSE
      Y = FALSE
150   CONTINUE
       INQUIRE (FILE='Act_Scratch.txt',EXIST=G)
       INQUIRE (FILE='Strain_Scratch.txt',EXIST=J)
       INQUIRE (FILE='Accel_Scratch.txt',EXIST=Y)
      IF (G.EQ.FALSE.OR.J.EQ.FALSE.OR.Y.EQ.FALSE) THEN
        GOTO 150
      ENDIF
      OPEN(UNIT=112,FILE='Act_Scratch.txt',STATUS='OLD')
      OPEN(UNIT=111,FILE='Strain_Scratch.txt',STATUS='OLD')
      OPEN(UNIT=110,FILE='Accel_Scratch.txt',STATUS='OLD')
      CLOSE(UNIT=112, STATUS='DELETE')
      CLOSE(UNIT=111, STATUS='DELETE')
      CLOSE(UNIT=110, STATUS='DELETE')
C
C FIND THE RESIDUAL BASED ON INITIAL GUESS #3
      CALL RESID_EST(GUESS_V(3),FREQ)
      RESID_V(3) = RESID
C
C ITERATE TO MAKE RESIDUAL ZERO - MULLER'S METHOD
60    CONTINUE
       PRINT *, '**'
       PRINT *, GUESS_V(3),RESID_V(3)
C WAIT FOR THE SCRATCH FILES TO BE WRITTEN THEN DELETE THEM
       G = FALSE
       J = FALSE
       Y = FALSE
170   CONTINUE
      INQUIRE (FILE='Act_Scratch.txt',EXIST=G)
      INQUIRE (FILE='Strain_Scratch.txt',EXIST=J)
      INQUIRE (FILE='Accel_Scratch.txt',EXIST=Y)
     IF (G.EQ.FALSE.OR.J.EQ.FALSE.OR.Y.EQ.FALSE) THEN
       GOTO 170
     ENDIF

       OPEN(UNIT=112,FILE='Act_Scratch.txt',STATUS='OLD')
       OPEN(UNIT=111,FILE='Strain_Scratch.txt',STATUS='OLD')
       OPEN(UNIT=110,FILE='Accel_Scratch.txt',STATUS='OLD')
       CLOSE(UNIT=112, STATUS='DELETE')
       CLOSE(UNIT=111, STATUS='DELETE')
       CLOSE(UNIT=110, STATUS='DELETE')
C MULLER'S METHOD TO FORCE RESIDUAL TO BE ZERO
```

```
      Q = (GUESS_V(3)-GUESS_V(2))/(GUESS_V(2)-GUESS_V(1))
      A = Q*RESID_V(3)-(Q*(1+Q)*RESID_V(2))+(Q**2)*RESID_V(1)
      B = (2*Q+1)*RESID_V(3)-((1+Q)**2)*RESID_V(2)+
     1     (Q**2)*RESID_V(1)
      C = (1+Q)*RESID_V(3)
      DENOM_1 = B+SQRT((B**2)-(4*A*C))
      DENOM_2 = B-SQRT((B**2)-(4*A*C))
      IF (ABS(DENOM_1).GT.ABS(DENOM_2)) THEN
       DENOM = DENOM_1
      ELSE
       DENOM = DENOM_2
      ENDIF
      NEXT_V = GUESS_V(3)-(GUESS_V(3)-GUESS_V(2))*((2*C)/DENOM)
      RESID_V(1) = RESID_V(2)
      GUESS_V(1) = GUESS_V(2)
      RESID_V(2) = RESID_V(3)
      GUESS_V(2) = GUESS_V(3)
      GUESS_V(3) = NEXT_V
      CALL RESID_EST(GUESS_V(3),FREQ)
      RESID_V(3) = RESID
      ITER = ITER + 1
C CHECK TO MAKE SURE THERE HAVE NOT BEEN TOO MANY ITERATIONS
      IF (ITER.GT.MAX_ITER) THEN
       PRINT *, 'TOO MANY ITERATIONS'
       GOTO 70
      ENDIF
C DETERMINE IF THE RESIDUAL IS SMALL ENOUGH TO ASSUME CONVERGENCE
    IF (ABS(RESID_V(3)).GT.TOL) THEN
      GOTO 60
    END IF
C
70   PRINT *, GUESS_V(3),RESID_V(3)
C
C WRITE THE FINAL ITERATION RESULTS TO THE RESULT FILES AND DELETE THE
C SCRATCH FILES WHEN DONE
    G = FALSE
    J = FALSE
    Y = FALSE
130  CONTINUE
     INQUIRE (FILE='Act_Scratch.txt',EXIST=G)
     INQUIRE (FILE='Strain_Scratch.txt',EXIST=J)
     INQUIRE (FILE='Accel_Scratch.txt',EXIST=Y)
    IF (G.EQ.FALSE.OR.J.EQ.FALSE.OR.Y.EQ.FALSE) THEN
      GOTO 130
    ENDIF
180  CONTINUE
    NUM = NUM +1
    IF (NUM.LE.100000) THEN
     GOTO 180
    ENDIF
    NUM = 0
110  FORMAT(F20.15, 1X, F20.15)
    OPEN(UNIT=112,FILE='Act_Scratch.txt',STATUS='OLD')
    READ(112, 110)ACT_MAG,ACT_PHASE
    CLOSE(UNIT=112, STATUS='DELETE')
    WRITE(107, *)FREQ,ACT_MAG,ACT_PHASE
```

```
      OPEN(UNIT=111,FILE='Strain_Scratch.txt',STATUS='OLD')
      READ(UNIT=111, 110)STRAIN_MAG,STRAIN_PHASE
      CLOSE(UNIT=111, STATUS='DELETE')
      WRITE(106, *)FREQ,STRAIN_MAG,STRAIN_PHASE
120   FORMAT(F20.15)
      OPEN(UNIT=110,FILE='Accel_Scratch.txt',STATUS='OLD')
      READ(UNIT=110, 120)ACCEL_MAG
      CLOSE(UNIT=110,STATUS='DELETE')
      WRITE(105, *)FREQ,ACCEL_MAG
      PRINT *, FREQ,ACCEL_MAG
C
C FIND THE NEXT INCREMENT NUMBER AND DETERMINE IF PROGRAM SHOULD CONTINE
      INC = INC + 1
      IF (INC.LE.NUM_POINTS) THEN
        GOTO 80
      ENDIF
C
C CLOSE THE RESULT FILES AND END PROGRAM
      CLOSE(UNIT=105)
      CLOSE(UNIT=106)
      CLOSE(UNIT=107)
      END
**********************************************************************
      SUBROUTINE RESID_EST(GUESS_V,FREQ)
**********************************************************************
*
* THIS IS A FUNCTION TO DETERMINE THE RESIDUAL VOLTAGE FOR THE MULLER'S
* METHOD ITERATION TO DETERMINE THE FEEDBACK CONTROL VOLTAGE VERSUS
* FREQUENCY
*
* WRITTEN BY BRIAN P. BAILLARGEON
* OCT. 21, 2003
*
* INPUT
* GUESS_V  : THIS IS THE PPF ACTUATOR CONTROL VOLTAGE ESTIMATE
* FREQ     : THE CURRENT FORCING FREQUENCY
*
* OUTPUT
* RESID    : THE RESIDUAL VOLTAGE BETWEEN THE GUESS AND RESULTING
*            PPF ACTUATOR CONTROL VOLTAGE
*
**********************************************************************
      REAL F_POT_REAL,F_POT_IMAG,FREQ,S_POT_MAG,S_POT_ANGLE, PI
      COMPLEX RESID,S_POT,RES_VOLT,GUESS_V
      INTEGER ID,BI
      LOGICAL K
      DATA N_FREQ,PI /12295,3.141592653589793/
      COMMON RESID
C
C THE COMPONENTS OF THE ACTUATOR POTENTIAL GUESS
      F_POT_REAL = REAL(GUESS_V)
      F_POT_IMAG = IMAG(GUESS_V)
C
C ALTER THE ABAQUS INPUT FILE
      CALL ALT_INPUT_FILE(FREQ,N_FREQ,F_POT_REAL,F_POT_IMAG)
C
```

```
C SPAWN ABAQUS TO SOLVE THE FE PROBLEM
      CALL system('rm FRF_Test.com FRF_Test.dat FRF_Test.fil
     1 FRF_Test.log FRF_Test.mdl FRF_Test.msg FRF_Test.odb
     2 FRF_Test.prt FRF_Test.res FRF_Test.sta FRF_Test.stt')
      CALL system('abaqus job=FRF_Test user=FRF_PPF.f &')
C
C WAIT FOR ABAQUS TO FINISH THE ANALYSIS TO FIND THE VALUE OF STRAIN
C AT THE SENSOR LOCATION
      K = FALSE
50    CONTINUE
      INQUIRE (FILE='SENSOR_OUTPUT.txt',EXIST=K)
      IF(K.EQ.F) THEN
        GOTO 50
      END IF
C
C READ THE STRAIN AND DELETE THE SCRATCH FILE - THE LOOP IS TO
C MAKE SURE ABAQUS IS DONE WRITING THE RESULTS TO THE FILE
      BI = 0
200   CONTINUE
      BI = BI + 1
      IF (BI.LT.100000) THEN
        GOTO 200
      ENDIF
      OPEN(UNIT=104,FILE='SENSOR_OUTPUT.txt',STATUS='OLD')
      READ(104,*)S_POT_MAG,S_POT_ANGLE
      CLOSE(UNIT=104, STATUS='DELETE')
      S_POT = ((S_POT_MAG/1.E-6)*COS(PI*S_POT_ANGLE/180.0),
     1 (S_POT_MAG/1.E-6)*SIN(PI*S_POT_ANGLE/180.0))
C
C DETERMINE THE NEEDED PPF CONTROL VOLTAGE FOR THE DETECTED STRAIN
      RES_VOLT = (ACT_VOLT(S_POT,2*PI*FREQ,0),
     1 ACT_VOLT(S_POT,2*PI*FREQ,1))
C
C DETERMINE THE RESIDUAL VOLTAGE
      RESID = GUESS_V-RES_VOLT
      END
************************************************************************
      SUBROUTINE ALT_INPUT_FILE(FREQ,N_FREQ,F_POT_REAL,F_POT_IMAG)
************************************************************************
*
* THIS SUBROUTINE ALTERS THE ABAQUS INPUT FILE TO ANALYZE THE STEADY STATE
* ANALYSIS OF THE CANTILEVER BEAM FOR DIFFERENT FORCING FREQUENCIES AND
* PPF CONTROL VOLTAGES.
*
* WRITTEN BY BRIAN P. BAILLARGEON
* OCT. 21, 2003
*
* INPUT
* FREQ          : THE CURRENT FORCING FREQUENCY
* F_POT_REAL    : THE REAL COMPONENT OF THE ACTUATOR POTENTIAL
* F_POT_IMAG    : THE IMAGINARY PARY OF THE ACTUATOR POTENTIAL
* N_FREQ        : AN INTEGER SPECIFING WHERE THE STEP PARAMETERS ARE IN THE
*                 INPUT FILE - 1
*
* OUTPUT
* NO OUTPUT. THE INPUT FILE FRF_Test.inp IS ALTERED.
```

```
*
**********************************************************************
C
      REAL FREQ,F_POT_REAL,F_POT_IMAG
      INTEGER N_FREQ, N
C FIND THE POSITION OF THE STEP PARAMETER LINE
      OPEN(UNIT=103, FILE='FRF_Test.inp', STATUS='OLD')
      DO 10 N = 1, N_FREQ
        READ(103,*)
10    CONTINUE
C
C WRITE THE REST OF THE INPUT FILE
20    FORMAT(F8.3,', ',F8.3,', 1, 1., 1')
      WRITE(103,20) FREQ, FREQ
      WRITE(103,*)'**'
      WRITE(103,*)'** BOUNDARY CONDITIONS'
      WRITE(103,*)'**'
      WRITE(103,*)'** Name: Clamped Type: Symmetry/Antisymmetry/
     1Encastre'
      WRITE(103,*)'*Boundary'
      WRITE(103,*)'_PickedSet579, ENCASTRE'
      WRITE(103,*)'** Name: Control_Load Type: Electric potential'
      WRITE(103,*)'*Boundary, load case=1'
30    FORMAT('_PickedSet587, 9, 9, ',F10.3)
      WRITE(103,30) F_POT_REAL
      WRITE(103,*)'*Boundary, load case=2'
40    FORMAT('_PickedSet587, 9, 9, ',F10.3)
      WRITE(103,40) F_POT_IMAG
      WRITE(103,*)'** Name: Potential_Load Type: Electric potential'
      WRITE(103,*)'*Boundary, load case=1'
      WRITE(103,*)'_PickedSet581, 9, 9, 120.'
      WRITE(103,*)'*Boundary, load case=2'
      WRITE(103,*)'_PickedSet581, 9, 9'
      WRITE(103,*)'** Name: Zero_Potential Type: Electric potential'
      WRITE(103,*)'*Boundary, load case=1'
      WRITE(103,*)'_PickedSet588, 9, 9'
      WRITE(103,*)'*Boundary, load case=2'
      WRITE(103,*)'_PickedSet588, 9, 9'
      WRITE(103,*)'**'
      WRITE(103,*)'** OUTPUT REQUESTS'
      WRITE(103,*)'**'
      WRITE(103,*)'*Restart, write, frequency=1'
      WRITE(103,*)'**'
      WRITE(103,*)'** FIELD OUTPUT: F-Output-1'
      WRITE(103,*)'**'
      WRITE(103,*)'*Output, field'
      WRITE(103,*)'*Node Output'
      WRITE(103,*)'U, V, A, EPOT'
      WRITE(103,*)'*Node File'
      WRITE(103,*)'PHPOT, A'
      WRITE(103,*)'*Element Output'
      WRITE(103,*)'S, E'
      WRITE(103,*)'*EL FILE'
      WRITE(103,*)'PHE'
      WRITE(103,*)'**'
      WRITE(103,*)'** HISTORY OUTPUT: H-Output-1'
```

```
      WRITE(103,*)'**'
      WRITE(103,*)'*Output, history, variable=PRESELECT'
      WRITE(103,*)'*El Print, freq=999999'
      WRITE(103,*)'*Node Print, freq=999999'
      WRITE(103,*)'*End Step'
      CLOSE(103)
C
      END
************************************************************************
      FUNCTION ACT_VOLT(S_POT,FREQ,IU)
************************************************************************
*
* THIS FUNCTION RETURNS THE REQUIRED PPF ACTUATOR VOLTAGE DUE TO THE
* STRAIN POTENTIAL.
*
* WRITTEN BY BRIAN P. BAILLARGEON
* OCT. 21, 2003
*
* INPUT VARIABLES
* FREQ        : THE CURRENT VALUE OF THE FORCING FREQUENCY
* S_POT       : THE COMPLEX VALUE OF STRAIN AT THE SENSOR LOCATION
* IU          : A FLAG TO INDICATE WHETHER THE REAL OR IMAGINARY PART IS
*               NEEDED
*
* OUTPUT
* ACT_VOLT  : THE CALCULATED ACTUATOR VOLTAGE
*
************************************************************************
      REAL F_PI,WN,WF,ZETA,G,ACT_GAIN,FREQ,FILE_WN,FILE_N,FILE_Z,
     1 FILE_G
      COMPLEX S_POT
      INTEGER IU
C
      DATA F_PI,ACT_GAIN /3.141592653589793, 68.0/
C
C LOAD THE PPF CONTROLLER PARAMETERS FROM FILE PPF_Controller.txt
      OPEN(UNIT=120, FILE='PPF_Controller.txt',STATUS='OLD')
      READ(120,*)
      READ(120,*)FILE_WN
      READ(120,*)
      READ(120,*)FILE_N
      READ(120,*)
      READ(120,*)FILE_Z
      READ(120,*)
      READ(120,*)FILE_G
      CLOSE(UNIT=120)
C
C DEFINE THE PPF CONTROLLER
      WF = 2.0*F_PI*FILE_WN*FILE_N
      ZETA = FILE_Z
      G = FILE_G
C
C DETERMINE THE VOLTAGE TO THE CONTROL ACTUATOR
      IF (IU.EQ.0) THEN
        ACT_VOLT = REAL(((G,0)*(WF**4,0)*(ACT_GAIN,0)*S_POT)/
     1 ((WF**2,0)-(FREQ**2,0)+(0,2*ZETA*WF*FREQ)))
```

```
      ELSE IF (IU.EQ.1) THEN
        ACT_VOLT = AIMAG(((G,0)*(WF**4,0)*(ACT_GAIN,0)*S_POT)/
     1 ((WF**2,0)-(FREQ**2,0)+(0,2*ZETA*WF*FREQ)))
      END IF
      END
*SUBROUTINE URDFIL
*WRITTEN BY BRIAN P. BAILLARGEON 01/08/2003
*THIS SUBROUTINE READS THE RESTULTS FILE OF AN ABAQUS ANALYSIS
*****************************************************************
* LSTOP - FLAG TO INDICATE WHETHER THE ANALYSIS SHOULD CONTINUE (NOT
* USED)
* LOVRWRT - INDICATES WHETHER OR NOT THE RESULT FILE CAN BE OVERWRITTEN
* KSTEP - INDICATES THE CURRENT STEP
* KINC - INDICATES THE CURRENT INCREMENT
* DTIME - THE TIME INCREMENT
* TIME(1) - INDICATES THE STEP TIME AT THE END OF THE INCREMENT
* TIME(2) - INDICATES THE TOTAL TIME AT THE END OF THE INCREMENT
*****************************************************************
      SUBROUTINE URDFIL(LSTOP,LOVRWRT,KSTEP,KINC,DTIME,TIME)
C
      INCLUDE 'ABA_PARAM.INC'
C
      DIMENSION ARRAY(513),JRRAY(NPRECD,513),TIME(2)
      EQUIVALENCE (ARRAY(1),JRRAY(1,1))
      REAL D_E1,D_G21,D_T1,F_STRAIN,F_ACCEL
      INTEGER F_NODE, KI
      DATA D_E1,D_G21,D_T1 /61.0E9,17.130924E-3,0.00001/
C
C FIND THE CURRENT INCREMENT
C
      CALL POSFIL(KSTEP,KINC,ARRAY,JRCD)
      KI = 0
      DO K1=1,999999
       CALL DBFILE(0,ARRAY,JRCD)
       IF (JRCD.NE.0) GO TO 110
       KEY = JRRAY(1,2)
C
C RECORD 117 CONTAINS INFORMATION ABOUT THE ELECTRIC POTENTIAL
C THE NODES OF INTERESTS ARE 224 (ACTUATOR) AND 3757 (SENSOR)
        F_NODE = JRRAY(1,3)
        IF (KEY.EQ.65) THEN
          IF (KI.EQ.4703) THEN
10          FORMAT(F20.15,1X,F20.15)
            OPEN(UNIT=101, FILE='/usr1/people/brian/abaqus/
     +Chapter_4/SENSOR_OUTPUT.txt', STATUS='NEW')
            WRITE(101,10)ARRAY(3),ARRAY(6)
            CLOSE(UNIT=101)
            OPEN(UNIT=113, FILE='/usr1/people/brian/abaqus/
     +Chapter_4/Strain_Scratch.txt', STATUS='NEW')
            WRITE(113,10)ARRAY(3),ARRAY(6)
            CLOSE(UNIT=113)
          ENDIF
          KI = KI + 1
        ENDIF
            IF (KEY.EQ.117) THEN
          IF (F_NODE.EQ.4252) THEN
```

```
          OPEN(UNIT=108, FILE='/usr1/people/brian/abaqus/
     +Chapter_4/Act_Scratch.txt', STATUS='NEW')
          WRITE(108,10)ARRAY(4),ARRAY(5)
          CLOSE(UNIT=108)
        ENDIF
          ENDIF
C
C RECORD 103 CONTAINS INFORMATION ABOUT THE TOTAL ACCELERATION
C THE NODE OF INTEREST IS 12 (BEAM TIP)
      IF (KEY.EQ.103) THEN
        IF (F_NODE.EQ.12) THEN
          OPEN(UNIT=114, FILE='/usr1/people/brian/abaqus/
     +Chapter_4/Accel_Scratch.txt', STATUS='NEW')
          F_ACCEL = ((ARRAY(4)**2)+(ARRAY(5)**2))**(0.5)
20          FORMAT(F20.15)
          WRITE(114,20)F_ACCEL
          CLOSE(UNIT=114)
       ENDIF
      ENDIF
C
    END DO
 110  CONTINUE
C
    RETURN
    END
```

Appendix E

ABAQUS FORTRAN Subroutines for Implementation of PPF Control

```
*SUBROUTINE URDFIL
*WRITTEN BY BRIAN P. BAILLARGEON 01/08/2003
*THIS SUBROUTINE READS THE RESTULTS FILE OF AN ABAQUS ANALYSIS
**************************************************************
* LSTOP - FLAG TO INDICATE WHETHER THE ANALYSIS SHOULD CONTINUE (NOT USED)
* LOVRWRT - INDICATES WHETHER OR NOT THE RESULT FILE CAN BE OVERWRITTEN
* KSTEP - INDICATES THE CURRENT STEP
* KINC - INDICATES THE CURRENT INCREMENT
* DTIME - THE TIME INCREMENT
* TIME(1) - INDICATES THE STEP TIME AT THE END OF THE INCREMENT
* TIME(2) - INDICATES THE TOTAL TIME AT THE END OF THE INCREMENT
**************************************************************
      SUBROUTINE URDFIL(LSTOP,LOVRWRT,KSTEP,KINC,DTIME,TIME)
C
      INCLUDE 'ABA_PARAM.INC'
C
      DIMENSION ARRAY(513),JRRAY(NPRECD,513),TIME(2)
      EQUIVALENCE (ARRAY(1),JRRAY(1,1))
      REAL F_STRAIN,F_STRAIN_NEW,F_STRAIN_OLD,F_DISP,F_DISP_NEW,
     +F_DISP_OLD
      COMMON F_STRAIN_NEW,F_DISP_NEW
      INTEGER F_NODE, KI
C
C FIND THE CURRENT INCREMENT
C
      CALL POSFIL(KSTEP,KINC,ARRAY,JRCD)
      KI = 0
      DO K1=1,999999
       CALL DBFILE(0,ARRAY,JRCD)
       IF (JRCD.NE.0) GO TO 110
       KEY = JRRAY(1,2)
C
C RECORD 21 CONTAINS INFORMATION ABOUT THE STRAIN
        F_NODE = JRRAY(1,3)
        IF (KEY.EQ.21) THEN
          IF (KI.EQ.4695) THEN
            F_STRAIN = ARRAY(3)
            OPEN(UNIT=200, FILE='/usr1/people/brian/abaqus/
     +Chapter_4/F_STRAIN_OLD.txt', STATUS='OLD')
            READ(200,*)F_STRAIN_OLD
            CLOSE(UNIT=200)
            F_STRAIN_NEW = 2*F_STRAIN-F_STRAIN_OLD
            WRITE(7,*) 'Strain URDFIL'
            WRITE(7,*) F_STRAIN_NEW
            F_STRAIN_OLD = F_STRAIN
```

```
          OPEN(UNIT=201, FILE='/usr1/people/brian/abaqus/
     +Chapter_4/F_STRAIN_OLD.txt', STATUS='OLD')
          WRITE(201,*)F_STRAIN_OLD
          CLOSE(UNIT=201)
        ENDIF
        KI = KI + 1
      ENDIF
C RECORD 101 CONTAINS INFORMATION ABOUT THE NODAL DISPLACEMENTS
      IF (KEY.EQ.101) THEN
        IF (F_NODE.EQ.8902) THEN
          F_DISP = ARRAY(4)
          OPEN(UNIT=202, FILE='/usr1/people/brian/abaqus/
     +Chapter_4/F_DISP_OLD.txt', STATUS='OLD')
          READ(202,*)F_DISP_OLD
          CLOSE(UNIT=202)
          F_DISP_NEW = 2*F_DISP-F_DISP_OLD
              WRITE(7,*) 'Displacement URDFIL'
          WRITE(7,*) F_DISP
          F_DISP_OLD = F_DISP
          OPEN(UNIT=203, FILE='/usr1/people/brian/abaqus/
     +Chapter_4/F_DISP_OLD.txt', STATUS='OLD')
          WRITE(203,*)F_DISP_OLD
          CLOSE(UNIT=203)
        ENDIF
      ENDIF
C
    END DO
 110  CONTINUE
C
    RETURN
    END
*SUBROUTINE DISP
*WRITTEN BY BRIAN P. BAILLARGEON 01/08/2003
*THIS SUBROUTINE IS USED TO ALTER THE POTENTIAL ACROSS THE PZT
*****************************************************************
* U - IS THE TOTAL VALUE OF THE PRESCRIBED VARIABLE AT THIS POINT
* KSTEP - IS THE STEP NUMBER
* KINC - IS THE INCREMENT NUMBER
* TIME(1) - IS THE CURRENT VALUE OF THE TIME STEP
* TIME(2) - IS THE CURRENT VALUE OF THE TOTAL TIME
* NODE - IS THE NODE NUMBER
* NOEL - IS THE ELEMENT NUMBER (NOT USED IN THIS ANALYSIS
* JDOF - IS THE DEGREE-OF-FREEDOM
* COORDS - AN ARRAY CONTAINING THE CURRENT COORDINATES OF THIS POINT
*****************************************************************
    SUBROUTINE DISP(U,KSTEP,KINC,TIME,NODE,NOEL,JDOF,COORDS)
C
    INCLUDE 'ABA_PARAM.INC'
C
    DIMENSION U(3),TIME(2),COORDS(3)
    REAL F_STRAIN_NEW,F_DISP_NEW,N_FREQ,C_FREQ,C_G
    COMMON F_STRAIN_NEW,F_DISP_NEW
    DATA F_PI,ACT_GAIN /3.141592653589793,68.0/
C
* THE COMPENSATOR PARAMETERS
    N_FREQ = 2*F_PI*74.443
```

```
      C_FREQ = 1.3*N_FREQ
      C_G = 0.0000025
C
* APPLY THE VOLTAGE TO THE ACTUATORS BASED ON THE COMPENSATOR
* DISPLACEMENT
      U(1)=C_G*(C_FREQ**2)*ACT_GAIN*F_DISP_NEW
      U(2)=0
      U(3)=0
      WRITE(7,*)'ACTUATOR'
      WRITE(7,*)U(1), F_DISP_NEW
C
      RETURN
      END
C
C
*SUBROUTINE DLOAD
*WRITTEN BY BRIAN P. BAILLARGEON 01/09/2003
*THIS SUBROUTINE IS USED TO APPLY A LOAD TO THE COMPENSATOR
*****************************************************************
* F - MAGNITUDE OF THE DISTRIBUTED LOAD
* KSTEP - THE CURRENT STEP
* KINC - THE CURRENT INCREMENT
* TIME(1) - CURRENT VALUE OF THE STEP TIME
* TIME(2) - CURRENT VALUE OF THE TOTAL TIME
* NOEL - THE ELEMENT NUMBER
* NPT - THE LOAD INTEGRATION POINT WITHIN THE ELEMENT OR ON THE
* ELEMENTS SURFACE
* LAYER - THE LAYER NUMBER
* KSPT - THE SECTION POINT NUMBER IN THE CURRENT LAYER
* COORDS - AN ARRAY CONTAINING THE COORDINATES OF THE LOAD INTEGRATION
* POINTS
* JLTYP - IDENTIFIES THE LOAD TYPE FOR WHICH THIS CALL TO DLOAD IS MADE
*****************************************************************
      SUBROUTINE DLOAD(F,KSTEP,KINC,TIME,NOEL,NPT,LAYER,KSPT
     1 COORDS,JLTYP,SNAME)
C
      INCLUDE 'ABA_PARAM.INC'
      DIMENSION TIME(2),COORDS(3)
      CHARACTER*80 SNAME
      REAL F_STRAIN_NEW,F_DISP_NEW,N_FREQ,C_FREQ
      COMMON F_STRAIN_NEW,F_DISP_NEW
      DATA F_PI /3.141592653589793/
C
* THE COMPENSATOR PARAMETERS
      N_FREQ = 2*F_PI*74.443
      C_FREQ = 1.3*N_FREQ
C
C
      F = -(C_FREQ**2)*F_STRAIN_NEW*(1.E6)*100
      WRITE(7,*)'COMPENSATOR'
      WRITE(7,*)F, F_STRAIN_NEW
C
      RETURN
      END
```

BIOGRAPHY OF THE AUTHOR

Brian P. Baillargeon was born in Portland, Maine on November 8, 1979. He was raised in Westbrook, Maine and graduated from Westbrook High School in June of 1998. He then attended the University of Maine and married his wife Stephanie in the fall of 2000. He graduated in 2002 with a Bachelor of Science degree in Mechanical Engineering. He entered the Mechanical Engineering graduate program at the University of Maine in the summer of 2002. Brian is a candidate for the Master of Science degree in Mechanical Engineering from The University of Maine in December, 2003.